Enabling Precise Spatial and Temporal Control of Human

Tissue Morphology and Microenvironments within

Engineered Cell Culture Systems

by

Jason David McNulty

A dissertation in partial fulfillment of the requirement for the degree of

Doctor of Philosophy

(Mechanical Engineering)

at the

UNIVERSITY OF WISCONSIN-MADISON

2015

Date of final oral examination: 12/10/2015

The dissertation is approved by the following members of the Final Oral Committee:

Lih-Sheng Tom Turng, Professor, Mechanical Engineering

Randolph Ashton, Assistant Professor, Biomedical Engineering

Thomas Mackie, Emeritus Professor, Medical Physics

Timothy Osswald, Professor, Mechanical Engineering

Krishanu Saha, Assistant Professor, Biomedical Engineering

Natalie Rudolph, Assistant Professor, Mechanical Engineering

Acknowledgements

Firstly, I want to extend my gratitude towards my co-advisors Prof. Turng and Prof. Ashton. They have been instrumental in my professional development and improvement as a scientist. Without them, I would not have had the opportunity to attend UW to pursue an advanced education and I am forever indebted. Further, my preliminary examination committee (Professors Osswald, Saha and Mackie) has my deepest appreciation for lending support and valuable advice throughout my tenure at UW-Madison.

Next, I'd like to thank my co-workers in the Polymer Engineering Center and the WIDMIR building. Having supportive and innovative colleagues made the past few years exceptional. While it would be very difficult to list all of the folks who made my research successful, the following group of associates have my deepest appreciation for their assistance, guidance and friendship; Thomas Ellingham, Hrishikesh Kharbas, Lukas Duddleston, Sebastian Goris, Ben Cox, George Petry, Robert Swader, Max Salick, Carlos Figueroa, Gavin Knight, and Ethan Lippmann. Each co-worker, co-author and collaborator brought a unique personality, background and expertise that facilitated the advancement of my research for which I am deeply grateful.

Of course, not everyone who deserves my appreciation was directly related to UW-Madison. Here, I'd also like to thank those who made my life more than a series of experiments. Jack Statz, Shawn Wallander, Alicia Geist, Dustin Wagner, Kyle Mayne, Kat Hutchenson, Alison and Kent Peña, Bob and Dorothy Vogelzang and all of those made Madison, WI a very enjoyable place to live for the past 5 years.

Next, I want to recognize that if it weren't for Dr. Adam Kramschuster, I never would have even considered graduate school. With his encouragement, recommendation and support, I was able to muster the courage to apply for the unknown and forever alter my life path. Jesse Pischär and Aaron Pabst are also influential people in my life who inspired my work ethic and were extraordinary role models.

Last but certainly not least, I want to distinguish that my family has played an incredible role in my academic career. Carissa McNulty has been my rock throughout the entire process, encouraging me when I was overwhelmed, reassuring me when I was hesitant and simply being an amazingly patient person. My parents, Tim and Shelly, have been exceptionally helpful. They never complained when I requested help, and were always there whenever needed.

ON WISCONSIN!

Table of Contents

1	Intr	oduc	ction	1
	1.1	Bac	ekground and Significance	1
2	Lite	eratu	re Review	4
	2.1	Ma	terials & Reagents	4
	2.1.	.1	Alginate	4
	2.1.	.2	Polyvinyl Alcohol	5
	2.1.	.3	Ionic Compounds	7
	2.1.	.4	Polyethylene Oxide/Glycol	8
	2.1.	.5	Stainless Steel	9
	2.2	Fab	prication Methods	10
	2.2.	.1	Micro-Injection Molding	10
	2.2.	.2	Rapid Prototyping	12
	2.2.	.3	Robotic Microcontact Printing (R-µCP)	14
3 Se			ecision Robotic Microcontact Printing (R-µcp) Utilizing A Vision Guided Compliant Articulated Robotic Arm	16
	3.1	Intr	oduction	17
	3.2	Sys	tem Design	19
	3.3	Exp	perimental Methods and Materials	21
	3.3.	.1	Rapid Prototyped and Auxiliary Components	21
	3.3.	.2	PDMS Stamp Fabrication and µCP	22
	3.3.	.3	R-µCP Process	23

	Surface-Initiated Activator Generated by Electron Transfer Atom Transfer dical Polymerization (SI-AGET ATRP) of Oligo(ethylene glycol) methyl ether thacrylate (OEGMEMA)	24
3.3.	5 Fluorescent Modification of Grafted PEGMEMA Brushes	. 25
3.3.	al Polymerization (SI-AGET ATRP) of Oligo(ethylene glycol) methyl ether crylate (OEGMEMA)	. 26
3.3.	7 Cell Culture and Staining Procedure	. 26
3.4	Results and Discussion	. 27
3.5	Conclusions	. 33
4 Inc	reasing Uniformity of Substrates Produced Via R-μCP	. 35
4.1	Conclusion	. 40
	prication of Microchannel Networks within Alginate Hydrogels Using Sacrificial Molding Techniques	. 41
6 Sac 64	rificial PVOH Cytocompatibility and Testing of Perfusion Bioreactor Culture Sys	tem
6.1.	1 Bioreactor Design for Neural and Vascular Tissue Culture	. 64
6.1.	2 Biocompatibility Testing	. 66
6.1.	3 Alginate Functionalization	. 72
6.2	Conclusions	. 76
6.3	Future Work	. 76
	Method for Creating Internal Geometries in Injection Molded Parts Using Water- Polyvinyl Alcohol (PVOH) Inserts	78
7.1	Introduction	. 78
7.2	Experimental Methods and Materials	. 82
7.2.	1 Injection Mold Design	. 83
7.3	Results and Analysis	. 85

	7.3.1	Metrology and Dimensional Analysis	. 85
	7.3.2	Surface Morphology Analysis	. 87
	7.4 Cor	nclusion	. 89
8	Conclus	ions and Future Work	. 91

Nomenclature

μCP: Microcontact Printing	14
ABS: Acrylonitrile Butadiene Styrene	13
Ca: calcium	4
CAD/CAM: Computer Aided Design/Manufacturing	82
CBA: Chemical Blowing Agents	11
CNC: Computer Numerical Control	82
DSC: Differential Scanning Calorimetry	92
Dulbecco's modified eagle medium nutrient mixture F-12	67
FDA: Food and Drug Administration	5
G: α-L-guluronic acid	4
human embryonic stem cells	3
M: (1,4)-linked β-D-mannuronic acid	4
Mw: Molecular Weight	8
NECs: Neural Epithelial Cells	67
PBA: Physical Blowing Agents	11
PCL: Polycaprolactone	2
PEG: Polyethylene Glycol	8
PEO: Polyethylene Oxide	8

	vii	
PGA: Polyglycolide	2	
phosphate-buffered saline	67	
PLA: Polylactide	2	
PVOH: Polyvinyl alcohol	2	
rapid mold heating and cooling	91	
SS: Stainless Steel	9	
Tm: Melting Temperature	8	
UV: Ultraviolet	13	

List of Tables

NIST Solubility Database [82]	7
Table 2-2 Composition of various stainless steels adapted from [93].	9
Table 5-1 Twin screw extrusion and microinjection molding processing parameters	.46
Table 5-2 Quantification of water solubility of various calcium compounds adapted from IUPAC-NIST solubility database [82]	. 62
Table 7-1 Injection molding process parameters	.83

List of Figures

Figure 2.1 Chemical structure of Alginate's M and G segments, adapted from KIMICA Corporation [49]
Figure 2.2 Chemical structure of PVOH
Figure 2.3 Examples of PVOH which undergo (A) bulk erosion (Monopol C250, Monosol) and (B) surface erosion (Monopol C100, Monosol) in room temperature water. Time denoted in hours
Figure 2.4 Chemical structure of PEO [85].
Figure 3.1 Diagram of R-µCP system and stamp fabrication. (i, a) Epson LS3 SCARA robot. (b) Custom end effector. (c) Downward facing mobile camera. (d) LED diffuse dome light. (e) Custom stamp nesting fixture with LED dark field ring light. (f) Nitrogen drying station. (g) Deposition material nesting fixture. (h) Substrate nesting fixture. (ii, i) Z-axis effector adapter. (j) Vacuum line. (k) Custom spring-loaded diamond tip etching tool. (l) Vacuum cups. (iii) Schematic of PDMS stamp fabrication process proceeding from top to bottom. (iv) Photo of a mounted PDMS stamp
Figure 3.2 Schematic of stamp features and relative offset positioning. (i) Array 1 (a) and 2 (b) annular post with 600/900 and 300/600 μ m interior/exterior diameters. (c) Array 3 circular posts with 300 μ m diameters. All arrays contained 1200 μ m inter-feature spacing. (ii) Diagram of offset printing arrangement; arrays 1 and 3 are concentric, and array 2 is printed with a relative 600 μ m X and Y offset
Figure 3.3 Micropatterned coverslip images and estimated R- μ CP accuracies. (i) Image of Trial 1, pre-compensation and (ii) Trial 2, post-compensation R- μ CP results. Scale bars are 500 μ m. Non-biased estimates of (iii) translational and (iv) rotational accuracies for each stamped feature array relative to Array 1. * indicates p < 0.05, Student's T-test, n = 3
Figure 3.4 Evaluating R- μ CP's need for constant substrate fixation. Procedural illustrations and representative images of coverslips patterned (i) without and (ii) with substrate removal between each μ CP step. Scale bars are 500 μ m. (iii) Intensity profile of line scan (red) across a single concentric pattern in (ii), which indicates 3 distinct intensities corresponding to each stamped feature array. Non-biased estimates of (iv) translational and (v) rotational accuracies for each stamped feature array relative to Array 1, n = 3.
Figure 3.5 Engineering complex cell culture environments. (i) Schematic of experimental process to graft PEGMEMA brushes with heterogeneous functionalities, i.e. a terminal bromine group vs. a terminal azide group, seed GFP+ NSCs, and then modify PEGMEMA brush array 1 in situ with a clickable biotin ligand. Post-fixation, the presence of biotin was detected using streptavidin-546

culture environment post streptavidin-546 staining. Scale bars are 500 µm33
Figure 4.1 Example image of concentrically patterned features on a microscope coverslip produced with R-μCP
Figure 4.2 Illustration of (A) non-flat/parallel stamp and (B) parallel stamp cross sections
Figure 4.3 Modified stamp holder with 4× micro-adjusters and center screws
Figure 4.4 Image of (A) original rigid tooling and (B) spring assisted conformal tooling
Figure 4.5 MATLAB graphical images of the experiment between patterning techniques/tools 39
Figure 4.6 Quantitative data of the fluorescent intensity vs. sample production technique (n=3 printed samples per method)
Figure 5.1 Illustration of PVOH and calcium salt compounding followed by injection molding of a sacrificial PVOH-Ca template, which is subsequently encapsulated and dissolved within a hydrogel matrix
Figure 5.2 Representative images of channel-laden hydrogels casted using sacrificial PVOH and PVOH-CaCl2 templates. (A) PEG, (B) polyacrylamide, and (C) alginate hydrogels cast using PVOH templates. (D) Alginate hydrogel cast using a 10% (w/w) loaded PVOH-CaCl2 template. (E) Schematic of cross-sectional hydrogel slices made to measure outer, middle, and interior channel diameters. Representative images of cross-sectioned alginate hydrogels cast using (F) PVOH and (G) 10% loaded PVOH-CaCl2 templates. (H) Metrological analysis of the hydrogel channel diameter's deviation (%) from the sacrificial template's geometry. Data combined from duplicate experiments to yield n=8, 16 and 24 for outer, middle and inner channels, respectively. Error bars represent standard deviation; *P<0.05, Student's unpaired t-test; scale bar is 3 mm
Figure 5.3 Mechanical property analysis at 25 °C. Tensile test of injection molded PVOH and PVOH-Ca specimens' (A) ductility, (B) Young's modulus and ultimate tensile strength (UTS) results, n=10 experimental replicates and error bars represent standard deviation. (C) Rheological analysis of each specimens' viscosity over a range of shear rates.
Figure 5.4 Material properties and calcium release analysis. (A) Representative thermogravimetric scans, n=3 experimental replicates. (B) Complexometric calcium titration, n=5 experimental replicates, *P<0.05, Student's unpaired t-test. Differential scanning calorimeter's (C) second heating and (D) first cooling curve traces of neat and extruded (Ext) PVOH and PVOH-Ca composites 57
Figure 5.5 Representative images of (A) 10% Ca(C ₂ H ₃ O ₂) ₂ loaded PVOH sacrificial fiber templates as micro-injection molded (top) and dissolved within alginate hydrogels (middle). (B) Dimensional analysis was performed on CT scan reconstructions (A, bottom) of three separately cast alginate

3 mm
Figure 5.6 Modular 3D sacrificial molding using PVOH- $Ca(C_2H_3O_2)_2$ templates. (A) Exploded CAD model of modular, 3-D template design. (B) As molded and assembled 3-D template, and (C) sacrificially molded channel network within an alginate hydrogel. (D) CT scanned reconstruction of the channel network within an alginate monolith. Scale bar is 3 mm.
Figure 5.7 CAD drawing of the 2D, sacrificial PVOH lattice templates with associated CNC-milled aluminum mold. All dimensions in mm
Figure 5.8 CAD drawing of the 2D, sacrificial filament templates with associated CNC-milled aluminum mold. All dimensions in mm. 63
Figure 5.9 CT scanned reconstruction of a 3D channel network within a polyacrylamide monolith63
Figure 6.1 Schematic of custom bioreactor system, identifying flow directions and equipment configurations.
Figure 6.2 Bioreactor temperature control profile with proportional control (P=4.5) and media flow at 0.3 mL/min.
Figure 6.3 NECs seeded within a Matrigel coated, standard TCPS 6 well culture plate
Figure 6.4 NECs seeded within a 303SS bioreactor on a Matrigel coated acrylic base
Figure 6.5 NECs seeded within a 316SS bioreactor on a Matrigel coated acrylic base
Figure 6.6 H9s seeded within a Matrigel coated standard TCPS culture plate subjected to a neural differentiation protocol. Rosette formation begins in day 1 and can be seen significantly in day 369
Figure 6.7 H9s seeded within a 316SS bioreactor on a Matrigel coated TCPS base subjected to a differentiation protocol while temperature and PH were controlled inside a standard cell culture incubator. Rosette formation begins in day 1 and can be seen significantly in day 2
Figure 6.8 H9s seeded within a 316SS bioreactor on a Matrigel coated TCPS base subjected to a differentiation protocol while temperature and PH was externally controlled. Rosette formation begins in day 1 and can be seen significantly in day 2
Figure 6.9 Representative images of the HUVECs cultured with varying amounts of PVOH within the cell culture media. 0.001 and 0.1 mg/mL concentrations not shown
Figure 6.10 Results at day 6 from the Cyquant assay performed on the HUVECs exposed to varying concentrations of dissolved PVOH.
Figure 6.11 Standard curve of RGD mixed with alginate at various concentrations

Figure 6.12 Representative images of HUVECs seeded onto standard TCPS well plates74
Figure 6.13 Representative images of HUVECs seeded onto RGD conjugated alginate within a 316SS externally controlled bioreactor prior to perfusion
Figure 6.14 Representative images of HUVECs seeded onto RGD conjugated alginate within a 316SS externally controlled bioreactor during perfusion
Figure 7.1 Custom designed components for injection mold tooling. Sacrificial PVOH components for assessing (A) geometric dimensional stability and (B) surface roughness
Figure 7.2 (A) Image of PVOH molded patterns in blue pigment and (B) image of PVOH molded patterns overmolded with LDPE.
Figure 7.3 (A) Average measurement of all critical dimensions for all each material. (B) Average percent deviation of critical dimensions as compared to the initial PVOH pattern dimensions. The sample size was 10.
Figure 7.4 Surface morphology of (A) milled PVOH pattern, (B) surface ground PVOH pattern, (C) milled LDPE relief, (D) surface ground LDPE relief, (E) milled PP relief, (F) surface ground PP relief, (G) milled PC relief, and (H) surface ground PC relief. All units in µm
Figure 7.5 Optical microscope images displaying surface morphology of (A) PVOH patterns and the relief surfaces on (B) LDPE (C) PP and (D) PC substrates

Abstract

Increased understanding of human developmental biology gives researchers more opportunities for experimentally modeling diseases and testing new regenerative therapies. Due to the expensive and typically inefficient nature of experimental research, scientists prefer to perform high-throughput analysis on microscale samples which allows for more rapid screening of important factors. Ideally, researchers would have off-the-shelf disease templates that could be quickly and accurately sampled, but only few, simple disease kits are commercially available.

Depending on the application, disease models can often be simplified into two dimensional arrays using processes such as microcontact printing (μ CP). While a promising technique for producing spatially organized microenvironments, the lack of standardized, precision equipment for performing the deposition results in frequently oversimplified substrates with limited complexity or biological relevance. The first aim of the research presented in this thesis is to develop an automated system which allows for free-form, high-precision, and uniform μ CP onto a variety of substrates with sequential deposition capabilities. This robotic microcontact printing (R- μ CP) technology will enable researchers to overcome major challenges with tissue engineering by providing chemically defined and scalable means to precisely engineer tissue morphology and microenvironments over multiple length scales in a spatial and temporal manner. As the results show, the prototype system not only possesses the ability to align multiple polydimethylsiloxane (PDMS) stampings, but it has the capability to do so even after the substrates have been removed, and replaced back onto the system with <10 μ m precision and accuracy. Moving forward, the R-

μCP technology will facilitate the unprecedented engineering of highly-complex culture substrates.

In many cases, two dimensional disease models are not sufficient for gaining complete understanding of microscale biological interactions. Therefore, researchers have attempted to produce three dimensional tissue scaffolds for addressing these limitations. Rapid prototyping has become a preferred technology for producing the scaffolds despite poor geometrical control, extensive manufacturing cycle times and distinct material selection restrictions. The second aim of this research is to develop processes for the fabrication of highly-complex engineered hydrogel scaffolds with internal and external microscale architecture using sacrificial synthetic thermoplastic polymers, with high-throughput and scalable manufacturing techniques such as micro-injection molding. With this technique, exemplary biocompatible scaffolds were produced with poly(vinyl alcohol)-calcium salt templates (PVOH-Ca) and fabricated by micro-injection molding, to cast internal geometries within both bulk and ionically curing hydrogels. Computed tomography (CT) analysis demonstrated that this process enabled casting of microscale features with $6.4 \pm 7.2\%$ average error. Additionally, by assembling multiple modular PVOH-Ca templates, full 3D channel networks with multiple length scales were produced within alginate hydrogels to demonstrate the flexibility of the technology. Thus, micro-injection molding of sacrificial PVOH-Ca templates should be capable of implementation in diverse tissue engineering applications.

Due to the sacrificial molding innovation it was hypothesized that a similar process could be used to produce other thermoplastic polymer components with internal complexities. Therefore, the sacrificial PVOH patterns were also overmolded with a non-

water-soluble polymer shell via injection molding and subsequently submerged in water to dissolve the initial template. Post dissolution, it was observed that intricate and diverse internal features were mass-producible in this manner. Metrological analysis performed on the components has shown precise control of the internal dimensions is possible over a wide range of processing temperatures and conditions with micro-feature replication. Due to the highly-competitive nature of the manufacturing industry, and the potential cost-savings of this innovation, it is expected that this research could significantly impact traditional manufacturing design considerations and time-to-market.

1 Introduction

1.1 Background and Significance

Throughout the past few decades, there has been much interest in trying to create new therapies for biological disorders such as neurodegenerative and cardiovascular diseases. In the ever-changing interdisciplinary field of tissue engineering, researchers in the biomedical, chemical and mechanical engineering fields work closely with biologists and medical professionals to fabricate biological substitutes aiming to restore, maintain, improve or replace native organ functions [1]. Prior to the advent of modern tissue engineering, researchers were limited to treating defective native organs with either bolus injections of autologous cell suspensions or replacing lost or malfunctioning organs by transplantation of autograft, allograft or xenograft. Unfortunately, injections and transplantations both maintain significant drawbacks to their clinical use for the mass public including their limited availability, donor site morbidity, ethical concerns and potential immune system rejection leaving a gaping void for alternative therapies [2-6].

The tissue engineering field has made vast strides in the past 30 years and the pace has increased even more so in the last decade with more research groups forming and technologies being introduced every year. Researchers have moved to using a wide variety of natural and synthetic biomaterials as scaffolding for cells to infiltrate, remodel and thrive [7, 8]. It has been shown that a suitable biomaterial will maintain a minimum of three properties: 1) biocompatibility or bioresorbability, 2) adequate mechanical properties that match the host site [9], and 3) protein adsorbable surface chemistry [10]. It is also desirable that the scaffolding biomaterial is highly porous with moderate interconnectivity to ensure efficient

mass transport of nutrients such as oxygen and growth factors, and enable waste removal and sufficient cell-cell signaling [11-13].

To date, researchers struggle with producing engineered scaffolds that fill these requirements in a scalable, repeatable and high throughput manner while maintaining desired control of the microscale architecture. Without achieving both topographical quality and production efficiency, it is difficult to realize the potential of high throughput analysis methods. The research presented in this thesis aims to describe novel methodology for utilizing standardized mass production techniques to produce 2D and 3D engineered scaffolds which will utilize customized materials to control cellular microenvironments. Synthetic biomaterials such as polylactide (PLA), polyglycolide (PGA), polyvinyl alcohol (PVOH) and polycaprolactone (PCL) offer numerous advantages when compared to their natural counterparts such as gelatin, fibrin and collagen. Firstly, they are chemically defined ensuring all experimental findings are not an artifact of unknown ingredients [14]. Secondly, they can be synthesized in nearly infinite quantities with little to no batch variation [15, 16]. Thirdly, synthetic materials may be processed with a variety of conventional processing equipment such as injection molding machines, thermoformers and extruders [17, 18]. Lastly, their mechanical, chemical and bio-related properties can be altered quickly and efficiently with simple chemical modifications making them suitable for a variety of applications [19-21]. For example, with little modification, PVOH can be manufactured to be either a rigid or ductile material or be synthesized with a high water content as a hydrogel [22].

Once the scaffolding has been manufactured, specific cell lines are seeded onto the structures in hopes that they begin to attach and proliferate. Until now, tissue engineers have

relied heavily on the self-assembly capabilities of human embryonic stem cells (HESCs) to spontaneously organize into biomimetic tissues which may be useful for regenerative therapies. Unfortunately, this approach rarely results in functional and morphologically correct tissues, largely because cellular organization and functionality depends on feedback from the HESCs surroundings. The engineered scaffold's shape, topography, mechanical properties and chemical composition can all affect the performance of the HESCs population. Environmental properties such as cell culture media temperature, PH and flowrate are also critical factors whose optimal values vary depending on cell type. Additionally, without understanding developmental biology, physiologically relevant and functional tissues may be impossible to produce without co-cultures of multiple cell lines to provide proper cell-to-cell interactions and crosstalk.

It should now be obvious that there is a dramatic need for tissue engineers to develop culture systems and scaffold fabrication techniques which address all of the aforementioned elements simultaneously. With this in mind, the remainder of this thesis starts with Chapter 2, which provides a literature review on prior work, followed by Chapters 4 and 5 aiming to enable versatile engineering of microscale tissue microenvironments which can be used to control morphogenesis of 2D biomimetic tissue models derived from HESCs. Chapter 6 aims to demonstrate a novel hydrogel based fabrication technique based on sacrificial polyvinyl alcohol (PVOH) patterns allowing for the production of complex 3D scaffolds with defined internal and external architectures to have more control over tissue morphogenesis. Chapter 7 exhibits a series of industrial applications for a similar thermoplastic based process, which has significant implications with respect to polymer part design for manufacturability. Chapter 8 discusses the overall conclusions and proposed future work related to the research.

2 Literature Review

2.1 Materials & Reagents

Presented in this chapter is an overview of the significant and relevant materials and fabrication methods used throughout this research.

2.1.1 Alginate

Alginate is a natural anionic polysaccharide derived from abundantly available brown seaweed or bacteria [8, 26-28]. It contains alternating segments of (1,4)-linked β-D-mannuronic acid (M) and α-L-guluronic acid (G) (**Figure 2.1**) with quantities of each component depending on the natural source of extraction [29]. The G segments of the polymer chain provide intermolecular cross-linking with divalent cations such as calcium (Ca) to form high water content hydrophilic hydrogels. In addition to being ionically cross-linkable [30-35], alginate has been modified to be thermally gelled [36, 37], bound by cell ligands [38, 39], photocrosslinked [26, 40] or covalently cross-linked with poly(ethylene glycol)-diamines [41-46], as further demonstrations of its versatility. Currently, there are over 200 manufacturers of alginate whose product differs in ratio of M and G, molecular weight and composition (block sequence) thereby affecting the hydrogels mechanical properties [47, 48].

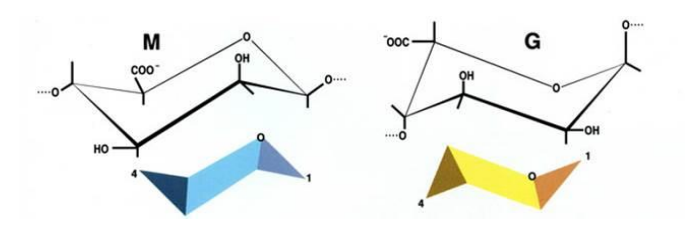


Figure 2.1 Chemical structure of Alginate's M and G segments, adapted from KIMICA Corporation [49].

Being a United States Food and Drug Administration (FDA) approved polymer, alginate hydrogels have been heavily used in minimally invasive procedures including drug and cell delivery [50-53], wound healing dressings [54, 55], cartilage repair [56-60] and bone regeneration [61-68]. Not only has alginate repeatedly proven itself as a biocompatible material, it is inherently inert and non-degradable in humans because we don't produce the chain-cleaving enzyme, alginase [69]. This however can be an advantage of the biomaterial, being that engineers can ensure the cell laden scaffolds are well integrated prior to providing instructive degradation techniques and removing the alien material from the patient. Therefore, it is anticipated that one can use alginate hydrogels to control the morphology of cellular constructs prior to surgical integration with a human host, ensure full assimilation with native tissue and degrade orthogonally. Thus, we have chosen to use alginate as a tissue engineering hydrogel scaffold because it can be tuned to have controllable physical properties and degradation events.

2.1.2 Polyvinyl Alcohol

The water-soluble, synthetic polymer polyvinyl alcohol (PVOH), [CH₂CH(OH)]_n (**Figure 2.2**), has long been used in papermaking, textiles and film coatings. PVOH is manufactured via partial or full hydrolysis of polyvinyl acetate to eliminate the acetate groups from the chains. Based on the degree of hydroxylation, chemists are able to modify the mechanical properties of the polymer, and tune it for a variety of applications [70]. Being that PVOH is a thermoplastic polymer, it has the ability to be processed via traditional polymer processing equipment including injection molding [71, 72], extrusion [73] and thermoforming [74]. Further, PVOH has also been identified as a suitable material for biomedical applications including tissue engineering scaffold fabrication due to its low

protein adsorption characteristics, biocompatibility and high water solubility at low temperatures [75]. In addition to being biodegradable, the dissolution time and methods of PVOH can be modified by altering the molecular weight of the polymer chains [76]. Numerous manufacturers of PVOH have developed formulations which undergo both surface and bulk erosion, allowing for varying decomposition times which correspond to numerous applications in tissue engineering [77-80]. Throughout this research, PVOH has been injection molded into various precision geometries templating physiologically relevant structures which were subsequently dissolved within hydrogels and other thermoplastic shells to produce tissue scaffolds for control of 3D tissue morphogenesis.

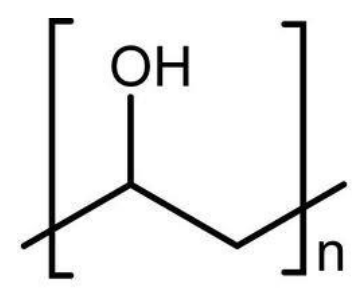


Figure 2.2 Chemical structure of PVOH.

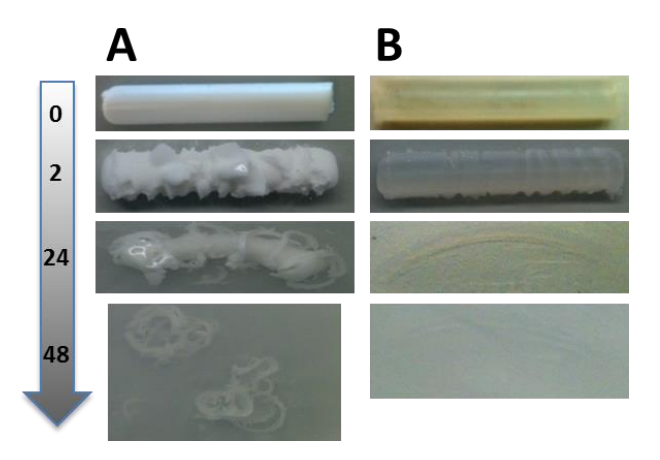


Figure 2.3 Examples of PVOH which undergo (A) bulk erosion (Monopol C250, Monosol) and (B) surface erosion (Monopol C100, Monosol) in room temperature water. Time denoted in hours.

2.1.3 Ionic Compounds

Ionically bound compounds such as sodium chloride (NaCl), calcium chloride (CaCl₂), and calcium sulfate (CaSO₄) are commonly used ingredients to modify synthetic biomaterials for tissue engineering applications. Frequently, they are used as sacrificial fillers to disrupt the continuity of polymer matrices and create pores once dissolved [81]. Additionally, CaCl₂ and CaSO₄, are used as chelating agents for some biomaterials such as alginate [8]. Essentially, when calcium salts are added into the aqueous alginate solution, the compound dissolves and frees the Ca ions to interact with the G segments of the alginate. The rate of the alginate gelation can be modified by increasing or decreasing the quantity of free Ca ions in the solution [33]. This can be done by simply using calcium salts of varying water solubility. **Table 2-1** below identifies a list of Ca compounds which vary in water solubility from 0-128 g/100ml with temperature variation.

Table 2-1 Quantification of water solubility of various calcium compounds adapted from IUPAC-NIST Solubility Database [82].

		Temperature (°C)				
Compound	Formula	0	10	20	30	40
Calcium Carbonate	CaCO ₃	0.0	0.0	0.0	0.0	0.0
Calcium Sulfate	CaSO ₄	0.2	0.2	0.3	0.3	0.3
Calcium Acetate	$Ca(C_2H_3O_2)_2$	37.4	36.0	34.7	33.8	33.2
Calcium Iodide	CaI ₂	64.6	65.3	66.0	67.6	70.8
Calcium Chloride	CaCl ₂	59.5	64.7	74.5	100.0	128.0

Also, it has been discovered that when compounds such as those in **Table 2-1** are combined with certain synthetic biomaterials like PVOH, the Ca ions may act as cross-

linking agents and irreversibly bind adjacent polymer chains [83]. We have observed this phenomenon, and have used the salts solubility as a tuning parameter to facilitate the development of alginate-based scaffolds with an internal vascular network using microinjection molded PVOH/Ca-salt composites as the templates.

2.1.4 Polyethylene Oxide/Glycol

Polyethylene oxide (PEO) or polyethylene glycol (PEG) is a water-soluble polyether compound that can be synthesized in an enormous variety of molecular weights (**Figure 2.4**). Typically, a low molecular weight (M_w <100,000) chain is considered a PEG, while those greater than 100,000 are described as PEO [84]. While PEG polymers usually take the form of transparent to opaque hydrogels, PEGs can be identified by their white color and solid mechanical properties. Additionally, PEOs maintain a melting temperature (T_m) proportional to their M_w with a maximum around 67°C.

$$H^{O}$$

Figure 2.4 Chemical structure of PEO [85].

Due to their inherent biocompatibility and non-fouling characteristics, PEG hydrogels and PEO thermoplastics have been used in biomedical applications for years [86]. Specifically, PEG hydrogels have been in drug delivery [87], wound healing and a variety of other biomedical applications [88-90] while PEO composite scaffolds have been used for

more structural purposes including bone [91] and cartilage [92]. In this research, PEO has been proposed as an alternative water-soluble material to PVOH.

2.1.5 Stainless Steel

To ensure cell survival *ex-vivo*, biomedical scientists are required to engineer bioreactor systems with precise control of numerous factors including temperature, PH and humidity. As it happens, these factors are also directly related to the oxidation rate of traditional fabrication materials. Because cells and culture media are in direct contact with the bioreactor, chemical leeching from the fabrication materials must be minimized. Unlike most ferrous steels, stainless steels (SS) are those with more than 10% chromium, which assists in the prevention of significant amounts of oxidation in the form of corrosion, rust or staining. Additional ingredients in stainless steel alloys can be found in Table 2-2. It can be noted that by changing the composition and structure of the stainless steel, it significantly alters the processability, machinability, mechanical properties and corrosion resistance of the alloy.

Table 2-2 Composition of various stainless steels adapted from [93].

Stainless Steel Composition (%)									
Type	Carbon	Chromium	Nickel	Molybdenum	Manganese	Silicon	Phosphorus	Sulfur	
303	< 0.15	17-19	8-10	0	<2	<1	<0.2	>0.15	
304	< 0.08	17.5-20	8-11	0	<2	<1	< 0.045	< 0.03	
316	< 0.03	16-18.5	10-14	2-3	<2	<1	< 0.045	< 0.03	

2.2 Fabrication Methods

Over the past few decades, many methods for fabricating synthetic scaffolds for tissue engineering have been introduced. Simply due to the lack of space to discuss each, only those in direct competition with this research will be discussed within.

2.2.1 Micro-Injection Molding

Polymer extrusion is a high-volume manufacturing process which can be used to fabricate films, tubes and other components with continuous two-dimensional (2D) profiles [94, 95]. Over the years, industrial vendors have incorporated multiple screws into the extrusion process for enhanced composite mixing capabilities; especially for the compounding of fibers and fillers [96]. Currently, researchers in the polymer processing field are working on additional variations of the extrusion process to reduce polymer densities and viscosities thereby saving money and making subsequent processes such as injection molding easier [97].

The field of tissue engineering has recently adopted polymer extrusion as part of the process for the fabrication of porous scaffolds. Biomaterials like PCL have been compounded with other water-soluble materials such as PEO in order to create co-continuous blends of partially sacrificial polymers [98-100]. After compounding, the extrudate was pelletized and subjected to injection or compression molding procedures to form the final architecture. Once finalized, the composite was placed in a water bath until the entire sacrificial segment of the scaffold was dissolved leaving behind interconnected pores within the matrix material.

Injection molding is a high-volume manufacturing technique which can be used to process thermoplastic and thermoset polymers into complex three-dimensional (3D) shapes repeatedly with little variation [72]. Because many biomaterials display thermoplastic properties, injection molding has been becoming more popular in the tissue engineering circles despite some significant hurdles [101]. Firstly, tissue engineering scaffolds require a highly porous and interconnected architecture in order to permit cellular attachment, migration and permeation. Secondly, injection molding microscale components can be difficult due to the high surface area to volume ratio of the mold to polymer. Additionally, the high aspect ratio in regards to flow length causes significant pressure requirements which may result in parting line flash before fully filling the cavity or short shot.

Injection molders have long been seeking opportunities to reduce material densities without compromising mechanical properties. Many advances have been made by utilizing chemical blowing agents (CBA) or physical blowing agents (PBA) to cause microscale pores throughout the polymer matrix. It was discovered that not only does this save manufacturer's material, but it creates a porous structure which with certain biomaterials could be used for tissue engineering applications. CBAs are chemical compounds that decompose at specific temperatures and release gasses such as CO₂ and N₂; as the gas is released, it stretches the polymer matrix to expand until the pressure can no longer expand the cooling polymer [102]. While PBAs act in the same manner as the CBAs, there is no chemical reaction taking place; supercritical gas is injected into the polymer melt while in the injection unit barrel [103, 104].

While injection molding with CBAs is far more popular for industrial applications, most simply will not work for tissue engineering applications due to potentially cytotoxic chemical residuals left behind after the reaction has taken place. PBAs on the other hand do

not leave behind any foreign material, cause any isolated degradation or provide any endo/exothermic reactions. For this reason, it is preferable for tissue engineers to utilize PBAs when working with biomaterials aimed for biocompatibility. Typically, the resulting foamed components are left with a porous interior with a solid skin layer due to non-uniform cooling temperatures throughout the thickness. Additionally, the majority of the pores are not interconnected even with post processing techniques such as ultrasonic cavitation [105].

2.2.2 Rapid Prototyping

With advances in the capabilities of additive manufacturing, researchers have been able to fabricate microscale components out of a variety of materials. With numerous options and fabrication methods, engineers have the ability to select the technology which best fits a product's needs. Tissue engineers have selectively adopted several techniques in order to manufacture tissue scaffolds with synthetic and natural biomaterials.

Fused deposition modeling (FDM), a form of additive manufacturing was developed by the founders of Stratasys, Ltd in 1989. This process is commonly used for prototyping applications and is now the leading form of rapid prototyping in the open-source consumer market. The process begins with a 3D computer model of the desired component. The model is mathematically sliced into micron thick layers which are then exported as 2D printer rasterization paths. Next, the file is submitted to the FDM hardware for the fabrication process where a polymer filament is extruded through a heated nozzle which moves in the X and Y axis following the toolpaths. After the deposition of each layer is completed, the build platform lowers in the Z axis prior to the deposition of the subsequent layer until all layers are finished [106].

Initially established to deposit materials such as acrylonitrile butadiene styrene (ABS) [107], FDM has been adopted and adapted by tissue engineers worldwide to fabricate all types of organs from myriads of biocompatible materials such as PCL [108, 109] and starch based carbohydrate glass [110]. In addition to rigid thermoplastics though, FDM has been altered to process bio-matter such as cellular organoids and slurries to orchestrate the direct placement of individual cells. The hardware for bioprinting, is nearly identical to that of FDM, but without the need for the extreme temperatures or filaments. Instead, modern bioprinters utilize syringes of varying sizes to control the deposition rates and volumes. In the past few years, bioprinters have become the new standard of cutting edge biomedical engineering equipment and have facilitated the growth of vascular networks [111-116], skin [117] and many other tissues with limited biomimetic structure.

Selective laser sintering (SLS) is another form of rapid prototyping that utilizes a laser power source in order to sinter powdered material (metal or polymer) [118-120]. Developed by Dr. Carl Deckard at the University of Texas at Austin, the process utilizes software to slice micron thick sections of a 3D computer model to develop 2D toolpaths, which are used to control a galvanometer driven laser.

In recent research, numerous groups have utilized SLS methodology to fabricate tissue engineering scaffolds for biological research. Examples include the development of porous PCL scaffolds for bone and cartilage repair [121] and PVOH/hydroxyapatite biocomposite scaffolds for intervention of craniofacial and joint defects [122].

Stereolithography (SLA) is another form of additive manufacturing which utilizes an ultraviolet (UV) laser to cure a liquid photo-reactive resin [123]. Similar to the other forms of rapid prototyping technologies, SLA develops its laser toolpaths from 2D slices of a 3D

computer model. Next, the SLA hardware uses the toolpaths to direct the UV laser in the X and Y axis [124]. As the UV laser is focused on the surface of the resin, the beam cross-links and polymerizes the resin into a solid and joins it to the previously built layers. Once the layer is complete, the build platform sinks deeper into the resin revealing another thin coating of liquid resin to cure.

Since its inception, SLA has been used to fabricate all types of materials, including ceramics [125], polymers [126] and hydrogels [127, 128]. Due to its high resolution capabilities, the dimensional capabilities produced by SLA are nearly unmatched by other prototyping methods. Since many biomaterials can be modified to be photopolymerizable, SLA has become a commonly used technology in the biomedical field for creating scaffolds with complex internal and external architectures. Specifically, researchers have used SLA to fabricate vascular networks [129], bone regeneration scaffolds [130, 131] and molds for various ligaments [132, 133], as examples.

2.2.3 Robotic Microcontact Printing (R-µCP)

Being that not all biological research needs to be performed in three dimensions, many scientific endeavors can be explored on traditional cell culture substrates such as microscope coverslips and polystyrene well plates. Because research of this nature is costly and largely inefficient, it is desirable to perform experiments in a high-throughput manner with minimal cells and culture media. One method, which is frequently used to increase the efficiency of cellular experimentation, is microcontact printing (μ CP), where cytophobic substrates are rendered cell adhesive in spatially controlled regions defined by the micro tooling [134, 135]. This technology when combined with modern robotics enables

unprecedented microscale control of cellular attachment, migration and even cell to cell contact [20].

3 High-Precision Robotic Microcontact Printing (Rµcp) Utilizing A Vision Guided Selectively Compliant Articulated Robotic Arm

Increased realization of the spatial heterogeneity found within in vivo tissue microenvironments has prompted the desire to engineer similar complexities into in vitro culture substrates. Microcontact printing (µCP) is a versatile technique for engineering such complexities onto cell culture substrates because it permits microscale control of the relative positioning of molecules and cells over large surface areas. However, challenges associated with precisely aligning and superimposing multiple µCP steps severely limit the extent of substrate modifications that can be achieved using this method. Thus, we investigated the feasibility of using a vision guided selectively compliant articulated robotic arm (SCARA) for µCP applications. SCARAs are routinely used for high precision, repetitive tasks in manufacturing, and even low-end models are capable achieving of microscale precision. Here, we present customization of a SCARA to execute robotic-µCP (R-µCP) onto goldcoated microscope coverslips. The system not only possesses the ability to align multiple polydimethylsiloxane (PDMS) stampings, but it has the capability to do so even after the substrates have been removed, reacted to graft polymer brushes, and replaced back onto the system. Plus, non-biased computerized analysis shows that the system performs such sequential patterning with <10 µm precision and accuracy, which is equivalent to the repeatability specifications of the employed SCARA model. R-µCP should facilitate the engineering of complex in vivo-like complexities onto culture substrates and their integration with microfluidic devices.

3.1 Introduction

In biological systems, the relative positions of constituent entities play a significant role in determining interactions and resulting behaviors. To properly control and model these interactions, researchers modify the mechanical, electrical, chemical, and biochemical properties of substrates in order to predictably position cells [19, 136-139], extracellular matrix (ECM) proteins [140-144], growth factors, DNA [145, 146], drugs, and other ligands. Further, by integrating these engineered substrates with microfluidic devices, one can also obtain precise control over the soluble as well as immobilized factors within microscale environments [147, 148].

Microcontact printing (μ CP) is a widely used method for spatially patterning surface molecules that can impart the previously mentioned substrate properties. It entails coating an elastomeric stamp of polydimethylsiloxane (PDMS) presenting nano-to-microscale features with a deposition material (e.g. solution of alkanethiols) and then printing a relief pattern of that material onto substrates (e.g. gold films) by making conformal contact [135]. The specifics of microcontact printing (μ CP) have been reviewed in great detail elsewhere [134], particularly in regards to printing patterns of alkanethiols onto gold-coated substrates [149, 150].

While μ CP is a versatile technique for patterning large surface areas with features as small as 50 nm [151, 152], it remains a challenge to efficiently align and superimpose multiple μ CP steps in an automated fashion onto a single substrate with high accuracy and precision while simultaneously permitting maximal flexibility in substrate modification chemistry. While others have developed devices to execute sequential μ CP, their methods

contain significant limitations or drawbacks. For example, Ng et al. used a manual alignment μCP system to position and apply sequential patterns on glass substrates, however the precision of the system was limited to ~30 µm in the X and Y directions [153]. Chakra et al. developed a semi-automated instrument capable of sequentially patterning a single substrate with 1 µm precision when using a single stamp, but a 10-fold decrease in precision was observed when using two different stamps. Further, no measurement of stamping accuracy was provided, and use of this device requires each PDMS stamp to be fabricated using a precisely machined, custom apparatus [154]. Similarly, Tien et al. developed elegant multileveled stamps to sequentially print aligned patterns but this too requires complex silicon wafer/stamp fabrication and inking procedures that potentially limit scalability [155]. Using a manual kinematic coupling system, Trinkle et al. was able to achieve a μ CP precision of < 1 µm even when exchanging stamps [156]. However, the relative location of each stamp cannot be freely adjusted, and the accuracy of their system is dependent on high precision stamp fabrication. Furthermore, it remains a challenge to remove substrates between sequential µCP patterning steps while maintaining microscale alignment, thus severely limiting the diversity of surface modification chemistries that can be utilized. Consequently, there remains a need for developing a µCP system that delivers accurate and precise alignment, flexibility in PDMS stamp and substrate design, and automation for scalable manufacturing.

Here, we have designed a robotic μCP (R- μCP) method using a vision guided, selectively compliant articulated robotic arm (SCARA) that eliminates the previously mentioned limitations. Our R- μCP method allows maximum flexibility in substrate and PDMS stamp design and fabrication, and it permits quick and facile exchange of PDMS

stamps. With our system, μ CP can be performed with high accuracy relative to a predetermined location on the substrate, and the stamping location can be modified in real time. Further, we have demonstrated that R- μ CP can be used to sequentially pattern a single substrate with 3 different stamps while maintaining an accuracy and precision of <10 μ m in the X and Y directions and <0.1° in θ even with periodic removal of the substrate from the system between stampings. Thus, R- μ CP vastly expands the number of sequential stampings and type of modification chemistries that can be used to engineer a single substrate compared to previous methods, and provides the level of automation required for manufacturing.

3.2 System Design

Our R- μ CP system was designed around an Epson LS3-401ST SCARA secured to the top of an aluminum platform (**Figure 3.1i**). The SCARA has a manufacturer listed precision of ± 10 microns [157] in the X and Y directions and $\pm 0.01^{\circ}$ in θ . To provide vision guidance for the SCARA, one 1280 \times 1024 resolution camera was mounted to the robotic arm facing the platform, and a second camera was mounted under the stamp nesting fixture facing upward. Both cameras (New Electric Technology, Mo. NS4133BU) were connected to an Epson RC90 controller through an Epson CV1 vision guidance system to provide photo acquisition for analyzing the SCARA's position. Importantly, an LED diffuse dome light was placed in line with the mobile, downward facing camera to provide consistent substrate imaging conditions. Also, a dual-purpose, custom end effector with vacuum cups for handling PDMS stamps and a diamond tipped etching tool was secured to the SCARA's Z-axis arm (**Figure 3.1ii**). The end effector's vacuum pressure was actuated by an electrically operated solenoid controlled with the R- μ CP program coding.

The SCARA's platform was engineered with custom fixtures to facilitate μ CP. The PDMS stamp nesting fixture was fabricated with a custom LED dark field ring light to enable imaging of the stamp's feature pattern using the upward facing camera. The substrate nesting fixture was engineered as a vacuum chuck with an array of ~1 mm holes through which vacuum was applied to eliminate substrate translation throughout the stamping process. The PDMS drying station consists of a pair of flexible modular hoses with fan nozzles connected to a nitrogen stream actuated using an electric solenoid. Additionally, a nesting fixture for holding deposition materials was added to the SCARA platform.

A significant advantage of R- μ CP is the allowance of freeform substrate and PDMS stamp fabrication. Standard microfabrication techniques can be used to generate substrates and stamps with no required usage of precision machined custom molds or apparatuses [135]. In this study, hand-cut gold-coated microscope coverslips served as the μ CP substrate, and PDMS stamps of uniform thickness were fabricated with the assistance of a plastic ring and weighted curing lid (**Figure 3.1iii**). After curing, the PDMS stamps were bonded to an acrylonitrile butadiene styrene (ABS) backing to ensure even pressure distribution upon μ CP. The ABS backing can be substituted with alternative materials of similar rigidity (**Figure 3.1iv**).

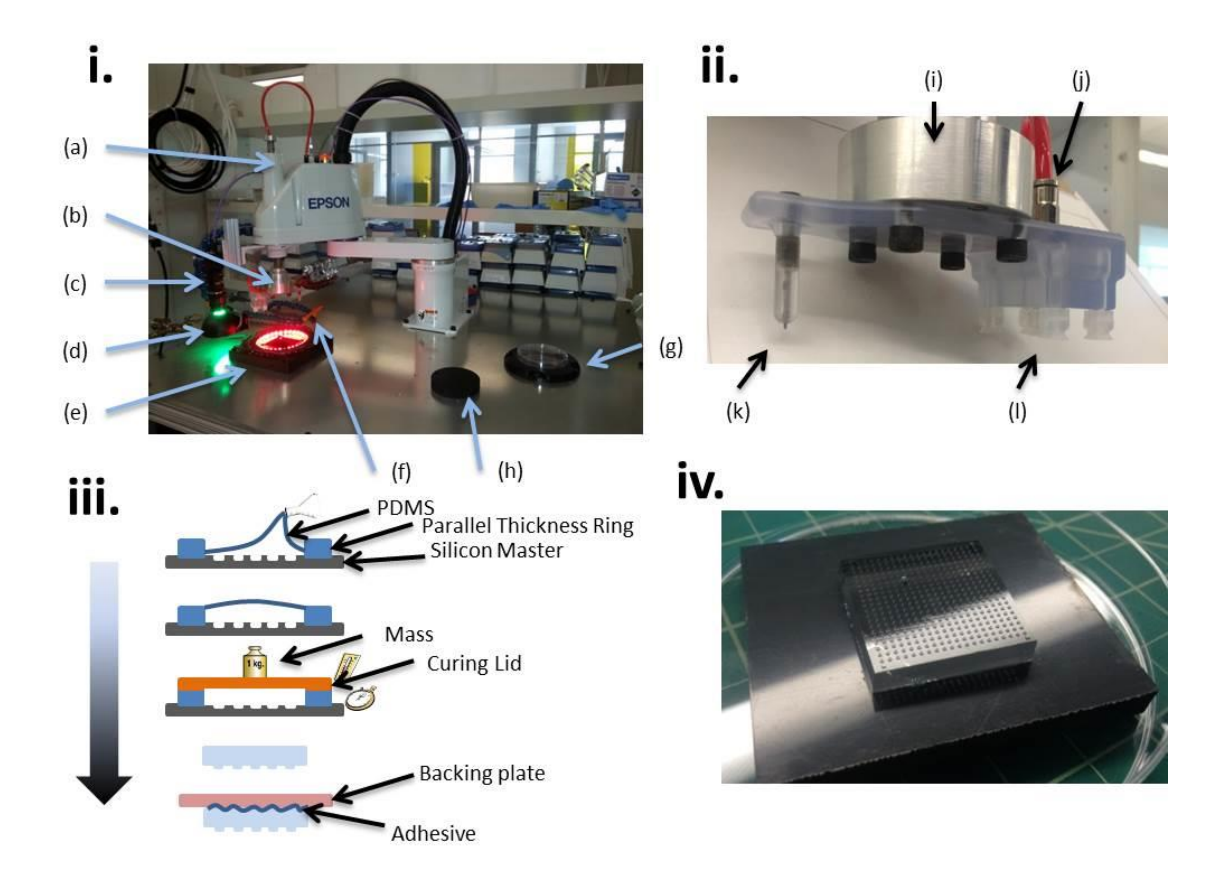


Figure 3.1 Diagram of R- μ CP system and stamp fabrication. (i, a) Epson LS3 SCARA robot. (b) Custom end effector. (c) Downward facing mobile camera. (d) LED diffuse dome light. (e) Custom stamp nesting fixture with LED dark field ring light. (f) Nitrogen drying station. (g) Deposition material nesting fixture. (h) Substrate nesting fixture. (ii, i) Z-axis effector adapter. (j) Vacuum line. (k) Custom spring-loaded diamond tip etching tool. (l) Vacuum cups. (iii) Schematic of PDMS stamp fabrication process proceeding from top to bottom. (iv) Photo of a mounted PDMS stamp.

3.3 Experimental Methods and Materials

3.3.1 Rapid Prototyped and Auxiliary Components

The custom end effector and substrate nesting fixture were fabricated from Accura 60 (3D Systems) using stereolithography (SLA) on a Viper Si2 system (3D Systems). After fabrication, the end effector was attached to the robot through a custom aluminum tooling plate. The stamp and deposition material nesting fixtures were built of ABS using a

Dimension Elite fused deposition modeling machine (Stratasys Ltd.). The custom robot platform was constructed using aluminum T-slot extrusions and expanded polyvinyl chloride paneling (8020 corporation). All lighting, solenoids, flexible nitrogen stream hoses and miscellaneous pieces including auxiliary electronics were acquired from commercial vendors and used as received.

3.3.2 PDMS Stamp Fabrication and µCP

Silicon master molds for fabricating PDMS stamps were designed using AutoCAD and fabricated at the Stanford Microfluidics Foundry. Upon receipt, the master molds were silanized with (Tridecafluoro-1, 1, 2, 2-tetrahydrooctyl) trichlorosilane (Gelest, Inc) to passivate the remaining bare silicon surfaces. Then, Sylgard-184 (Dow Chemical) was cast at a 10:1 monomer: curing agent ratio over the master mold, and degassed under vacuum to create a stamp of uniform thickness. In this study, PDMS stamps with three different feature geometries were used: arrays of 300 μ m diameter posts, annular posts with 300/600 μ m interior/exterior diameters, and annular posts with 600/900 μ m interior/exterior diameters (**Figure 3.2**). In all patterns, the center-to-center spacing between features within each pattern was 1200 μ m.

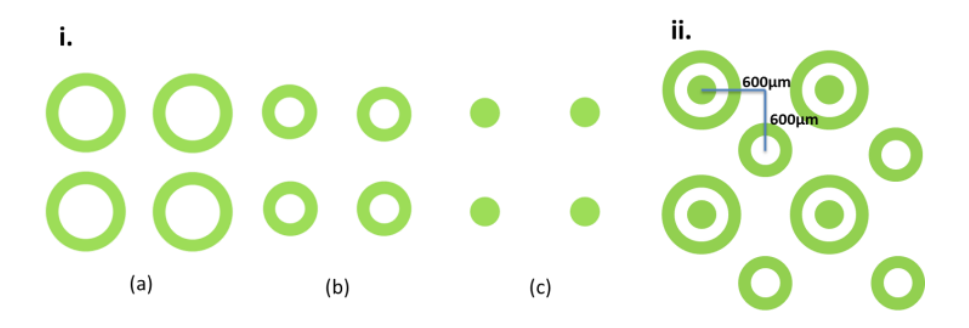


Figure 3.2 Schematic of stamp features and relative offset positioning. (i) Array 1 (a) and 2 (b) annular post with 600/900 and 300/600 µm interior/exterior diameters. (c) Array 3

circular posts with 300 μ m diameters. All arrays contained 1200 μ m inter-feature spacing. (ii) Diagram of offset printing arrangement; arrays 1 and 3 are concentric, and array 2 is printed with a relative 600 μ m X and Y offset.

3.3.3 R-µCP Process

Before stamping, the relative location of the end effector and cameras were calibrated using the Epson RC+ software (SE Corporation). Type 1 glass microscope coverslips (Fisher Scientific) were coated with 35 Å of titanium followed by 180 Å of gold using a CHA-600 Metal Evaporator (Telemark), and the SCARA's end effector, diamond tipped tool was used to etch alignment marks onto the glass substrate. Then a set-up program was executed to train the vision system to recognize etch marks on the substrate and alignment marks (\geq 50 μ m) on all PDMS stamps.

The following steps were performed by the SCARA to pattern alkanethiols onto the gold-coated coverslips. First, an ABS-backed PDMS stamp was placed feature-side down into the stamp nesting fixture, a gold-coated coverslip was secured by vacuum to the substrate nesting fixture, and a 2 mM solution of ω -mercaptoundecyl bromoisobutyrate (Prochimia) in absolute ethanol was placed in the deposition material nesting fixture. Then upon robot program initiation, the robot used the end effector vacuum function to pick up the PDMS stamp and position its features within the LED dark field ring light. Next, the fixed upward facing camera was used to calculate the PDMS stamp's location and orientation by identifying the position of alignment marks in opposite corners of the stamp relative to the robot's global coordinate system. Then in a similar manner, the robot used the downward facing mobile camera to calculate the relative location and orientation of the gold-coated substrates via the previously etched alignment marks.

Once all positions were determined, the SCARA submerged the PDMS stamp's features into the alkanethiol solution such that the entire surface was coated uniformly. Then, the robot positioned the stamp above the nitrogen stream to evaporate the ethanol from the surface of the stamp leaving behind physisorbed alkanethiol molecules. The nitrogen stream was initiated at a pressure of 0.48 bar (7 psi) before being increased to 1.03 bar (15 psi) after several drying passes. Once dried, the stamp was aligned to its calculated position above the gold-coated coverslip, and lowered in 100 µm increments while the SCARA monitored the Z-axis torque at each step. Once the pre-determined conformal contact torque was achieved, the stamp's position was maintained for an additional 15 seconds and then slowly lifted off the glass substrate and returned to its nesting fixture. Upon the release of vacuum pressure by the SCARA, the stamp in the nesting feature was exchanged by hand to a different stamp. This process was repeated to superimpose multiple patterns of immobilized alkanethiols on a single substrate.

3.3.4 Surface-Initiated Activator Generated by Electron Transfer Atom Transfer Radical Polymerization (SI-AGET ATRP) of Oligo(ethylene glycol) methyl ether methacrylate (OEGMEMA)

To visualize superimposed patterns of alkanethiol self-assembled monolayers (SAMs) [134], the SAMs were further modified and fluorescently labeled using previously published protocols [21]. The following materials were used for the modification reactions. Milli-Q water was generated with a Millipore Simplicity 185 system. Copper (II) bromide (99.999% trace metals basis), 2, 2'-Bipyridine (BiPy) (≥99%), L-ascorbic acid, OEGMEMA (Mn=475), sodium azide (NaN3), donkey serum, methanol (for HPLC ≥99%), N,N-

Dimethylformamide (DMF, anhydrous, 99.8%), and dimethyl sulfoxide (DMSO, anhydrous, ≥99.9%) were purchased from Sigma-Aldrich. Streptavidin-Alexa Fluor® 488 conjugate, and Dulbecco's Phosphate-Buffered Saline (DPBS) were purchased from Life Technologies. DBCO-PEG4-Biotin conjugates were purchased from Click Chemistry Tools. OEGMEMA monomer was purified with a basic Al2O3 column to remove the inhibitor.

After patterning a gold-coated substrate with a one or more ω -mercaptoundecyl bromoisobutyrate SAMs using R- μ CP, the coverslip was removed from the system, and modified using SI-AGET ATRP to graft poly(ethylene glycol) methyl ether methacrylate (PEGMEMA) brushes from the SAMs. Then, the brushes were functionalized and conjugated with fluorescent molecules to facilitate imaging.

For PEGMEMA grafting, water (7.5 mL), methanol (7.5 mL), the macromonomer OEGMEMA (8 g, 16.7 mmol), 2'2-Bipyridine (0.24 mmol, 37.5 mg), and copper (II) bromide (0.08 mmol, 17.9 mg) were added to a sealed Schlenk flask, mixed, and degassed with three freeze-vacuum-thaw cycles. Next, the mixture was transferred to a reaction flask containing a micropatterned glass slide under vacuum. L-ascorbic acid (0.8 mmol, 140.9 mg) in deionized water was injected into the flask to start the reaction, and the reaction continued for 16 h under nitrogen. Polymerization was halted by adding air, and the slides were cleaned with ethanol, water, and ethanol before drying under nitrogen.

3.3.5 Fluorescent Modification of Grafted PEGMEMA Brushes

After polymerization, the PEGMEMA brushes could be viewed under brightfield microscopy, and were micropatterned identical to the PDMS stamp's feature geometry. For enhanced contrast to facilitate computerized analysis of their geometry, fluorescent images of

the PEGMEMA brushes were desired. Thus, the terminal bromine group on the PEGMEMA brush was azide substituted using 0.1 M sodium azide/DMF solution at 37 °C for 24 h (unless stated otherwise), followed by rinsing with water and ethanol and drying with nitrogen. Then, the coverslip was immersed in 10 µM DBCO-PEG4-Biotin/DPBS solution for 6 h at room temperature to induce strain-initiated, copper-free click immobilization of biotin molecules onto the PEGMEMA brushes. After the reaction, the slide was again rinsed with water and ethanol, and dried using nitrogen. Next, the coverslip was incubated for 1 h in 1 mL of 3% donkey serum/DPBS solution followed by an additional 2 h incubation after adding 20 µl of 2 mg/ml Streptavidin-Alexa Fluor® 488 or 546 (Life Technologies), which binds to immobilized biotin molecules. Light was avoided during this reaction. Finally, the coverslip was rinsed with Tris-buffered saline (TBS, pH 7.4) twice for 10 min, and once more in 1% Donkey Serum/DPBS for 1 h before being imaged with a Nikon A1R confocal microscope.

3.3.6 Computerized Pattern Analysis using MATLAB

To obtain non-biased accuracy and precision measurements for R- μ CP, confocal images of fluorescent micropatterned coverslips were analyzed using a custom MATLAB program (described later). After image analysis, the program outputted the relative X, Y, and angular (θ) error between each μ CP step.

3.3.7 Cell Culture and Staining Procedure

Human embryonic stem cells (line WA09) were transfected by electroporation (Bio-Rad Gene-Pulser) with three plasmids: hCas9 (Addgene 41815), a guide RNA plasmid targeting the AAVS1 safe harbor site (Addgene 41818), and a GFP plasmid with AAVS1

homology. The cells were subjected to puromycin selection and verified under microscopy for constitutive green fluorescence. To differentiate the cells into neural stem cells (NSCs), a previously describe method was used [158]. Briefly, cells were seeded at 2×10^5 cells/cm² on Matrigel coated plates (BD Bioscience) in E6 media. Media was changed daily for 6 days upon which they were seeded onto patterned slides at 1×10^5 cells/cm² in E6 media containing $10~\mu$ M Y-27632 (R&D Systems) and 8μ g/mL mouse laminin (Life Technologies). After attachment, slides were incubated with $10~\mu$ M DBCO-PEG4-Biotin/DMF (Click Chemistry Tools) in E6 media for 2 hours. After incubation, the slides were washed 3 times with PBS and cells were then fixed in 4% paraformaldehyde (PFA) in PBS for 15 minutes. The slides with cells were then washed 3 times with PBS and then fluorescently stained with Streptavidin-Alexa Fluor® 546 conjugate and DAPI as discussed earlier.

3.4 Results and Discussion

In order to determine the accuracy and precision of the R-μCP system, stamps featuring Arrays 1, 2, and 3 (**Figure 3.2i**) were used to consecutively pattern ω-mercaptoundecyl bromoisobutyrate SAMs onto gold-coated coverslips in an offset arrangement (**Figure 3.2ii**). After R-μCP all three stamps, the coverslips were grafted with PEGMEMA brushes, fluorescently modified, and imaged using confocal microscopy (**Figure 3.3i**). Then, measurements of accuracy and precision were obtained by image analysis using a custom MATLAB program.

In the MATLAB program, images of the entire coverslip were subjected to a threshold filter to binarize the data, thereby providing distinct regions of interest (ROIs) that the software was able to numerically analyze. Then, the ROIs were divided into separate

arrayed populations based on their morphological properties (denoted in **Figure 3.2i**) with each feature population corresponding to a single stamping event. Next, the program determined the centroids of each feature, and performed a nearest-neighbor analysis to compare the locations of each feature within Array 1 to their respective counterparts in Arrays 2 and 3. From this analysis, a transformation matrix was determined utilizing Horn's Method for absolute orientation [159], including both translational and rotational components, maximizing the overlap of the multiple arrays and reducing the root-mean-squares distance between nearest-neighbor features. Then, the program outputted the accuracy as a relative rotational and translational error between Array 1 vs. 2 and 1 vs. 3 based on the user's pre-defined stamping offset values. Estimates of the R-μCP systems' precision was obtained by calculating the standard deviation between experimental replicates.

Image analysis of our initial offset stamping experiment (Trial 1, **Figure 3.3i**) estimated the R-μCP system's translational accuracy to be greater than 20 μm in the X and Y directions, and the rotational accuracy to be as high as 0.18° (**Figure 3.3iii and iv**). This is significantly higher than expected, and therefore, we postulated that each custom robot modification, tool, and PDMS stamp could introduce implicit alignment errors into the system. Thus, it was hypothesized that if these compounded errors are taken into account as compensation values, then one could possibly improve the R-μCP system's accuracy.

Based on the error values estimated in Trial 1 as compensation offsets for each PDMS stamp featuring either Array 2 or 3, a second trial of the same experiment was repeated (**Figure 3.3ii**). MATLAB image analysis of photos from Trial 2 indicated that the R-µCP system's translational accuracy and precision in both the X and Y direction were

significantly reduced and consistently <10 μ m when compensation was programed into the SCARA's alignment code (**Figure 3.3iii** and **iv**). The rotational accuracy also became more consistent and was reduced to <0.07°. Thus, the translational accuracy and precision of the R- μ CP system appears to be approaching the limitations of the employed SCARA model, but additional protocol or machine modifications may be necessary to further increase the rotational accuracy. Furthermore, this highlights the need to execute an initial calibration run to fine tune stamp alignment before proceeding to use of R- μ CP for mass-producing patterned substrates.

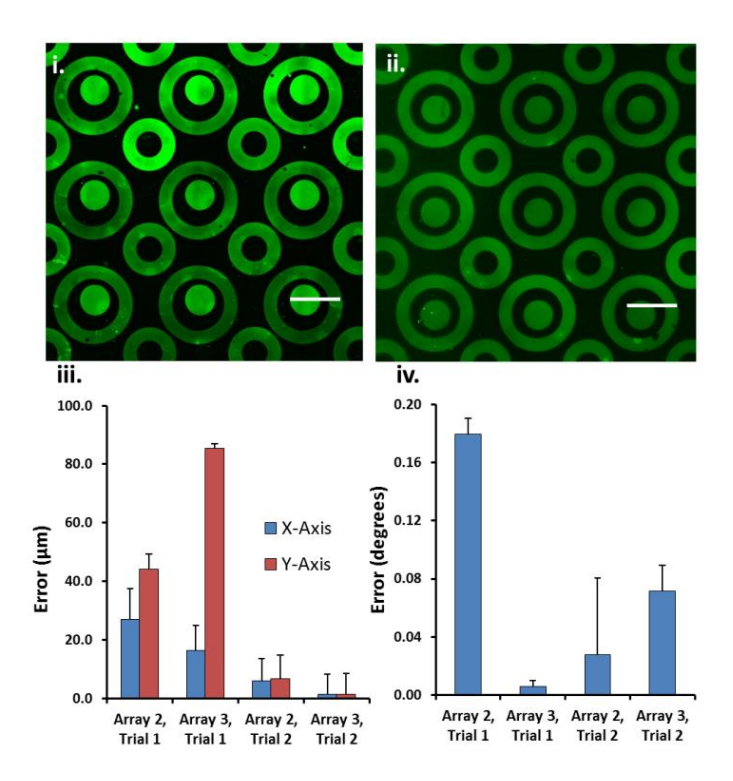


Figure 3.3 Micropatterned coverslip images and estimated R- μ CP accuracies. (i) Image of Trial 1, pre-compensation and (ii) Trial 2, post-compensation R- μ CP results. Scale bars are 500 μ m. Non-biased estimates of (iii) translational and (iv) rotational accuracies for each stamped feature array relative to Array 1. * indicates p < 0.05, Student's T-test, n = 3.

Prior systems designed to align and superimpose multiple μ CP steps require constant substrate fixation throughout the entire patterning process to achieve high degrees of

precision [154, 156]. This limits the diversity of chemical modifications, and thereby structural complexities, which can be engineered into micropatterned culture substrates. To determine whether this was also a limitation of R-µCP, we compared the results of coverslips concentrically patterned with stamps presenting feature Arrays 1, 2, and 3 both without (Trial 3) and with (Trial 4) removal of the coverslips between each µCP step (Figure 3.4i and ii, respectively). For coverslips that were periodically removed from the R-µCP system (Trial 4), each stamping was followed by removal, reaction to graft a PEGMEMA brush to the most recently printed alkanethiol SAMs, and functionalization of that brush by reacting the coverslip with sodium azide for 4 hours. It has been previously demonstrated the reaction kinetics for azide functionalization of PEGMEMA brushes, and that a 4 h reaction will only partially substitute the brush's terminal bromine groups [21]. Therefore, the PEGMEMA brushes formed on coverslips with removal between each µCP (Trial 4) will have variable levels of azide functionalization due to variable sodium azide exposure durations (i.e. brush corresponding to Array 1 (stamped first), 12 h; Array 2, 8 h; Array 3, 4h). In contrast, coverslips not removed between each µCP step (Trial 3) were grafted with PEGMEMA brushes that were reacted with sodium azide once and for a uniform duration of 8 h. Thus upon biotin immobilization and Streptavidin Alexa Fluor® 488 staining of the coverslips, the PEGMEMA brushes that correspond to stamps featuring Array 1, 2, and 3 will have decreasing fluorescent intensities on coverslips that were removed between each µCP step (Trial 4) but similar intensities on coverslips that were not removed between each µCP step (Trial 3).

As compared to the prior results (**Figure 3.3iii** and **iv**), it was observed that there was no significant decrease in the accuracy and precision of R-µCP when the substrate was

removed from the system between μ CP steps (Trial 4). Furthermore, a line scan across the concentric PEGMEMA brushes on a coverslip corroborated the ability to differentially modify each PEGMEMA pattern using R- μ CP while still maintaining high accuracy and precision (**Figure 3.4iii, iv** and **v**). Thus, unlike previous systems, R- μ CP is not limited by the need for constant substrate fixation throughout the entire multi-patterning process.

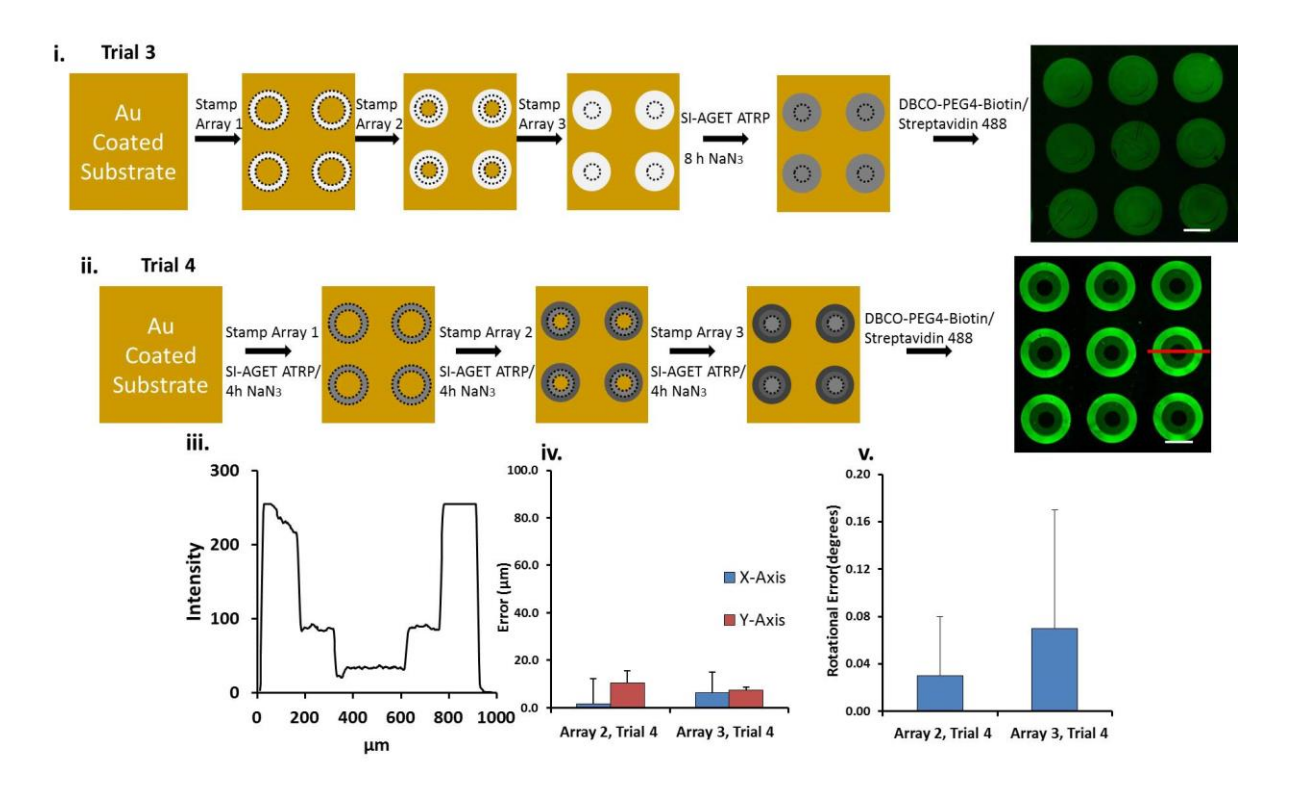


Figure 3.4 Evaluating R- μ CP's need for constant substrate fixation. Procedural illustrations and representative images of coverslips patterned (i) without and (ii) with substrate removal between each μ CP step. Scale bars are 500 μ m. (iii) Intensity profile of line scan (red) across a single concentric pattern in (ii), which indicates 3 distinct intensities corresponding to each stamped feature array. Non-biased estimates of (iv) translational and (v) rotational accuracies for each stamped feature array relative to Array 1, n = 3.

To further demonstrate the utility of $R-\mu CP$, the system was used to engineer a complex cell culture environment on gold coated coverslips. Specifically, a PEGMEMA brush using stamps featuring Array 1 was grafted and azide functionalized. Subsequently, a

second PEGMEMA brush was concentrically grafted using stamps featuring Array 2, and allowed the terminal bromine groups on this brush to persist (Figure 3.5i). Upon seeding the substrate with GFP+, human pluripotent stem cell-derived neural stem cells (NSCs), the cells adhered to all parts of the culture substrate except for those presenting PEGMEMA brushes. Furthermore, due to heterogeneous functionalization of the PEGMEMA brushes, we were able to selectively modify the culture substrate's surface chemistry in a spatiotemporal and in situ manner using the simple addition of DBCO-PEG4-biotin to the cell culture media. Upon addition, DBCO-PEG4-biotin spontaneously reacts with the azide functionalized PEGMEMA brush patterned by Array 1 without affecting the surface chemistry of any other part of the culture substrate, thereby creating a culture substrate with three different surfaces chemistries: cell adhesive gold-coated coverslip background regions, a non-cell adhesive PEGMEMA brush patterned by Array 2, and a non-cell adhesive, biotin presenting PEGMEMA brush patterned by Array 1. Then, upon fixation of the entire slide, we showed selective immobilization of biotin using Steptravidin-Alexa Flour 546 immunostaining (Figure 3.5ii). In future applications, biotin could be replaced with a cell adhesive peptide to allow facile and microscale spatiotemporal control of cell adhesion during in vitro culture.

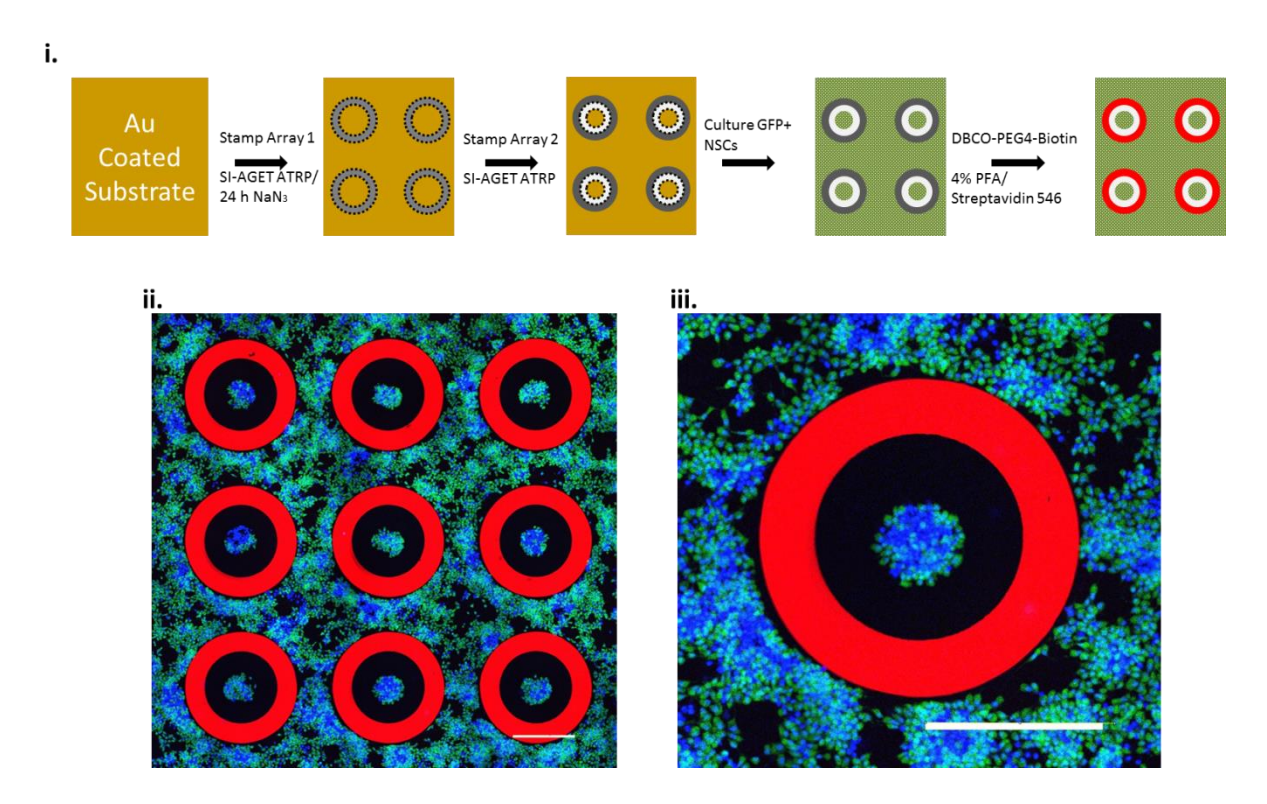


Figure 3.5 Engineering complex cell culture environments. (i) Schematic of experimental process to graft PEGMEMA brushes with heterogeneous functionalities, i.e. a terminal bromine group vs. a terminal azide group, seed GFP+ NSCs, and then modify PEGMEMA brush array 1 in situ with a clickable biotin ligand. Post-fixation, the presence of biotin was detected using streptavidin-546 staining. (ii) Low-magnification and (iii) high-magnification representative images of the complex culture environment post streptavidin-546 staining. Scale bars are 500 μm.

3.5 Conclusions

The results from this study demonstrate that the current R- μ CP system can align and print superimposed patterns of molecules using PDMS stamps with <10 μ m accuracy and precision. While this represents a μ CP error less than the size of a human cell, it is believed that the accuracy and precision of R- μ CP could be further enhanced if a higher-end SCARA robot was employed. With such as substitution, it could be predicted that the accuracy and precision of the system would be less than the ~7 μ m shown in this work. Utilizing higher resolution cameras coupled with higher quality lighting might also reduce the R- μ CP error.

Furthermore, recent studies have demonstrated a μ CP lift-off procedure that can be used to generate arrays of features as small as 40 nm in diameter [151]. It should be noted that a high-end SCARA based system with nanometer Z-axis resolution could generate such patterns with similar accuracy as long as appropriately sized alignment marks are included in the 40 nm featured stamp design.

Major advantages of the R-μCP method are the flexibility that it provides in PDMS stamp fabrication and substrate handling as well as scalability due to automation. Users can continue to use their pre-existing PDMS stamps, transparent or opaque, without the need to modify their fabrication methods due to the required usage of precisely machined molds. Additionally, R-μCP's vision integration allows for substrates to be removed from the fixture between μCP steps, thereby increasing the diversity of materials and surface chemistries that can be engineering onto custom culture substrates. Future applications of R-μCP could be used to engineer biomimetic culture substrates that contain the spatial heterogeneity of microenvironmental cues observed within *in vivo* tissues. Moreover, the use of R-μCP to accurately pattern substrates relative to a reference point will facilitate integrating such engineered culture substrates with microfluidics, thereby further enabling the scalable manufacturing of novel *in vitro* assays and microarray screening technologies.

4 Increasing Uniformity of Substrates Produced Via R-μCP

While the R- μ CP system introduced in the previous chapter has demonstrated the ability to perform multiple sequential, precise and accurate patterns on a single substrate, a noticeable non-uniformity in deposition density can be observed (**Figure 4.1**). This is a common issue when performing any form of μ CP and is typically amplified with larger surface area stamps and substrates. The aim of this chapter is to highlight the key factors which cause the non-uniformity with R- μ CP and provide innovative solutions which will increase the consistency and performance of the process.



Figure 4.1 Example image of concentrically patterned features on a microscope coverslip produced with $R-\mu CP$

A thorough examination of the entire R- μCP process highlighted two primary origins of the deposition non-uniformity.

- Non-flat/parallel stamps
- Lack of a conforming end effector

As the video published in the JOVE (Journal of Visual Experiments) journal demonstrates, that when performing a R-µCP printing operation, the Z axis of the robot moves straight down until the stamp is in contact with the substrate [160]. If however the stamp is not parallel on the top and feature side of the PDMS, this can result in over and under-patterned regions of the substrate (**Figure 4.2**). Being that the stamp was mounted to a rigid end effector this issue was compounded causing deformation of the lowest features and allowing contact of the feature background during pattering.

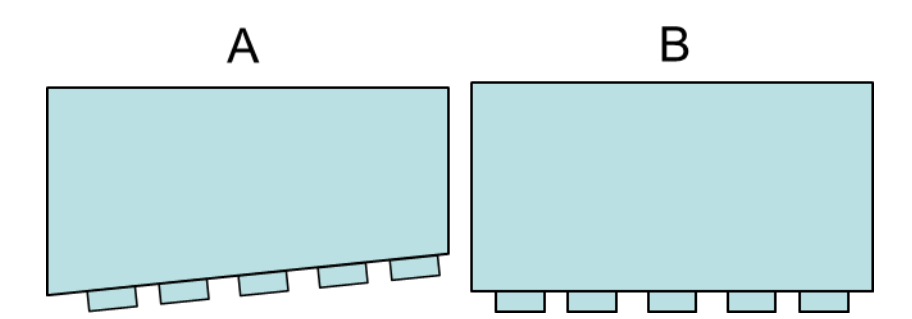


Figure 4.2 Illustration of (A) non-flat/parallel stamp and (B) parallel stamp cross sections

To mitigate the issue, the stamp fabrication process was modified, an adjustable stamp holder was created and a spring assisted conformal end effector was built. Specifically, to prevent shrinkage and residual stresses – and ultimately a concave surface – the stamp fabrication protocol was modified from the earlier version by eliminating the curing lid step and ensuring the feature array was a minimum of 4.5 mm from the parallel thickness ring to

account for meniscus effects (3× characteristic capillary lengths of PDMS). The adjustable stamp holder was designed with 4× micro-adjustable screws (M3×0.2) threaded through brass bushings in the 4 corners of a rectangular aluminum plate (**Figure 4.3**). The micro-adjusters were then calibrated into a hard-stop position allowing for the PDMS features to come into contact with the substrate, but preventing any background transfer, regardless of stamping force. A standard 8-32 set screw was also added into the center of the aluminum stamp holder to adjust for any concave surfaces due to PDMS shrinkage during curing.

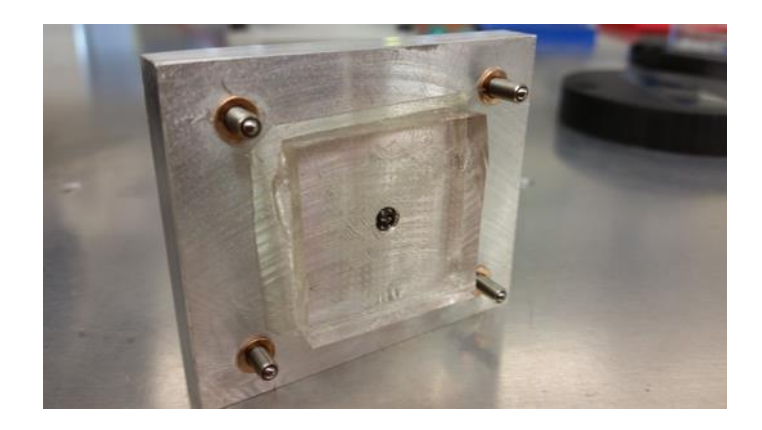


Figure 4.3 Modified stamp holder with 4× micro-adjusters and center screws.

Lastly, the rigid end effector was replaced with a spring assisted conformal end effector which would self-level onto the substrate nesting fixture and eliminate any system non-perpendicularity (**Figure 4.4**).

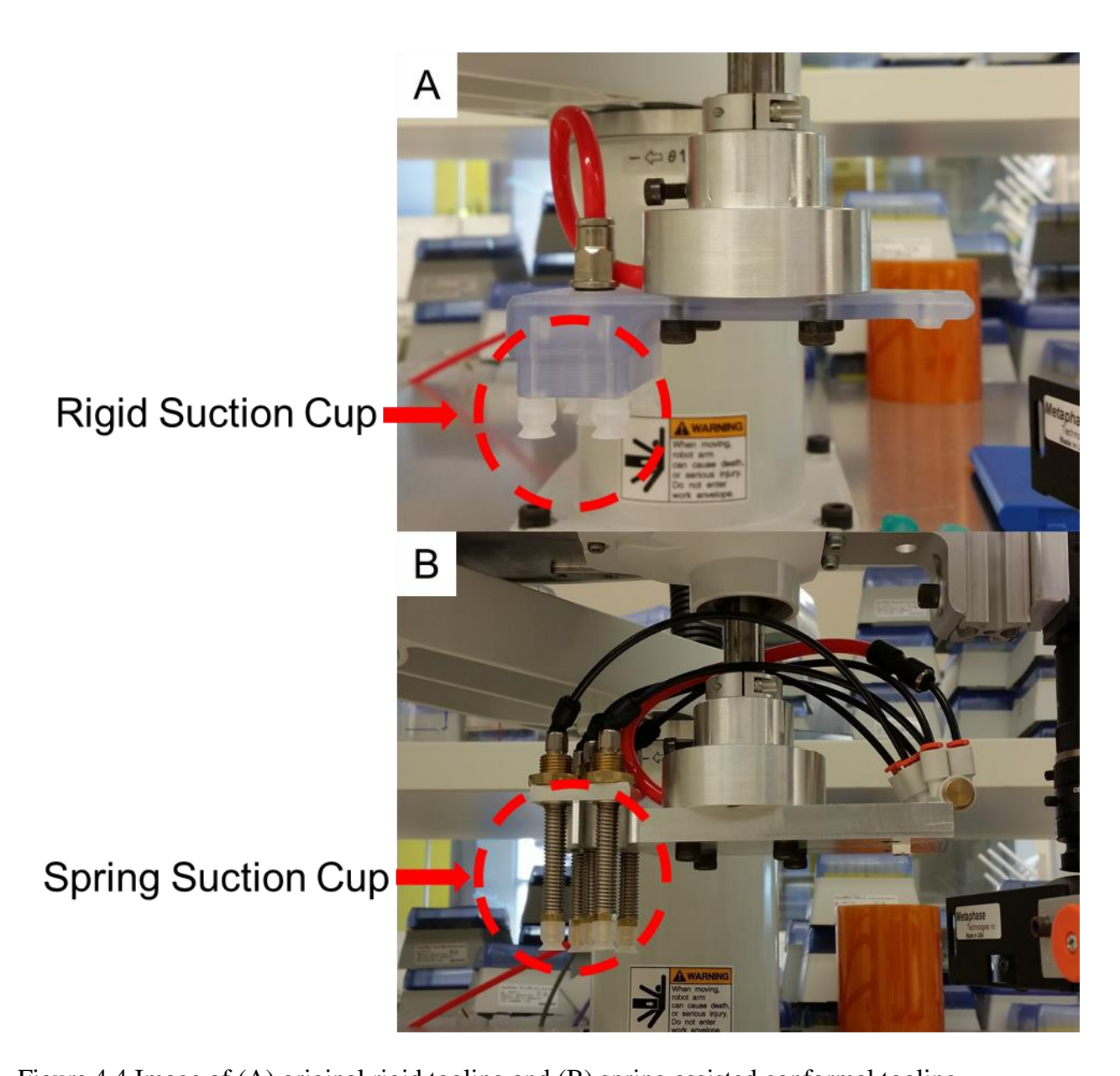


Figure 4.4 Image of (A) original rigid tooling and (B) spring assisted conformal tooling.

Next a simple comparison experiment was carried out by patterning microscope coverslips with the traditional hand stamping (H), original R- μ CP tooling (O) and new spring assisted R- μ CP tooling/stamp holder (S) in 2 groups, 1) with a non-parallel stamp and 2) parallel stamp as described in **Figure 4.2**. Similar to the previous chapter, the patterned regions were then fluorescently functionalized, imaged using confocal microscopy, and

analyzed with MATLAB in order to assess the uniformity of microcontact printing by evaluating each pattern's fluorescent intensity (average and standard deviation of each feature) over the entire substrate(cf. **Figure 4.5**).

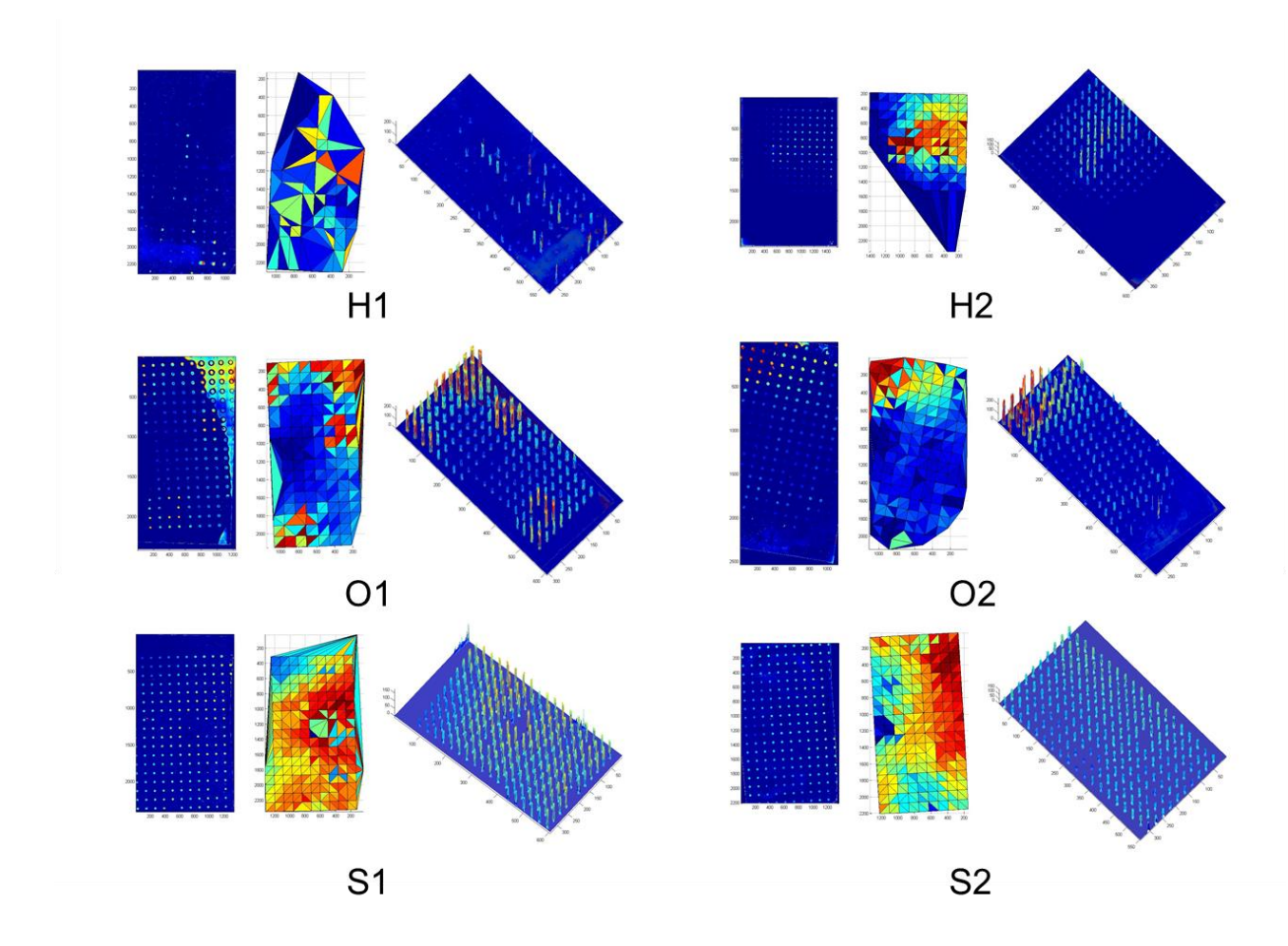


Figure 4.5 MATLAB graphical images of the experiment between patterning techniques/tools.

The MATLAB program was designed to import a high-resolution stitched image from the Nikon file format and perform automated image analysis of the fluorescent patterns. Specifically, the code was used to identify each fluorescent island as a unique ROI, record all ROI intensities and calculate the overall average and its average intensity. Confirming the

visual observations, the box and whisker plot in **Figure 4.6** shows that the new spring tooling has less variation in fluorescent intensity when compared to both hand stamping and the original tooling regardless of stamp quality.

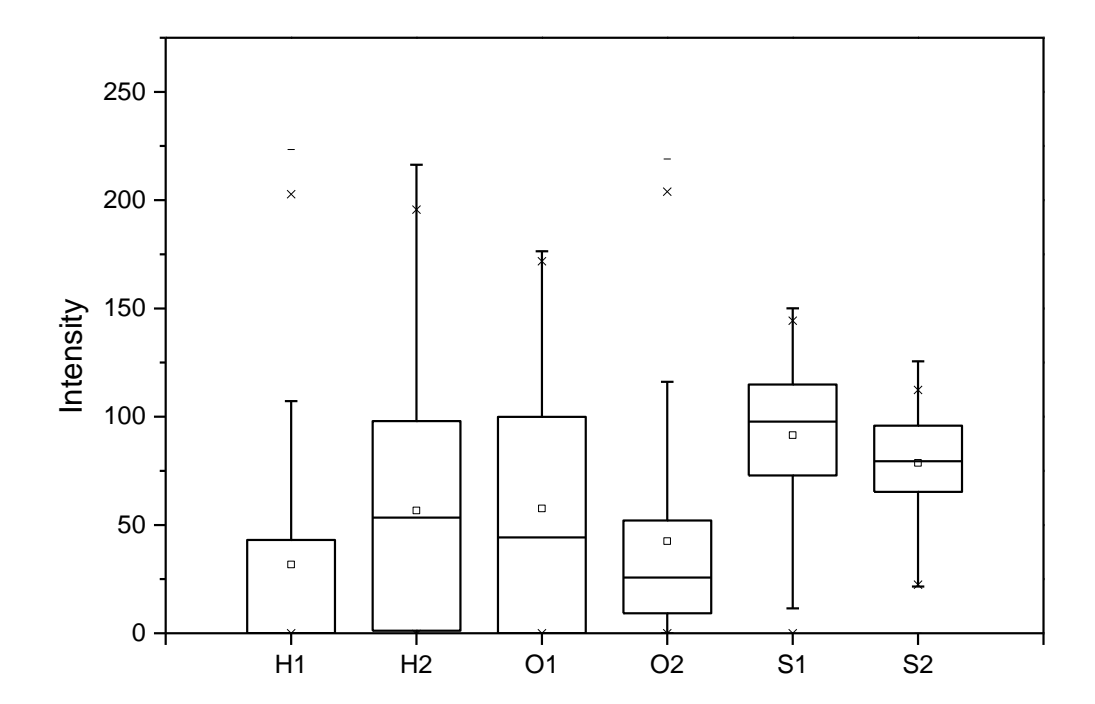


Figure 4.6 Quantitative data of the fluorescent intensity vs. sample production technique (n=3 printed samples per method)

4.1 Conclusion

In a separate journal article, we previously demonstrated the ability to produce micropatterned substrates in traditional well plate formats [161]. While successful, the procedure made use of a simple guide system for hand stamping the micro-features with 1 extra-large PDMS stamp. The R-µCP system has since been programed to produce accurate, precise and uniform substrates with the standard PDMS stamps. This technological feat coupled with the systems increased microscale uniformity will allow an unprecedented level of experimental control within industry standard culture formats.

5 Fabrication of Microchannel Networks within Alginate Hydrogels Using Sacrificial Injection Molding Techniques

Sacrificial molding of hydrogel monoliths is a versatile technique for making 3D scaffolds with microchannel networks that regulate tissue morphology in tissue engineering applications. Previous sacrificial materials fabricated by serial processes such as solvent casting and thermal extrusion/fiber drawing can be used to effectively mold internal geometries within rapidly polymerizing, bulk curing hydrogels. However, they display poorer performance in controlling the geometry of diffusion limited, ionically cross-linked hydrogels. Here, we describe the use of poly(vinyl alcohol)-calcium salt templates (PVOH-Ca) fabricated by micro-injection molding, a mass-production process, to conveniently cast internal geometries within both bulk curing hydrogels and ionically cross-linked alginate hydrogels. Calcium salt solubility was discovered to be a critical factor in optimizing the polymer composite's manufacturability, mechanical properties, and the quantity of calcium released upon template dissolution within the hydrogels. Metrological and computed tomography (CT) analysis showed that the template's calcium release enables precise casting of microscale channel geometries within alginate hydrogels (6.4 \pm 7.2% average error). Additionally, the assembly of multiple modular PVOH-Ca templates to mold 3D channel networks within alginate hydrogels is presented to demonstrate process scalability and versatility. Thus, injection molded PVOH-Ca templates as sacrificial, calcium-releasing inserts should facilitate implementation and customization of hydrogel sacrificial molding in diverse tissue engineering applications.

5.1 Introduction

Hydrogel biomaterials are used throughout the field of tissue engineering as versatile scaffolds to support three-dimensional (3D) cell growth and shape the morphology of tissue constructs [1, 7, 8, 162-164]. In vivo, normal tissue development and physiology relies upon proper cytoarchitectural organization at multiple length scales. Hence, several methods have been developed for engineering the macro-to-microscale architecture of hydrogel scaffolds, including layer-by-layer 3D printing technologies, such as fused deposition modeling (FDM) and stereolithography (SLA) [23-25, 165]. Recently, these methods have been used to fabricate sacrificial templates that enable unprecedented, rapid casting of intricate architectures within hydrogel monoliths [166, 167]. For example, Miller et al. used a FDM printer to create interconnected 3D lattices composed of water-soluble carbohydrate glass filaments [110]. Subsequently, the lattices could be encapsulated within hydrogels, and upon dissolution, leave behind channel networks suitable for generating microvasculature within prospective 3D tissues. Alternatively, sacrificial poly(vinyl alcohol) (PVOH), alginate, gelatin, and polyethylene glycol (PEG) templates casted within SLA fabricated molds have also been developed to engineer microscale hydrogel architecture [168-171].

While these approaches enable rapid casting of complex hydrogel architectures, the fabrication techniques and sacrificial template materials impose several limitations. First, the FDM and SLA/solvent casting fabrication techniques are not scalable for mass production due to extended manufacturing cycle times per sacrificial template. Second, the carbohydrate glass template's reported mechanical properties indicate its brittle and inelastic nature, suggesting limited durability during normal handling, whereas those of the PVOH and

alginate templates were not directly determined. Third, current template materials have only been proven to effectively cast complex geometries within bulk curing hydrogels such as PEG, fibrin, and methacrylated gelatin. Poorer dimensional accuracy was observed when Miller et al. used carbohydrate glass lattices to cast channels within diffusion limited, ionically crosslinked alginate hydrogels, a widely used tissue engineering scaffold and clinically approved biomaterial [110, 168, 172-174]. Alginate in particular has several advantageous biomaterial properties for tissue engineering applications: facile and gentle cell encapsulation, ease of chemical modification via densely presented carboxylic acid groups on its polymer backbone, and enzymatic degradation mechanisms that are orthogonal to the mammalian genome [172, 173, 175, 176]. Thus, there remains a need to develop a scalable mass production process for generating durable sacrificial templates capable of accurately casting architectural features within both bulk curing and diffusion limited, ionically crosslinked hydrogels.

To address these limitations, we have developed micro-injection molded PVOH-calcium salt composites (PVOH-Ca) as enhanced sacrificial templates for engineering hydrogel architecture (**Figure 5.1**). Injection molding processes are unmatched in manufacturing scalability due to their automated, parallel production of finished polymer components within seconds [72, 177, 178]. Interestingly, calcium salt solubility was discovered to be a critical parameter in optimizing the PVOH-Ca's micro-injection molding processability and the resulting templates' handling durability and casting precision. Calcium acetate (Ca(C₂H₃O₂)₂) was determined to induce optimal PVOH-Ca composite mechanical properties, and its release upon template dissolution accelerated the curing rate of alginate hydrogels at the template/hydrogel interface. PVOH-Ca(C₂H₃O₂)₂ templates were observed

to cast 500 μ m diameter features within alginate monoliths with only a 6.4 \pm 7.2% average error, and equivalent performance was observed within bulk curing polyacrylamide hydrogels. Also, to demonstrate process scalability and versatility, modular PVOH-Ca(C₂H₃O₂)₂ templates were injection molded, assembled into multicomponent Lego®-like structures, and used to generate 3D channel networks within alginate and polyacrylamide hydrogels. Overall, these results demonstrate the mass-production, utility, and versatility of PVOH-calcium acetate templates for sacrificially molding custom architectures within hydrogels used for tissue engineering applications.

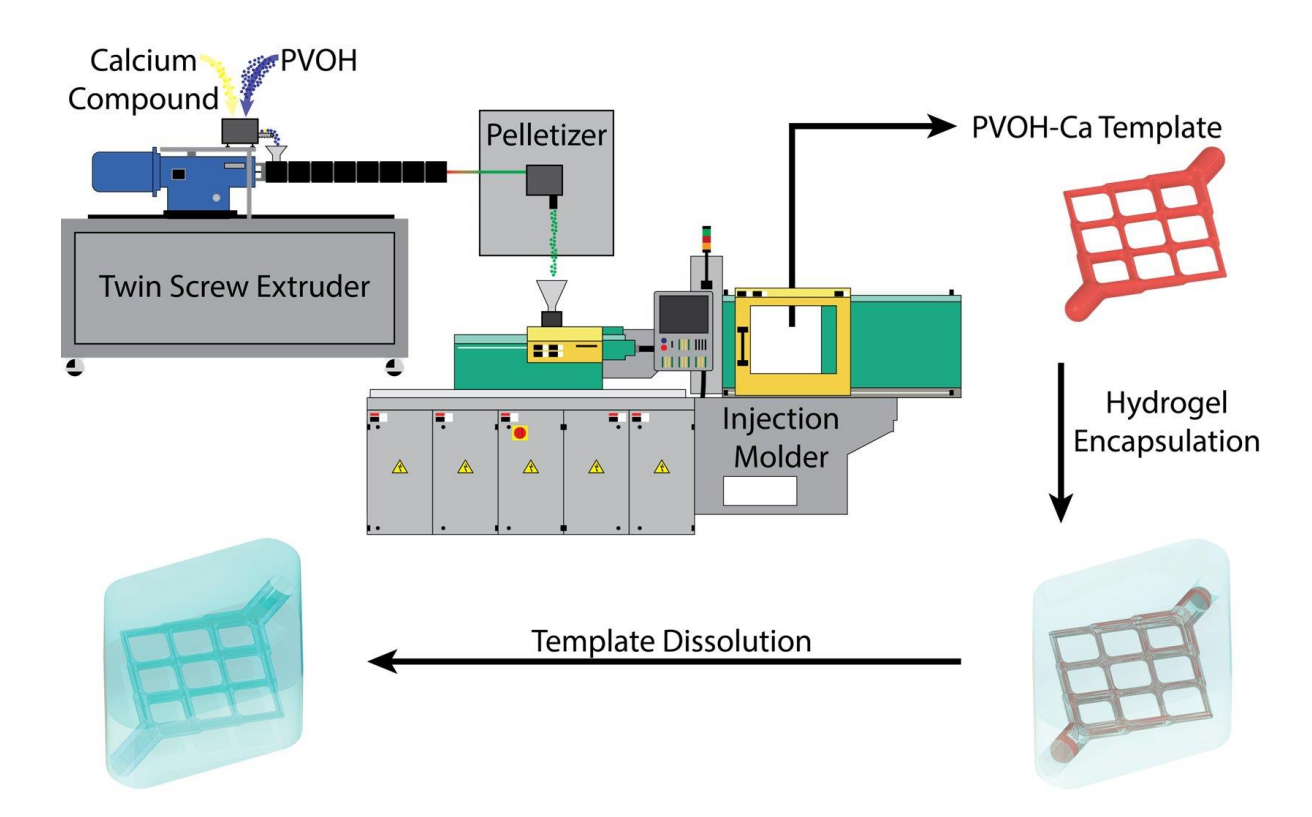


Figure 5.1 Illustration of PVOH and calcium salt compounding followed by injection molding of a sacrificial PVOH-Ca template, which is subsequently encapsulated and dissolved within a hydrogel matrix.

5.2 Materials and Methods

5.2.1 Materials

Pronova SLG1000 sodium alginate was purchased from Pronova Biopolymer. Calcium salts (e.g., CaCO₃, Ca(C₃H₂O₂)₂, CaI₂ and CaCl₃), Eriochrome Black T, Ammonium Chloride, and Magnesium Chloride were purchased from Sigma Aldrich. Calcium sulfate and ammonia were purchased from Acros Organics. Polyacrylamide, tetramethylethylenediamine (TEMED), and ammonium persulfate were purchased from Biorad. Functionalized PEGnorbornene hydrogel materials were kindly provided by Prof. William Murphy (UW–Madison). Polypropylene 6061 aluminum and 316 stainless steel raw materials were purchased from McMaster-Carr Supply Company. Dexron-VI automatic transmission fluid (ATF) was purchased from Autozone and used as the imaging contrast dye for alginate perfusion.

5.2.2 Extrusion Compounding

Calcium salts were ground via mortar and pestle and sieved until less than 300 µm in dimension. The salts were hand mixed with PVOH (Monopol C100, Monosol Inc.) and conditioned under vacuum at 70 °C for 4 hours. The mixture was fed through a volumetric feeder (Tuf-Flex 100, Schenck Accurate) into a co-rotating twin screw compounding extruder (18 mm Leistritz AG) equipped with a screw designed with only feedforward elements and a 6 mm strand die (**Figure 5.1**). Post compounding, the extrudate was run through a pelletizer to prepare the composite for injection molding. Compounding parameters are listed in Table 5-1.

Table 5-1 Twin screw extrusion and microinjection molding processing parameters.

Twin Screw Extruder Processing Parameters	
Zone 1 (°C)	160
Zone 2 (°C)	165
Zone 3 (°C)	170
Zone 4 (°C)	173
Zone 5 (°C)	175
Zone 6 (°C)	177
Zone 7 (°C)	178
Zone 8 (°C)	180
Load (%)	< 40
Screw Speed (rpm)	50-70
Injection Molding Process Parameters	
Mold temperature (°C)	46
Barrel temperature (°C)	190-200
Injection pressure (bar)	1250-1400
Holding pressure (bar)	1000
Injection speed (cm ³ /s)	55
Holding time (s)	2
Cooling time (s)	20

5.3 Mechanical and Thermal Analysis

Tensile properties of injection molded PVOH and PVOH-Ca composites in forms of the ASTM D638 Type V tensile bars were measured using an Instron 5967 Universal Tensile Testing Machine (30 kN) elongated at 50 mm/min [31]. Thermogravimetric analysis (TGA) was performed on PVOH-Ca composite samples ranging from 20-60 mg with platinum pans (DSC Consumables Inc.) ramped to 600 °C at 10 °C/min (Q50 TGA, TA Instruments). Differential scanning calorimetry (DSC) was performed using hermetic aluminum pans (DSC Consumables Inc.) between 0 and 210 °C at a ramp rate of 10 °C/min (Auto Q20, TA Instruments). Viscosity characterization was performed with a parallel plate rheometer (AR2000, TA Instruments) using injection molded discs (24.5 mm diameter, 2 mm thick).

5.4 Injection Molding

Custom injection molds were designed with 3D modeling software (Solidworks 2014, Dassault Systemes) and fabricated from 6061 aluminum with a computer numerical control (CNC) vertical machining center (MiniMill 2, Haas) programmed with computer aided design/manufacturing (CAD/CAM) software (MasterCAM X7, CNC Software, Inc.). All injection molding was performed on a 38 ton Arburg Allrounder 270A machine with an 18 mm injection unit with processing parameters found in Table 5-1.

5.5 Complexometric Calcium Titration

A complexometric titration was performed to quantify the amount of Ca ions released from PVOH-Ca templates upon dissolution. First, 1.4 g of each composite was completely

dissolved in 50 ml of deionized water. Second, 100 mL of 50 mM ethylenediaminetetraacetic acid (EDTA) was added to the solution to chelate all free Ca atoms. Third, eriochrome black T (EBT), a weaker chelating agent used as an indicator, was added to the solution causing a blue color that changes to pink upon its complexing with cations. Then, MgCl₂ was titrated in the solution to react with the excess EDTA to completion, which was indicated by the solution's color change due to Mg's reaction with EBT. In this manner, we could calculate the amount of Ca released upon PVOH-Ca template dissolution from the amount of MgCl₂ added. For each template composition, the titration results were compared with the total Ca salt content detected by thermogravimetric analysis (TGA).

5.6 Hydrogel Fabrication

5.6.1 Polyacrylamide

Polyacrylamide hydrogels were fabricated within a custom-made polypropylene device that suspended PVOH templates between inlet and outlet needles. Five milliliters of 12% acrylamide/bisacrylamide was prepared, and 100 μL of ammonium persulfate and 4 μL of TEMED were added to initiate the bulk polymerization reaction. After 5 min, the polyacrylamide solution was added to the device to completely cover the PVOH templates. The solution was allowed to polymerize for one hour to form a hydrogel around the templates. The device was transferred to a water bath at 45°C and incubated overnight for PVOH dissolution.

5.6.2 Polyethylene Glycol (PEG)

PEG-norbornene (PEG-NB) hydrogels were fabricated within a custom-made polypropylene device that suspended PVOH templates between inlet and outlet needles. In particular, 4.5 milliliters of 4% (w/v) PEG-NB was prepared to achieve 60% crosslinking [179]. Immediately, the solution was added to the device to completely cover the PVOH templates. The device was placed under a UV lamp and exposed to UV light at 365 nm wavelength for 20 seconds to allow polymerization. The device was transferred to a water bath at 45°C and incubated overnight for PVOH dissolution. Post dissolution, the internal channel network was perfused with a mixture of green food colorant and water to enhance imaging contrast.

5.6.3 Alginate

Alginate hydrogels were fabricated within a custom-made polypropylene and stainless steel (SS) device that suspended PVOH templates between inlet and outlet ports. To form the alginate hydrogels, a 5 mL solution of 2% sodium alginate in sterile, deionized water was prepared by overnight mixing at 4 °C. A CaSO₄-alginate slurry was prepared by adding 300 µL of 7.5% CaSO₄ in deionized water to the 5 mL of 2% sodium alginate solution. The slurry was poured into the device to cover the suspended PVOH template, and allowed to pre-gel for 10 min. Then the device was submerged in a 2% (w/v) solution of CaCl₂ in deionized water to finalize the hydrogel gelation and completely dissolve the PVOH template. Post dissolution, the internal channel network was perfused with Dexron-VI automatic transmission fluid to enhance imaging contrast.

5.6.4 Imaging and Reconstruction

Hydrogels were imaged using standard photography or a microCATII microCT (Siemens AG.) at the University of Wisconsin Carbone Cancer Center's small animal imaging facility. The Digital Imaging and Communications in Medicine (*DICOM*) image stacks were then reconstructed and converted into STL graphic bodies using Mimics software (Materialize NV.). Image analysis was performed using a combination of Magics (Materialize NV.), MeshLabs, and Solidworks (Dassault Systemes).

5.7 Results and Discussion

5.7.1 Injection molded, Sacrificial PVOH and PVOH-CaCl₂ Templates

To alleviate handling durability issues inherent to carbohydrate glass sacrificial templates, we opted to produce our templates from water-soluble, biocompatible PVOH similar to Tocchio et al. [168]. Micro-injection molding was chosen as the preferred fabrication technique to mitigate manufacturing mass-production scalability concerns with rapid prototyping based and SLA/solvent casting approaches. Aluminum molds were CNC-milled to produce sacrificial PVOH templates with a lattice geometry consisting of cylinders transitioning from 3 to 1 mm in diameter (Figure 5.1, Figure 5.2E, and Supplemental Figure 5.7). PVOH lattice templates were injection molded, encapsulated within polyacrylamide, PEG, and alginate hydrogels, and dissolved in a water bath to generate monoliths with replicate internal architecture. Post template dissolution, bulk curing polyacrylamide and PEG hydrogels displayed discernable and precisely casted internal channels (Figure 5.2A-B). The PEG hydrogel's channels displayed a higher deviation from

the PVOH template's dimensions presumably due to the hydrogel's characteristic swelling [179, 180] (**Figure 5.2H**). However, a series of disconnected and non-uniform voids were generated in alginate hydrogels, suggesting that the PVOH template dissolved prior to the inward diffusion of Ca²⁺ ions (**Figure 5.2C** and **E-F**).

To enable effective sacrificial molding of alginate hydrogels, we hypothesized that compounding calcium salts into the PVOH template would accelerate the crosslinking rate at the template/hydrogel interface and result in greater geometric control of the cast internal architecture. Accordingly, PVOH was compounded with 5% and 10% (w/w) CaCl₂ using twin screw extrusion, and the PVOH-CaCl₂ composite was injection molded into a lattice geometry (Figure 5.2E). Upon casting with PVOH-CaCl₂ templates, continuous channel networks were observed within alginate hydrogels indicating release of the compounded calcium ameliorated casting efficacy (Figure 5.2D-G). Metrological analysis of the sectioned hydrogels (Figure 5.2E-G) revealed that compounding 10% vs. 5% (w/w) CaCl₂ into the PVOH lattice yielded significantly better casting of channel network geometries (Figure 5.2H). However, the casted architecture still displayed a ~30% dimensional deviation from the PVOH-CaCl₂ template. Thus, the addition of CaCl₂ to PVOH template enables casting of architecture within both bulk curing and ionically crosslinked hydrogel monoliths, but casting precision within alginate hydrogels could still be improved.

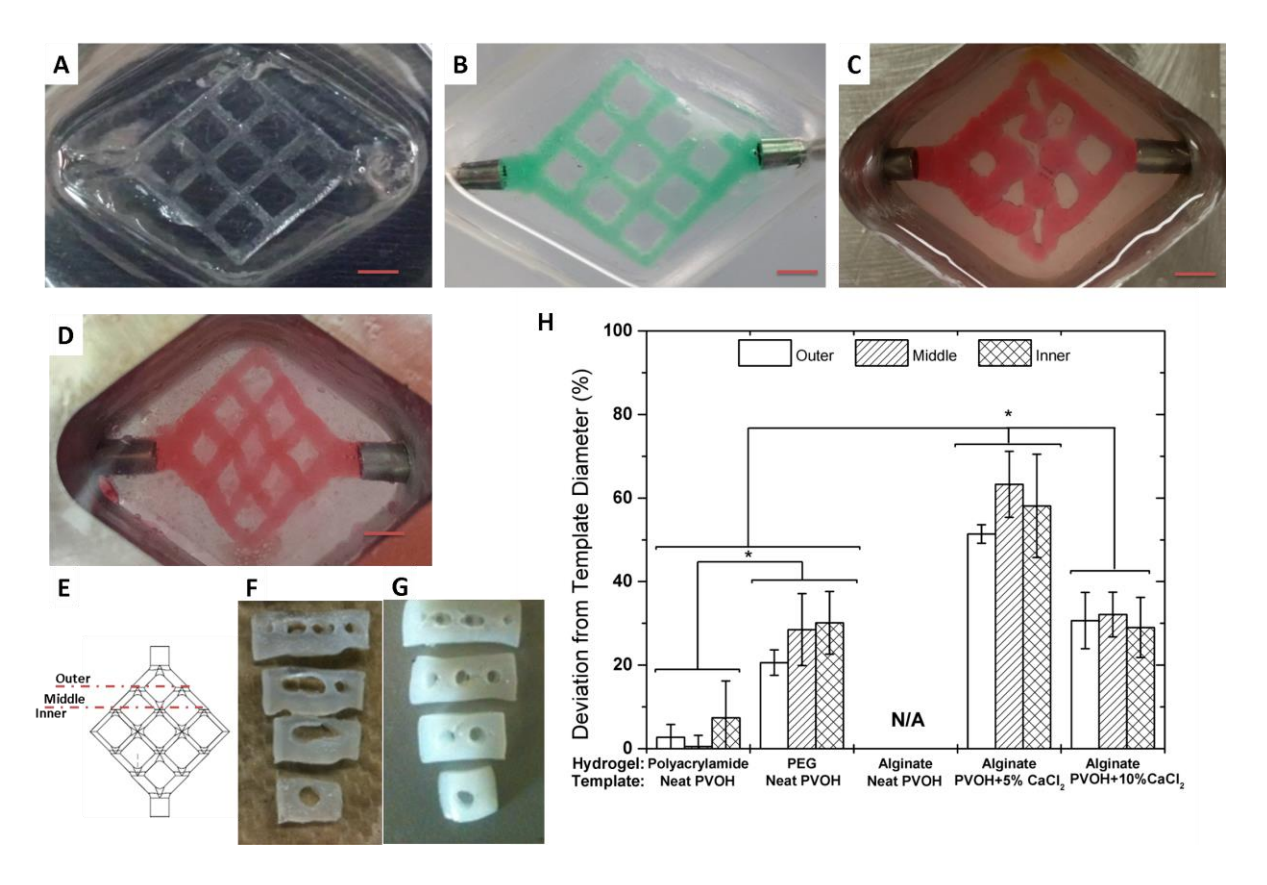


Figure 5.2 Representative images of channel-laden hydrogels casted using sacrificial PVOH and PVOH-CaCl2 templates. (A) PEG, (B) polyacrylamide, and (C) alginate hydrogels cast using PVOH templates. (D) Alginate hydrogel cast using a 10% (w/w) loaded PVOH-CaCl2 template. (E) Schematic of cross-sectional hydrogel slices made to measure outer, middle, and interior channel diameters. Representative images of cross-sectioned alginate hydrogels cast using (F) PVOH and (G) 10% loaded PVOH-CaCl2 templates. (H) Metrological analysis of the hydrogel channel diameter's deviation (%) from the sacrificial template's geometry. Data combined from duplicate experiments to yield n=8, 16 and 24 for outer, middle and inner channels, respectively. Error bars represent standard deviation; *P<0.05, Student's unpaired t-test; scale bar is 3 mm.

5.7.2 Optimizing Mechanical Properties of PVOH-Ca Templates

Although the PVOH-CaCl₂ casting results were promising, the addition of CaCl₂ into the PVOH substrate also yielded undesirable fabrication side effects. Notably, the composite was much more difficult to process via extrusion and injection molding than neat PVOH; thermal degradation of the polymer was apparent both visually and aromatically. According

to a prior cement study, dissolved Ca²⁺ ions can produce strong crosslinking-like interactions between adjacent hydroxyl groups on PVOH backbone chains [83]. Since CaCl₂ solubility is high and increases with temperature (Supplemental Table 5-2), we suspected that the thermal processing of extrusion and injection molding amplified Ca²⁺ crosslinking within the polymer composite. This would make microscale PVOH-CaCl₂ templates difficult to injection mold. Also, it would decrease the Ca²⁺ ions released upon template dissolution and thereby available for crosslinking alginate. Therefore, we hypothesized that compounding PVOH with Ca salts of lower solubility would minimize intra-composite crosslinking.

To test this theory, PVOH was also compounded with calcium iodide (CaI₂), calcium acetate (Ca(C₂H₃O₂)₂), or calcium carbonate (CaCO₃) salts, listed in order of decreasing solubility (Supplemental Table 5-2). Then, each composites' mechanical properties and calcium release were analyzed in detail (**Figure 5.3** and **Figure 5.4**). Tensile strength tests on injection molded PVOH-Ca ASTM D638 Type V specimens showed that the compounded calcium salts decrease composite ductility, i.e. strain at break [181], and increase modulus and ultimate tensile strength (UTS) compared to neat PVOH (**Figure 5.3A** and **B**). The Ca salts' effect on composite modulus and UTS is directly correlated with their solubility while the effect on composite ductility is inversely correlated. These results agree with traditional polymer filler theory taking into account polymer chain crosslinking by solvated Ca²⁺ ions. Notably, sacrificial templates produced from PVOH-Ca(C₂H₃O₂)₂ or CaCO₃ composites versus carbohydrate glass would have enhanced handling durability due to a 50-fold increase in ductility [110].

Rheological measurements were conducted to assess each PVOH-Ca composite's viscosity and thereby relative ease of manufacturing by extrusion and injection molding.

Using a parallel plate rheometer to measure viscosity at continuous shear rates, PVOH-CaI₂ or -CaCl₂ composites displayed a viscosity ~10 folds higher than PVOH-neat, -Ca(C₂H₃O₂)₂, or -CaCO₃ across an order of magnitude shear rate range (0.1-1 per sec) (**Figure 5.3C**). Similar to modulus and UTS data, the composite's viscosity was directly correlated to Ca salt solubility. The decreased viscosity of PVOH-neat, -Ca(C₂H₃O₂)₂, or -CaCO₃ composites was observed to facilitate extrusion and injection molding processes as well as minimized noticeable polymer degradation compared to PVOH-CaI₂ or -CaCl₂. As discussed later, optimizing the PVOH-Ca composite's viscosity was critical for feasible injection molding of sacrificial templates with microscale dimensions, i.e. micro-injection molding.

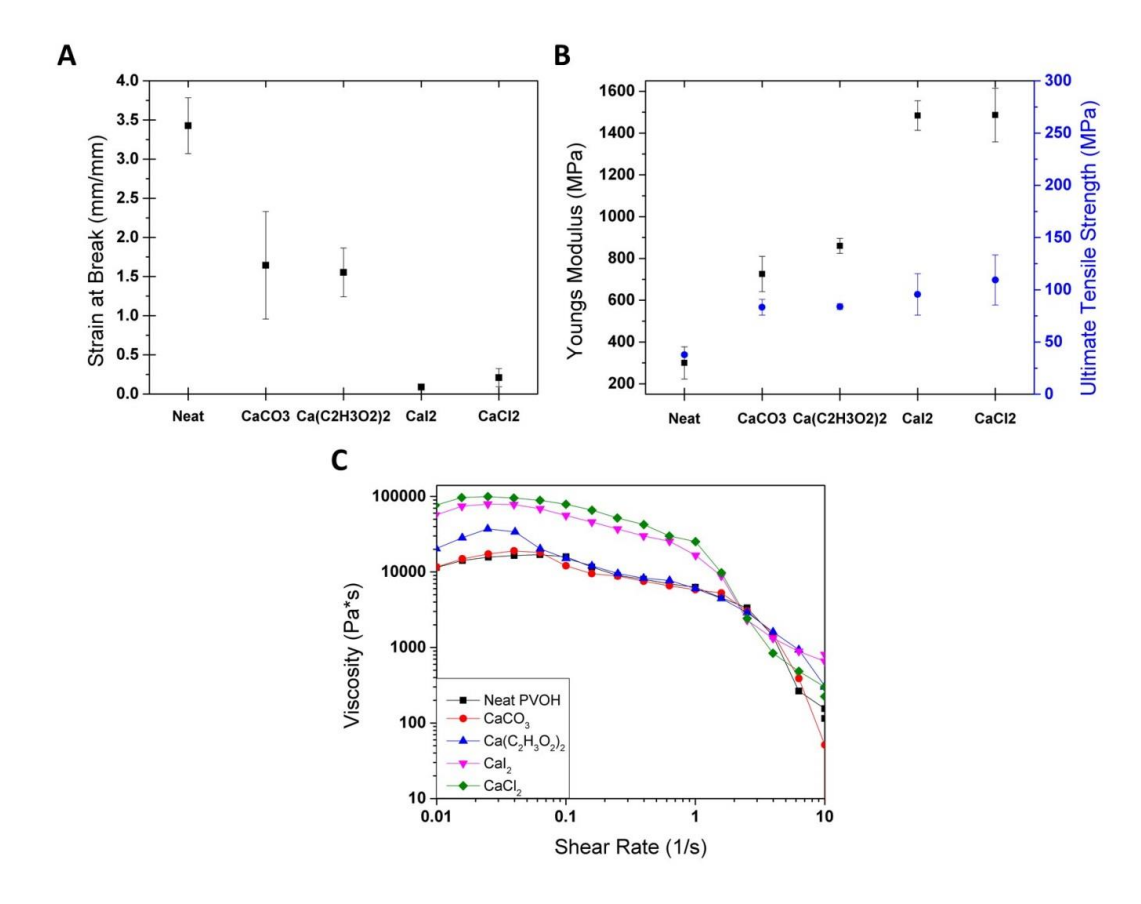


Figure 5.3 Mechanical property analysis at 25 °C. Tensile test of injection molded PVOH and PVOH-Ca specimens' (A) ductility, (B) Young's modulus and ultimate tensile strength

(UTS) results, n=10 experimental replicates and error bars represent standard deviation. (C) Rheological analysis of each specimens' viscosity over a range of shear rates.

5.7.3 Optimizing Calcium Release Properties of PVOH-Ca Templates

The lower solubility of calcium acetate and carbonate salts made them ideal compounding agents for producing PVOH-Ca composites with optimal mechanical properties. However, it remained unknown how their decreased solubility would affect Ca²⁺ ion release upon composite dissolution. To calculate this quantity, we first needed to know the actual weight percent of calcium salt in each PVOH composite. Since PVOH but not the compounded calcium salts decomposes below 600°C, thermogravimetric analysis (TGA), which measures mass loss over increasing temperatures, was executed on PVOH compounded with ~10% (w/w) calcium salts. As shown in **Figure 5.4A**, the compounded salts persisted in the ash content at 600 °C. When normalized to the remaining neat PVOH ash, the persistent salt masses were found to be consistent with compounded values except for the PVOH-CaI₂ composite. Considerable PVOH degradation was observed during PVOH-CaI₂ extrusion, thus skewing the TGA data where the degraded PVOH did not burn off under 600 °C. Also, the onset of degradation (first curve inflection point) of all PVOH-Ca composites occurred at lower temperatures than the neat composite, potentially indicating disruption of PVOH crystallinity by Ca²⁺ ions. This further corroborates the presence of intra-composite PVOH polymer/ Ca²⁺ crosslinking.

A complexometric calcium titration was performed on the PVOH-Ca composites to assess the amount of Ca^{2+} ions released upon dissolution in deionized water (**Figure 5.4B**). Calculating from the titration and TGA data, the average percent of released Ca^{2+} content

was determined to never be greater than 50%. Also, the Ca²⁺ released from PVOH-Ca(C₂H₃O₂)₂ or -CaCl₂ composites was equivalent and significantly higher than that released from PVOH-CaI₂ and -CaCO₃. The lower Ca²⁺ content release of PVOH-CaI₂ composites could be due to polymer degradation during extrusion and the skewed TGA data whereas that of the PVOH-CaCO₃ is likely due to the salt's low solubility in water (Supplemental Table 5-2).

As a final analysis to explain <50% calcium recovery from PVOH-Ca(C₂H₃O₂)₂ or -CaCl₂ composites, we performed differential scanning calorimetry (DSC). This analytical technique measures the thermal energy input required to induce a 1 °C temperature change in the sample, thereby allowing characterization of the composite's glass transition (T_g), melting (T_m) temperatures, and crystallization enthalpy (ΔH_c). In DSC second heating curves (Figure 5.4C), the T_g is indicated by the curve's first inflection point, and the T_m is indicated by the curve's last inflection point. We observed a direct correlation between the composites' T_g and an inverse correlation between the composites' T_m relative to its calcium salt's solubility (Supplemental Table 5-2), respectively. In the DSC cooling curve (**Figure 5.4D**), the ΔH_c is calculated as the area under the curves' exothermic peak. In analyzing this material property, we observed an inverse correlation between the composites' ΔH_c and the compounded calcium salt's solubility. Moreover, the presence of a double exothermic peak in the neat PVOH and extruded neat PVOH samples versus the single peak in the extruded PVOH-Ca samples indicates that imperfect types of crystals are being formed in salt containing samples. Collectively, the DSC results strongly suggested that the total compounded calcium content is not released from the PVOH-Ca composites upon dissolution due to intra-composite PVOH polymer/Ca²⁺ crosslinking. Importantly, our detailed analysis

of each composites mechanical and calcium release properties clearly imply that PVOH-Ca(C₂H₃O₂)₂ templates would provide superior sacrificial molding capabilities, handling durability, and micro-injection molding feasibility.

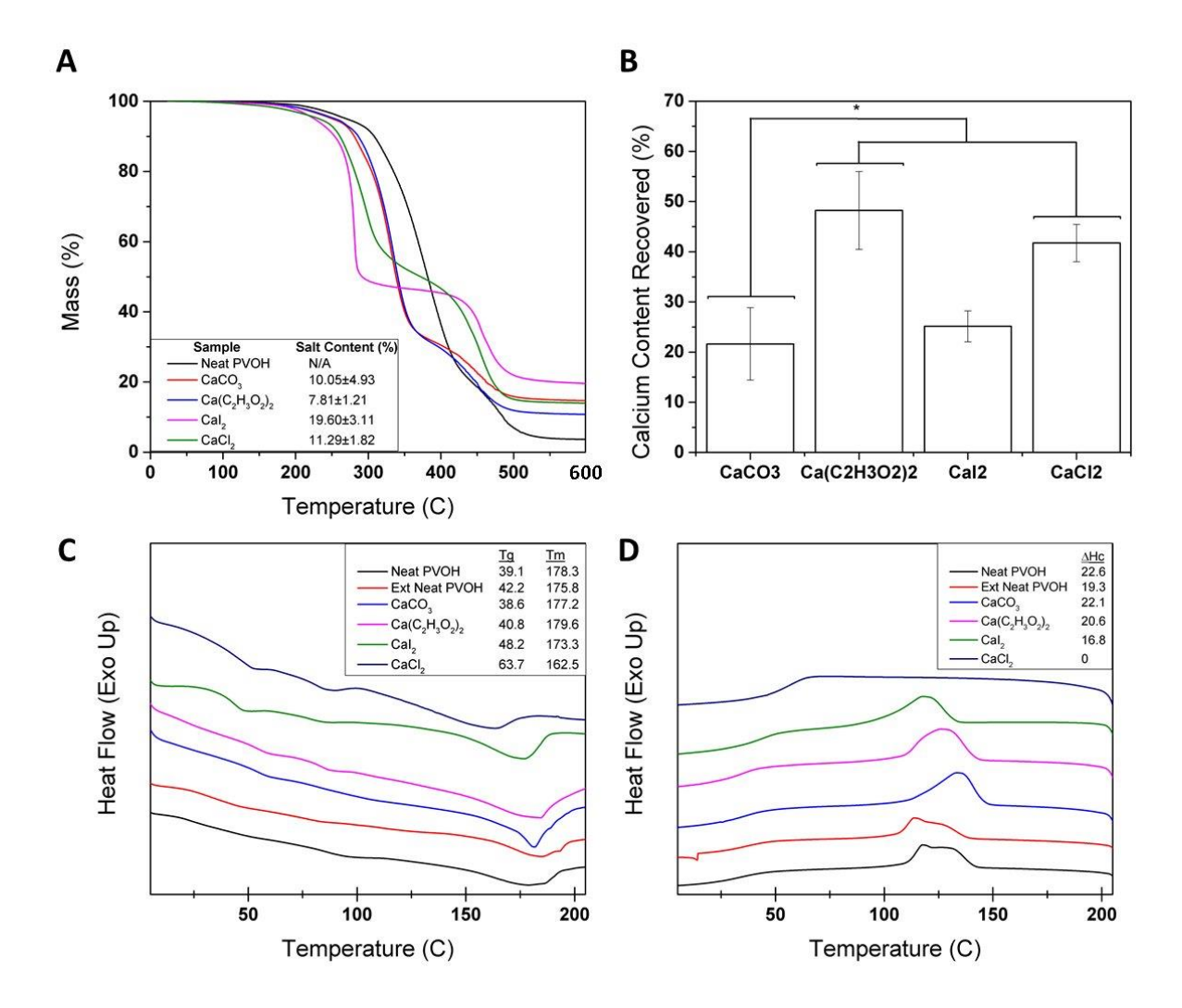


Figure 5.4 Material properties and calcium release analysis. (A) Representative thermogravimetric scans, n=3 experimental replicates. (B) Complexometric calcium titration, n=5 experimental replicates, *P<0.05, Student's unpaired t-test. Differential scanning calorimeter's (C) second heating and (D) first cooling curve traces of neat and extruded (Ext) PVOH and PVOH-Ca composites

5.7.4 Micro-injection Molded PVOH-Ca $(C_2H_3O_2)_2$ Templates

A micro-injection mold was CNC-milled for a fiber template geometry 2.2 cm in length that immediately tapered from a 3mm inlet/outlet diameter to a main fiber diameter of 500 μ m (**Figure 5.5A** and **Supplemental Figure 5.8**). PVOH-Ca(C₂H₃O₂)₂ templates of 10% salt loading were successfully micro-injection molded, but fabrication of similarly dimensioned and salt loaded PVOH-Ca(C₁ templates failed. Post sacrificial molding of alginate hydrogels using the PVOH-Ca(C₂H₃O₂)₂ templates, the resulting micro-channels were filled with pigmented oil for photographing, and they were quantitatively analyzed by micro-CT imaging and reconstruction analysis (**Figure 5.5A**). Dimensional analysis of the CT reconstructions revealed that the casted micro-channel diameter deviated from the template geometry by an average of $6.4 \pm 7.2\%$ average error at any point along its long axis, i.e. 10 measurements per casted micro-channel (**Figure 5.5B**). This demonstrates repeatable and precise casting of microscale architecture within diffusion limited, ionically crosslinked alginate hydrogels. Additionally, similarly dimensioned neat PVOH templates left no discernable micro-channel within alginate monoliths (data not shown).

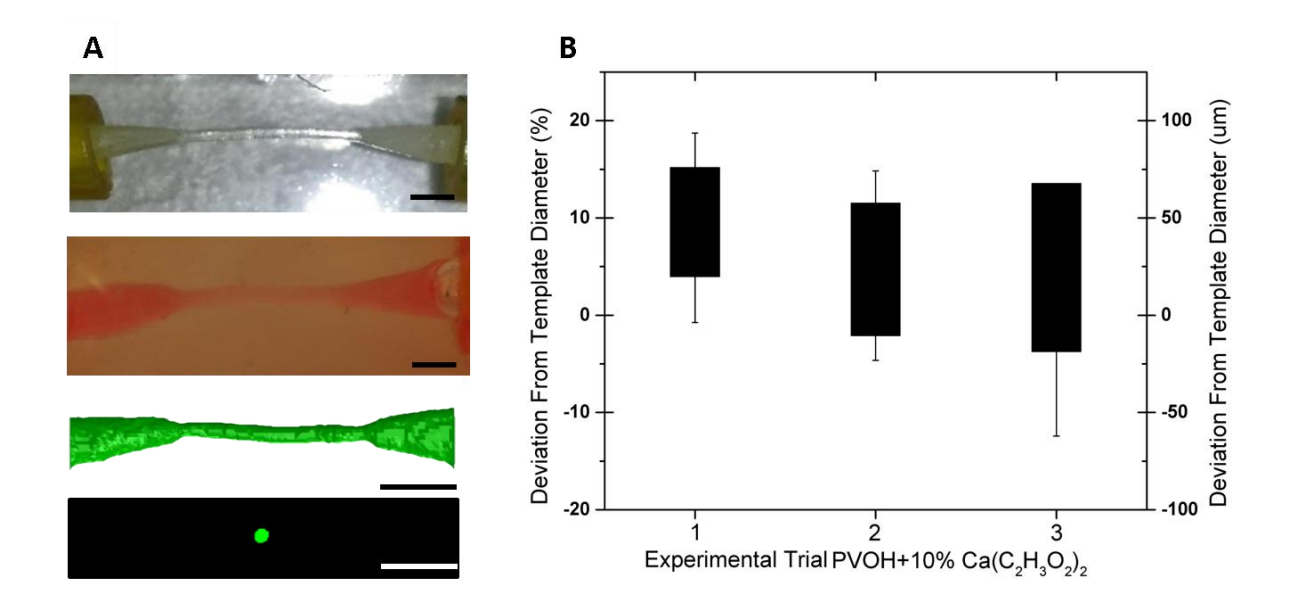


Figure 5.5 Representative images of (A) 10% Ca(C₂H₃O₂)₂ loaded PVOH sacrificial fiber templates as micro-injection molded (top) and dissolved within alginate hydrogels (middle). (B) Dimensional analysis was performed on CT scan reconstructions (A, bottom) of three separately cast alginate hydrogels at 10 points along each micro-channel. Error bar represents standard deviation. Scale bar is 3 mm.

5.7.5 Scalable 3-D Molding of Hydrogel Architecture

To explore the 3D scalability and versatility of injection molded PVOH-Ca(C₂H₃O₂)₂ templates, a set of CNC-milled, aluminum molds were fabricated to facilitate assembly of a 3D sacrificial template. The design allowed for freeform configuration of two modular components, a manifold and the previous lattice geometry, which connect via interference fit (**Figure 5.6A**). After injection molding, 3D PVOH-Ca(C₂H₃O₂)₂ templates were assembled like Legos[®] (**Figure 5.6B**), and used to sacrificially mold internal channel networks within polyacrylamide (**Supplemental Figure 5.9**) and alginate hydrogels (**Figure 5.6C**). After template dissolution, the hydrogels were CT scanned and image reconstruction verified the resulting 3D channel networks patency and continuity (**Figure 5.6D**). Thus, the design and injection molding of modular, PVOH-Ca(C₂H₃O₂)₂ components that can be assembled into

3D sacrificial templates represents a scalable and potentially limitless approach to precisely customize the architecture of bulk curing and ionically crosslinked hydrogels.

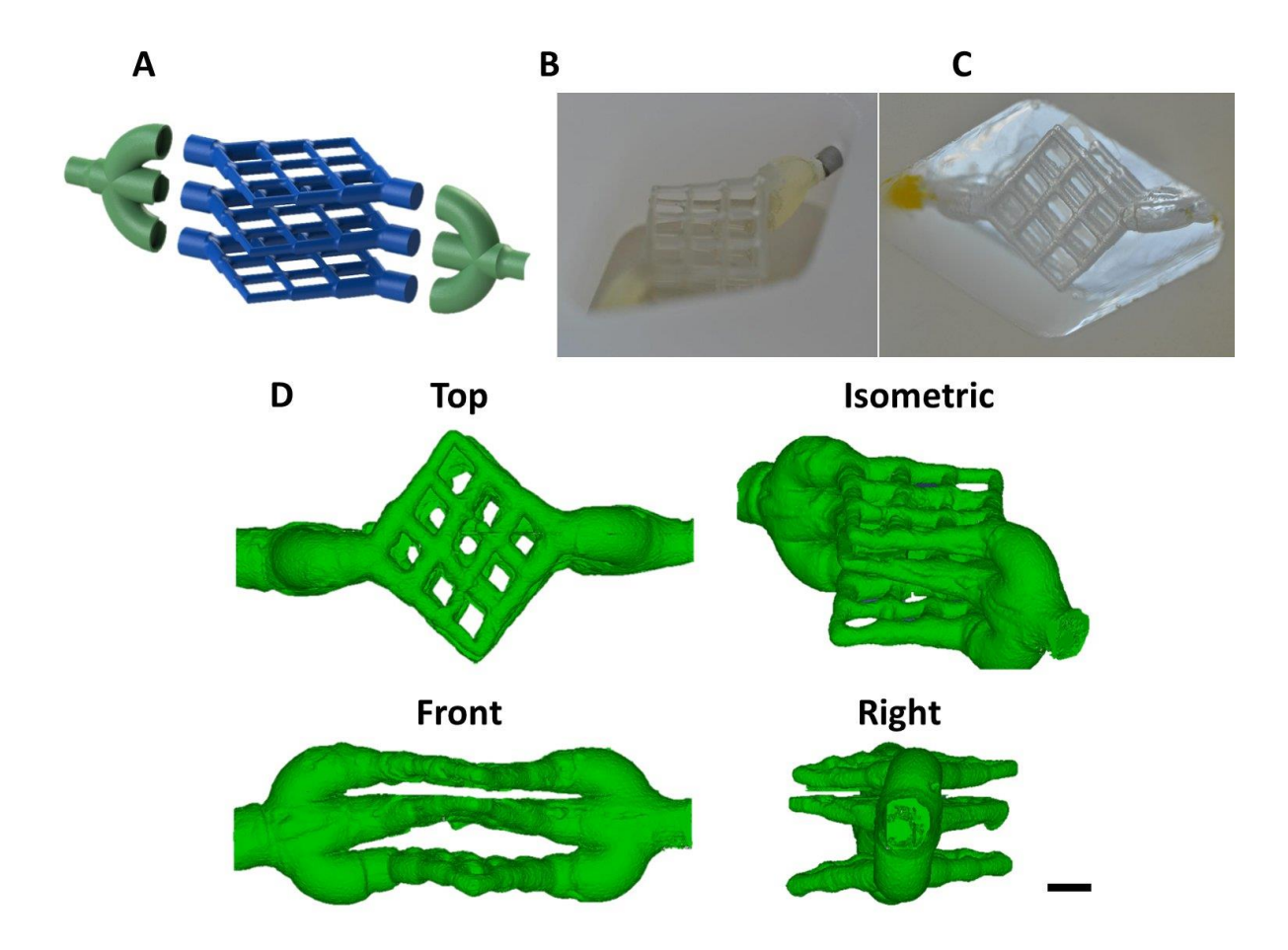


Figure 5.6 Modular 3D sacrificial molding using PVOH- $Ca(C_2H_3O_2)_2$ templates. (A) Exploded CAD model of modular, 3-D template design. (B) As molded and assembled 3-D template, and (C) sacrificially molded channel network within an alginate hydrogel. (D) CT scanned reconstruction of the channel network within an alginate monolith. Scale bar is 3 mm.

5.8 Conclusion

The ability to engineer tissue constructs with biomimetic morphologies and cytoarchitectures has been greatly enhanced by the development of techniques to fabricate biomaterial scaffolds with macro-to-microscale features. Sacrificial molding is a promising

and scalable technique for rapidly casting complex architectures within hydrogel scaffolds. Yet, prior studies primarily demonstrated its efficacy using bulk curing hydrogels while noticeably less molding feasibility and precision were observed when applied to diffusion limited, ionically crosslinked hydrogels such as alginate. Furthermore, these studies performed limited to no quantitative analysis of their sacrificial molding approach's feature casting fidelity.

Here, we fabricated injection molded, PVOH-Ca templates to facilitate and optimize sacrificial molding within both bulk curing and ionically crosslinked hydrogels. Injection molded PVOH templates effectively mold bulk curing hydrogels such as polyacrylamide and PEG. However, the addition of calcium salts to the sacrificial templates was both necessary and sufficient to enable precise casting of microscale features within alginate monoliths. Extensive characterization unveiled that the PVOH-Ca composite's mechanical, material, and calcium release properties could be tuned based on the compounded calcium salt's solubility. Also, this analysis proved that PVOH-Ca(C₂H₃O₂)₂ possessed superior manufacturability and sacrificial template material properties, which were further demonstrated by precise casting of microscale 2D and modular 3D alginate hydrogel architectures. The micro-injection molded, PVOH-Ca(C₂H₃O₂)₂ templates described herein were developed to maximize production scalability and template design flexibility, as well as ease of implementation for researchers. We envision manufacturing these templates as a library of modular geometric pieces that can be assembled in Lego®-like configurations for rapid and precise customization of hydrogel scaffold architecture for diverse tissue engineering applications.

5.9 Supplemental Information

Table 5-2 Quantification of water solubility of various calcium compounds adapted from IUPAC-NIST solubility database [82].

IUPAC-NIST Solubility Table (g/100cc water)										
	Formula	Temperature (°C)								
Compound		0	10	20	30	40				
Calcium Carbonate	CaCO ₃	0	0	0	0	0				
Calcium Sulfate	CaSO ₄	0.2	0.2	0.3	0.3	0.3				
Calcium Acetate	Ca(C ₂ H ₃ O ₂) ₂	37.4	36	34.7	33.8	33.2				
Calcium Iodide	CaI ₂	64.6	65.3	66	67.6	70.8				
Calcium Chloride	CaCl ₂	59.5	64.7	74.5	100	128				

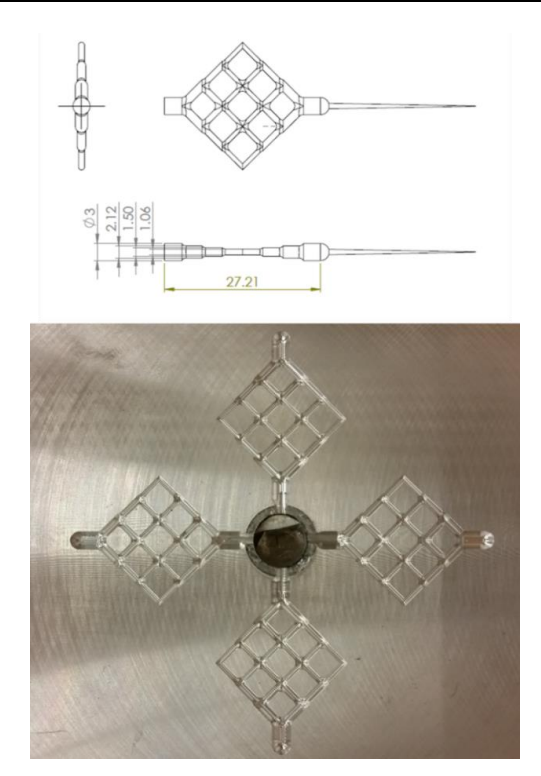


Figure 5.7 CAD drawing of the 2D, sacrificial PVOH lattice templates with associated CNC-milled aluminum mold. All dimensions in mm.

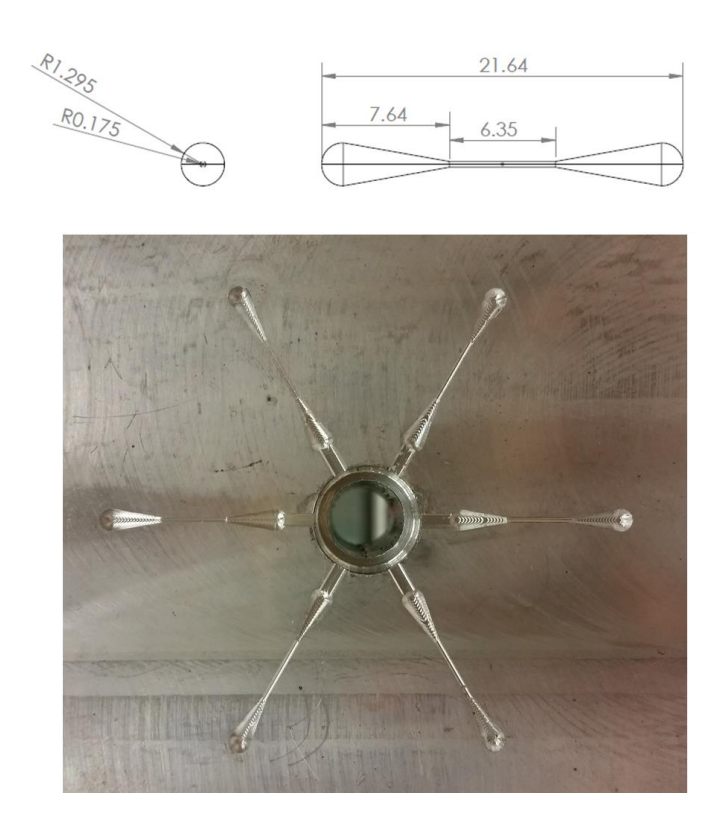


Figure 5.8 CAD drawing of the 2D, sacrificial filament templates with associated CNC-milled aluminum mold. All dimensions in mm.

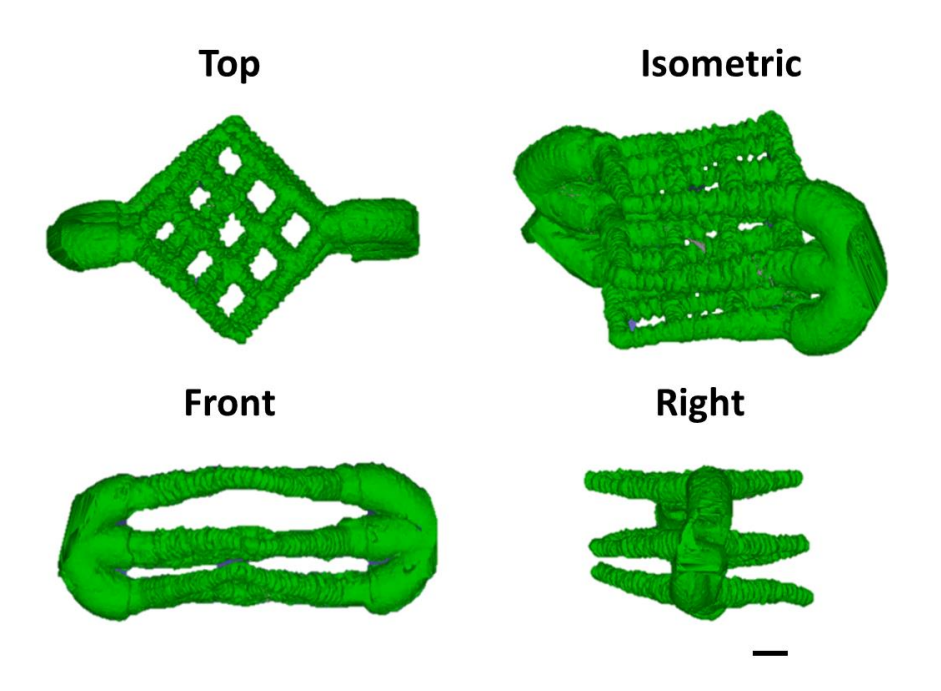


Figure 5.9 CT scanned reconstruction of a 3D channel network within a polyacrylamide monolith.

6 Sacrificial PVOH Cytocompatibility and Testing of Perfusion Bioreactor Culture System

In order to use the sacrificial molding technique described in the previous chapter for tissue engineering applications, it first needs to be fully vetted for cytocompatibility. To maximize efficiency, ensure proper nutrient delivery throughout the hydrogel scaffold, and maintain proper cell culture conditions, a custom-designed perfusion bioreactor was fabricated and exhaustively tested.

6.1.1 Bioreactor Design for Neural and Vascular Tissue Culture

In order to enable long term cell culture (upwards of 1 month) within feature laden hydrogels but outside of a standard cell culture incubator, a microscope-stage-mounted perfusion bioreactor system was designed which allowed for real-time monitoring of cellular growth and development. A multi-head peristaltic pump controlled media flow both before and after the temperature controlled stainless steel (SS) bioreactor device to ensure consistent flow through the hydrogel's channel network. PH was maintained in the cell culture media by a volumetric gas mixing system, which pumped a defined air and CO₂ mixture through a humidifier (**Figure 6.1**).

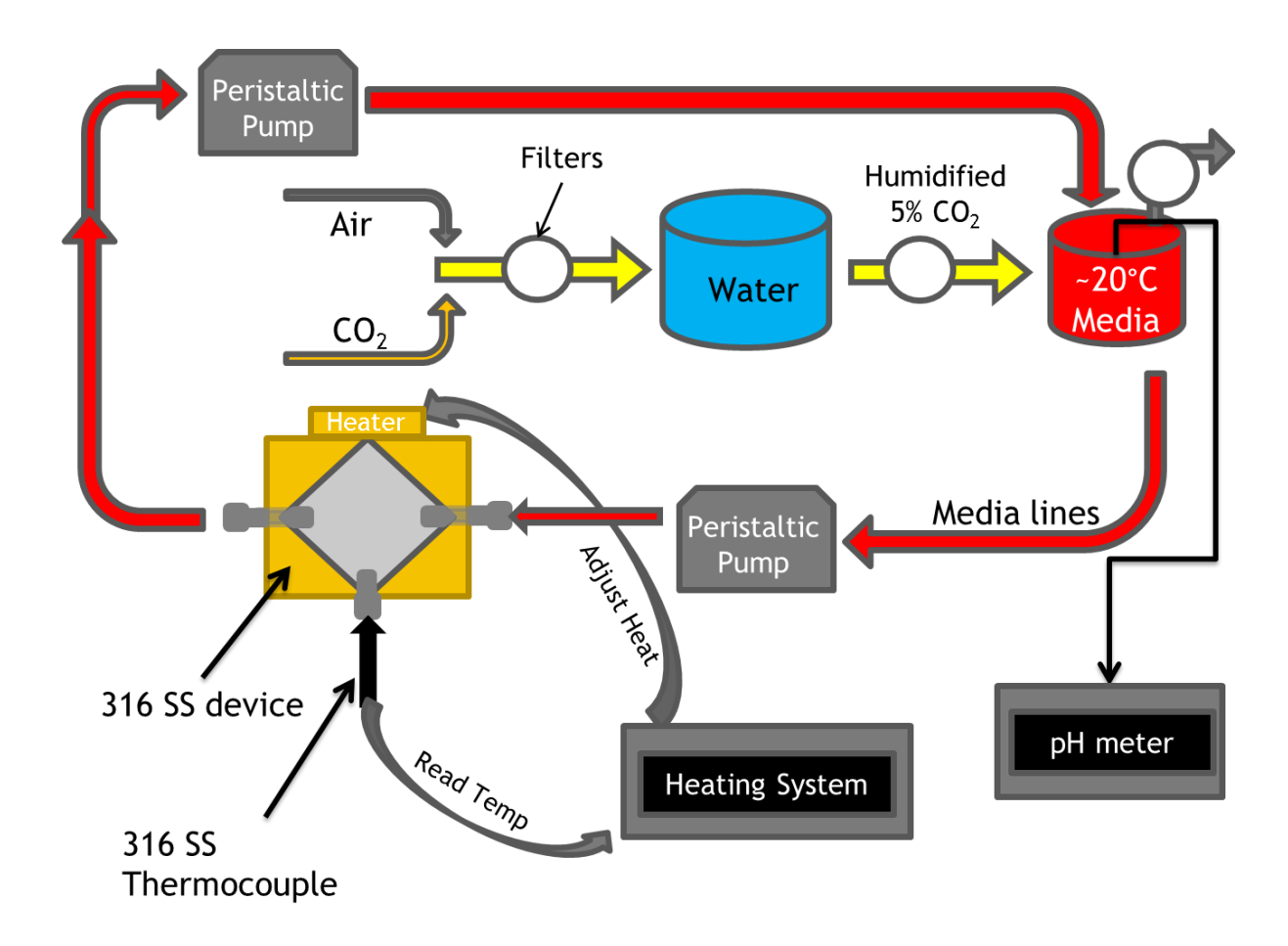


Figure 6.1 Schematic of custom bioreactor system, identifying flow directions and equipment configurations.

Long-term temperature stability of the perfusion bioreactor system was recorded for various volumetric flowrate configurations from 0-2 mL/min. Data for one 0.3 mL/min flowrate can be seen in **Figure 6.2**, where a proportional controller was needed to maintain a consistent temperature (P=4.5). Less than half a degree C overshoot was recorded and the temperature was maintained for upwards of 12 hours with fluctuations equivalent to commercially available cell culture incubators.

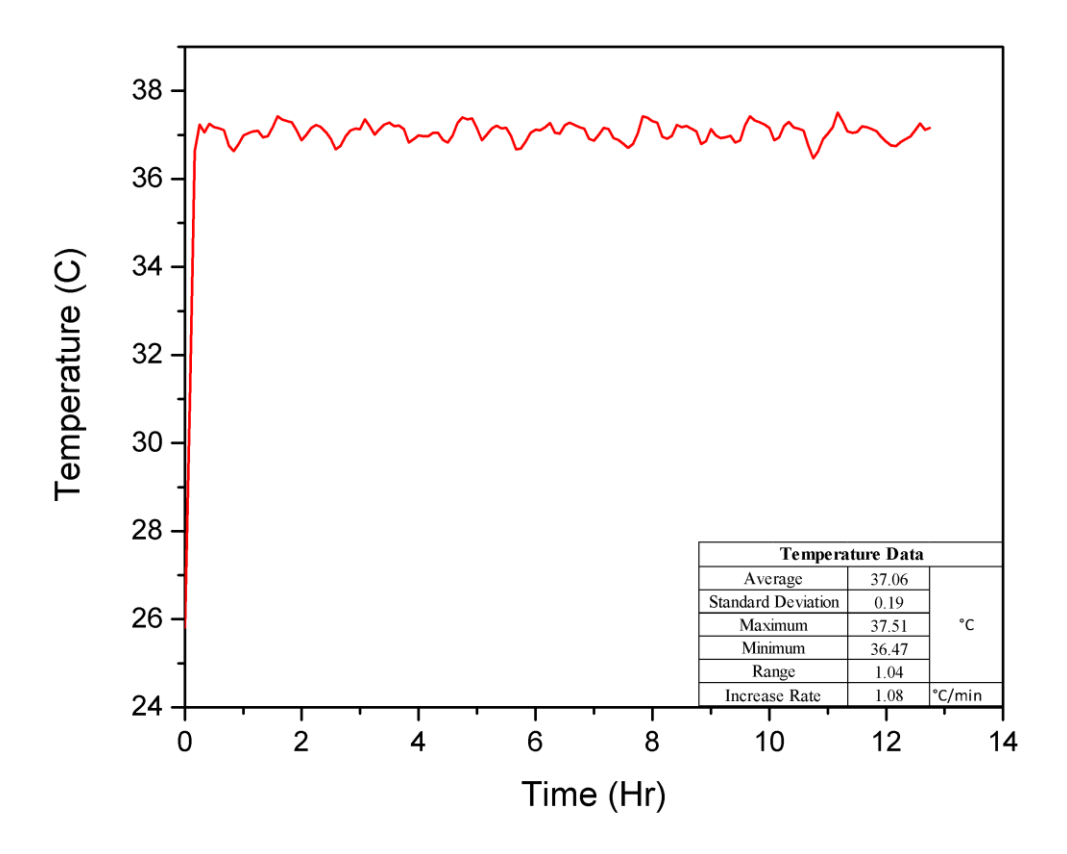


Figure 6.2 Bioreactor temperature control profile with proportional control (P=4.5) and media flow at 0.3 mL/min.

6.1.2 Biocompatibility Testing

Biocompatibility testing was performed on all materials that would contact the cells or culture medium. Cell proliferation assays were executed using 303 and 316 SS bioreactors and solutions containing varying amounts of dissolved PVOH to ensure cell survival within alginate hydrogels molded with interior channels. All thermally stable materials were autoclaved prior to use, bioreactors fabricated both 303 and 316 SS were sealed with silicone O-rings between rigid and transparent bases and lids. 316 SS dispensing needles were

installed into the bioreactors as inlet and outlet ports, capped and secured with 316 SS set screws. The devices were rinsed with phosphate-buffered saline (PBS) and with Dulbecco's modified eagle medium nutrient mixture F-12 (DMEM/F12) followed by a coating of Matrigel in DMEM/F12 overnight. Cells cultured in a tissue culture polystyrene (TCPS) 6 well plate coated in a similar fashion were used as a positive control.

H9 GFP hESCs were seeded in both the bioreactor and a control 6 well plate at 150 k cells/cm², and differentiated into neural epithelial cells (NECs) using the E6 method [158]. Images were taken daily using 4x and 10x objectives on a Nikon epifluorescence microscope. **Figure 6.3** through **Figure 6.5** identify NECs which within the SS bioreactors. It can be seen that the cells on the TCPS control and within the 316SS sustained cell survival for upwards of 4 days, while the cells seeded within the 303SS system were killed within 5 days of culture.

NECs on TCPS Control

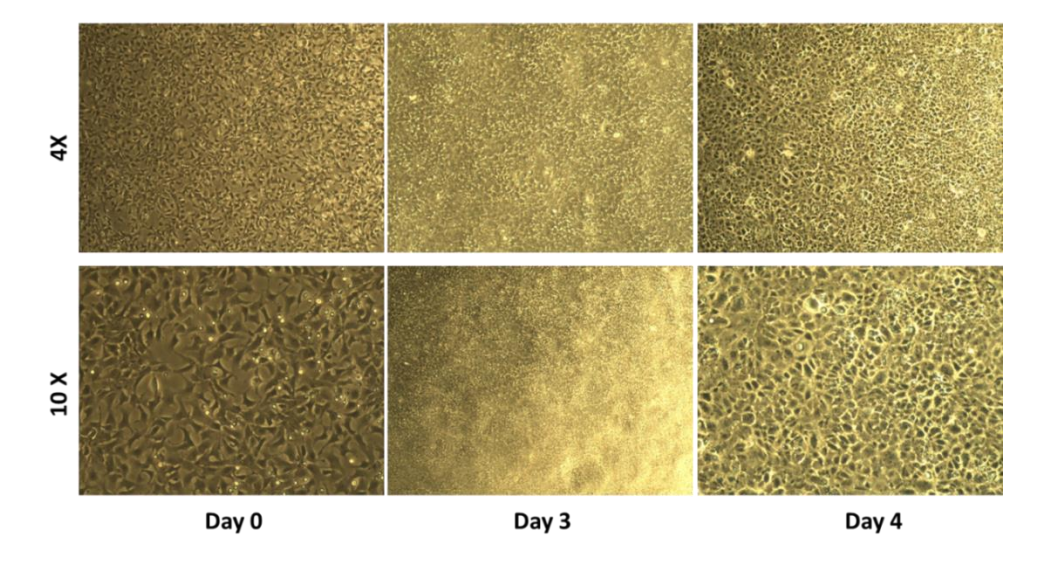


Figure 6.3 NECs seeded within a Matrigel coated, standard TCPS 6 well culture plate.

NECs on 303SS w/Acrylic Day 5

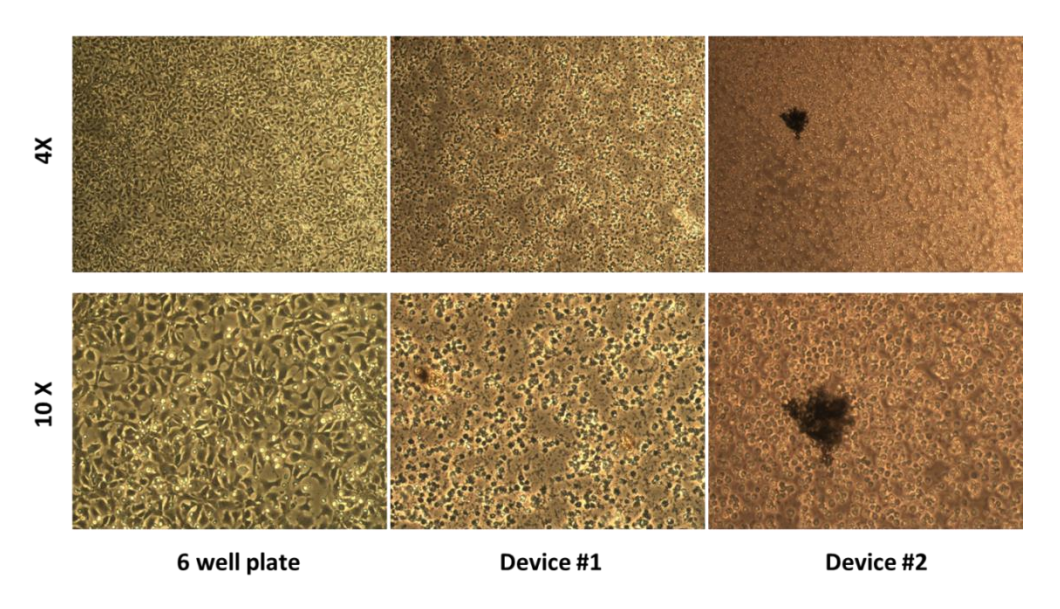


Figure 6.4 NECs seeded within a 303SS bioreactor on a Matrigel coated acrylic base.

NECs on 316SS w/Acrylic

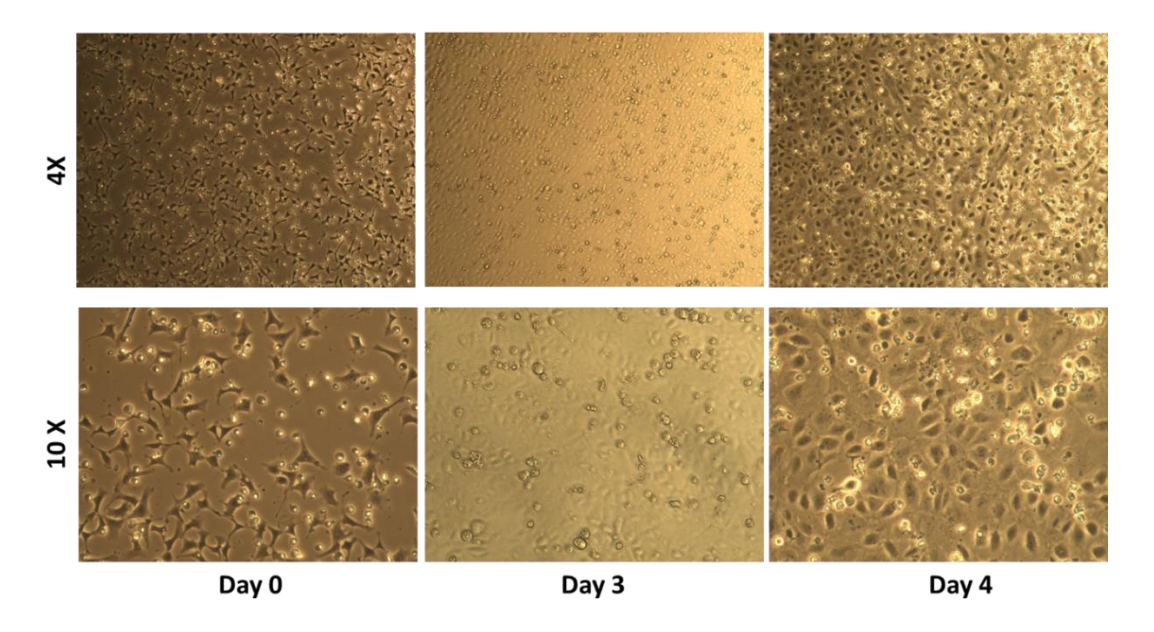


Figure 6.5 NECs seeded within a 316SS bioreactor on a Matrigel coated acrylic base.

It was noted that while the 316SS bioreactor was able to support NEC survival, continuous flow was not performed because it caused dramatic cell death. Additionally, the terminal cell density was significantly lower than that of the standard TCPS well plate, therefore, subsequent experimentation within 316SS bioreactors utilized TCPS base materials to increase the systems viability.

Next, to ensure that the cells differentiate properly in the bioreactor, undifferentiated H9s were seeded onto a Matrigel coated TCPS well plate and TCPS base plate within a 316SS bioreactor. One bioreactor was maintained within a standard cell culture incubator and the other was maintained using the external control system described previously (**Figure 6.1**). **Figure 6.6** through **Figure 6.8** show representative images of the results for each configuration. It should be noted that in each case the H9's differentiate into characteristic rosette structures, indicating that the external bioreactor system maintains a microenvironment similar to a cell culture incubator [158].

H9 differentiation on TCPS Control

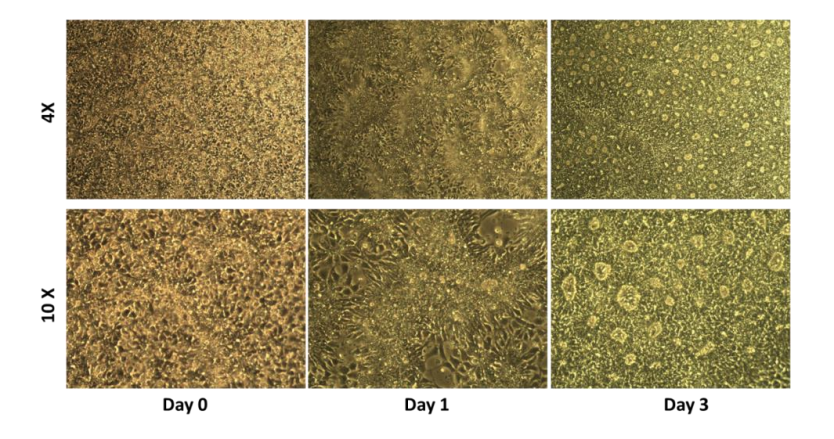


Figure 6.6 H9s seeded within a Matrigel coated standard TCPS culture plate subjected to a neural differentiation protocol. Rosette formation begins in day 1 and can be seen significantly in day 3.

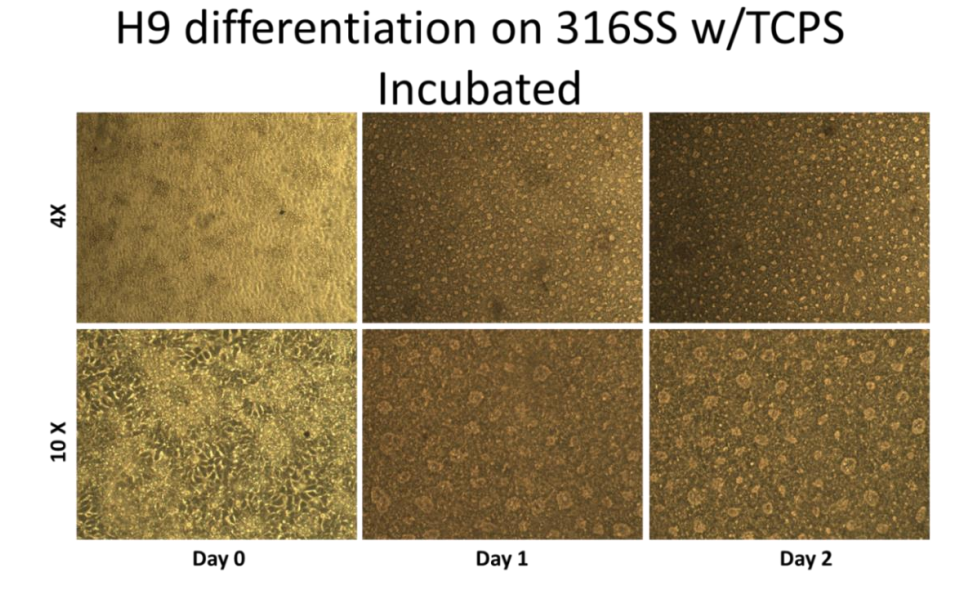


Figure 6.7 H9s seeded within a 316SS bioreactor on a Matrigel coated TCPS base subjected to a differentiation protocol while temperature and PH were controlled inside a standard cell culture incubator. Rosette formation begins in day 1 and can be seen significantly in day 2.

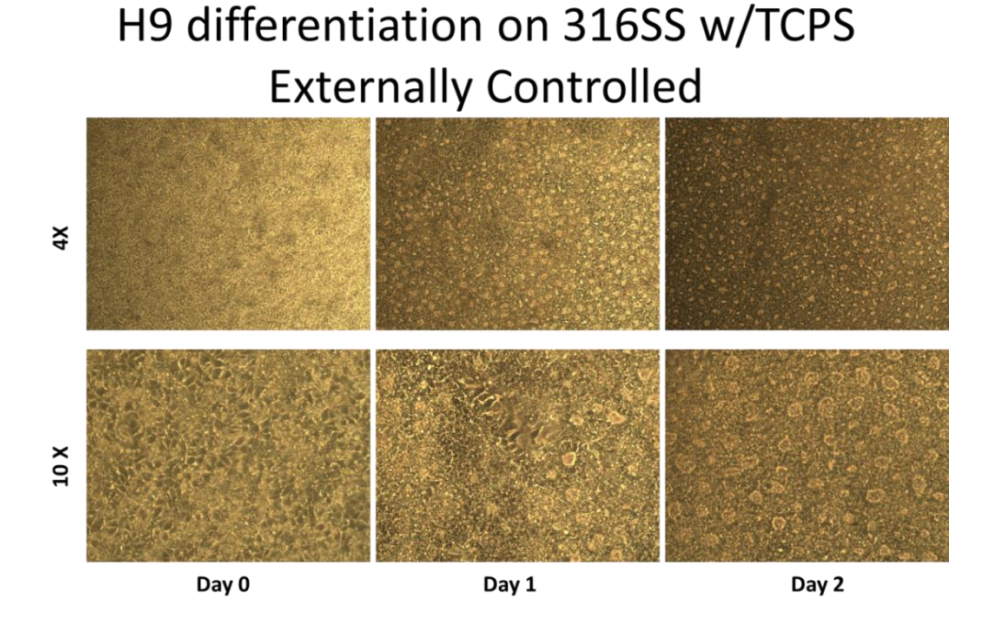


Figure 6.8 H9s seeded within a 316SS bioreactor on a Matrigel coated TCPS base subjected to a differentiation protocol while temperature and PH was externally controlled. Rosette formation begins in day 1 and can be seen significantly in day 2.

To verify the sacrificial PVOH templates used in this technique were biocompatible and would not detract from cellular functions, passage 7 HUVECs were cultured in media containing varying concentrations of dissolved Monopol C100 . Specifically, PVOH was dissolved into PBS to a concentration of 100 mg/mL. The solution was then serially diluted into 6 concentrations from 0-10 mg/mL and combined with standard HUVEC media. HUVECs were seeded into 28 wells of standard TCPS 96 well plates with 4 replicates per experimental PVOH-media solution. Representative images have been shown below in **Figure 6.9** and the proliferation assay (Cyquant) data has been displayed in **Figure 6.10**.

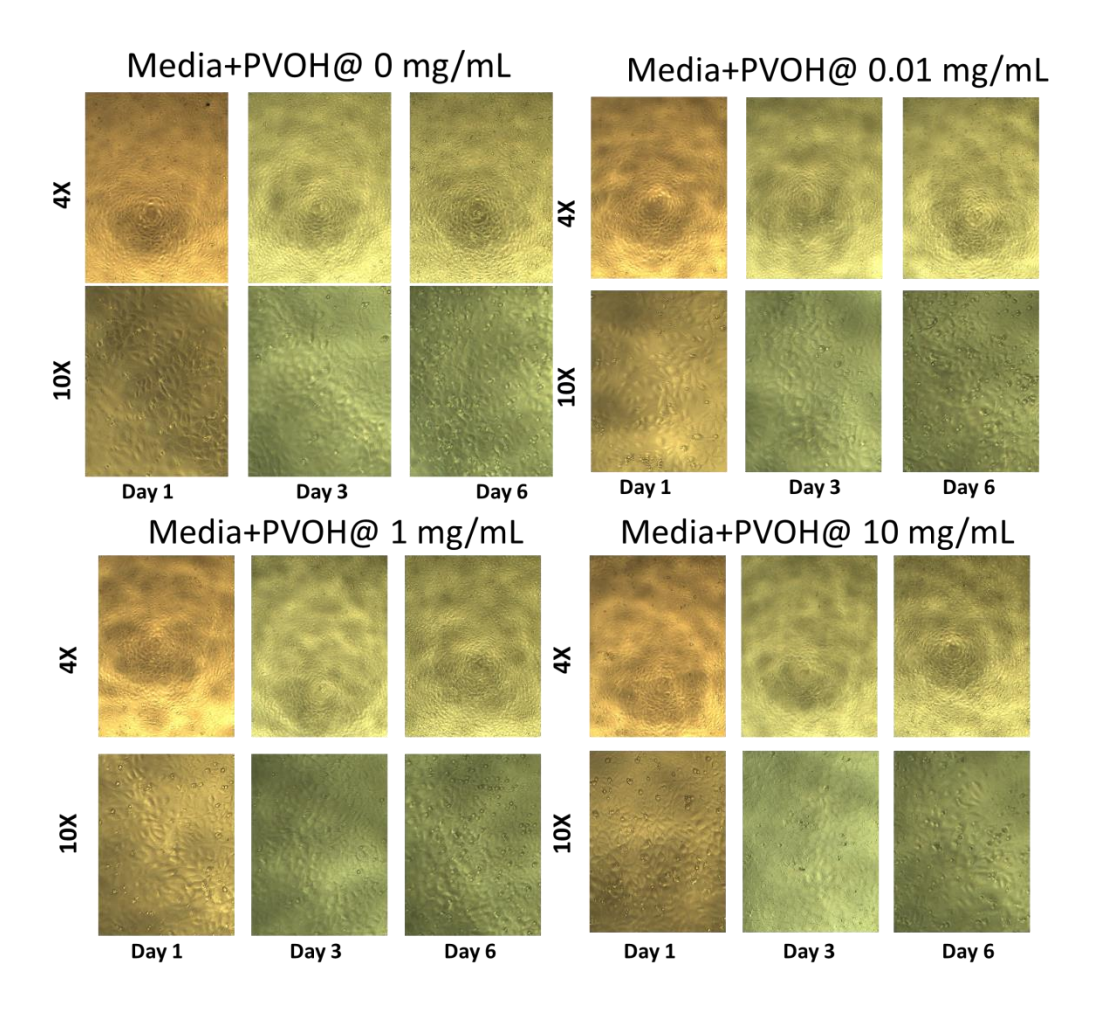


Figure 6.9 Representative images of the HUVECs cultured with varying amounts of PVOH within the cell culture media. 0.001 and 0.1 mg/mL concentrations not shown.

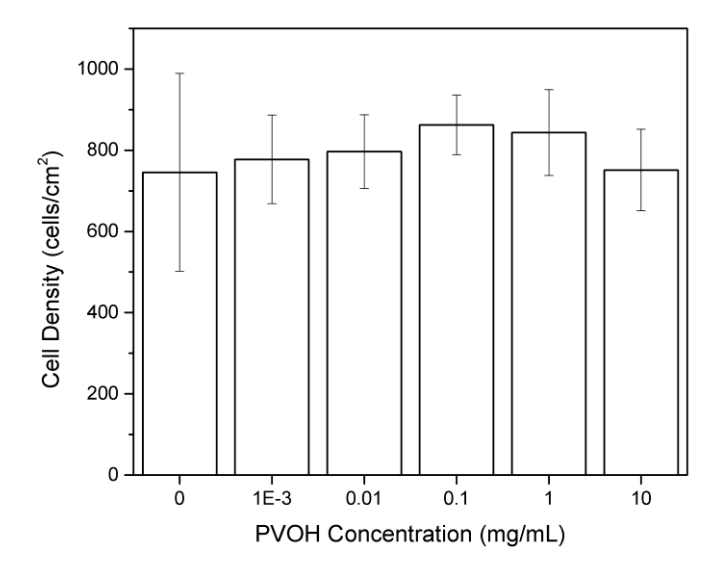


Figure 6.10 Results at day 6 from the Cyquant assay performed on the HUVECs exposed to varying concentrations of dissolved PVOH.

The PVOH containing cell culture media had no discernable effect on the viability of HUVECs in respect to their attachment and proliferation over 6 days. Therefore, the next logical step was to assess the performance of the entire perfusion bioreactor system with all the subcomponents in place.

6.1.3 Alginate Functionalization

While alginate is naturally non-cytophobic, it is also highly hydrophilic and non-fouling biomaterial; therefore, it is inherently cell adhesion resistant without supplemental chemical modification. While these traits allow for alginate to be used in biological therapeutics without adverse and toxic effects, the lack of adhesion prevents the material from nearly all tissue scaffolding applications. In the literature numerous methods have been published for rendering alginate protein cell adhesive [69, 182]. One of the most common techniques is to conjugate peptides containing synthetic RGD (CGYGPGRGDSPK) peptides.

To determine what level of RGD conjugation, a solution of RGD peptide and alginate was mixed at various molar mass ratios from 100:1 to 6.66:1 (1% to 15% RGD). The solutions were analyzed with a fluorescent plate reader to formulate a standard curve for the RGD based on UV absorption of the aromatic tyrosine at 280 nm (**Figure 6.11**). Next, conjugated RGD-alginate hydrogels (2% and 10%) subjected to extensive dialysis to remove unconjugated peptide, analyzed using UV absorption and were compared to the standard curve.

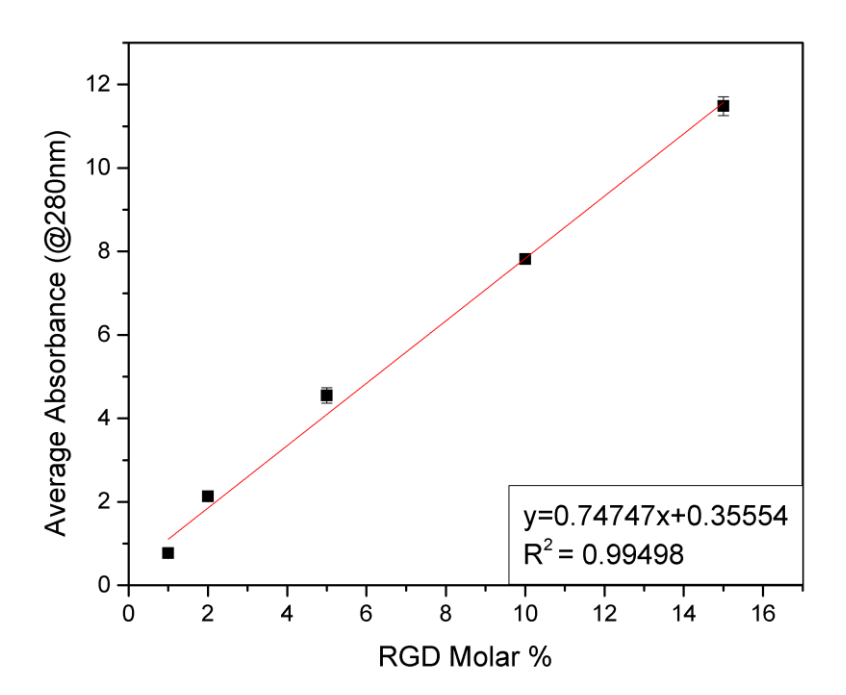


Figure 6.11 Standard curve of RGD mixed with alginate at various concentrations.

The results confirmed that the actual molar mass % yield was 0.817% and 6.213% respectively verifying that RGD was indeed bound to the alginate hydrogel. Next, to test whether or not the RGD conjugated alginate hydrogels could support cell survival, HUVECs (passage 5) were seeded at 100k cells/cm² onto the RGD:alginate within externally controlled

316SS bioreactors. After 3 days, to increase the efficiency of the endothelial cells, the perfusion bioreactor was set to a volumetric flowrate of 0.1 mL/min through day 5. **Figure 6.12** through **Figure 6.14** show representative images of the HUVECs seeded onto the TCPS control and the RGD:alginate prior to, and post perfusion.

HUVECs on TCPS Control X7 Day 1 Day 2 Day 3

Figure 6.12 Representative images of HUVECs seeded onto standard TCPS well plates.

316SS Bioreactor Prior to Flow

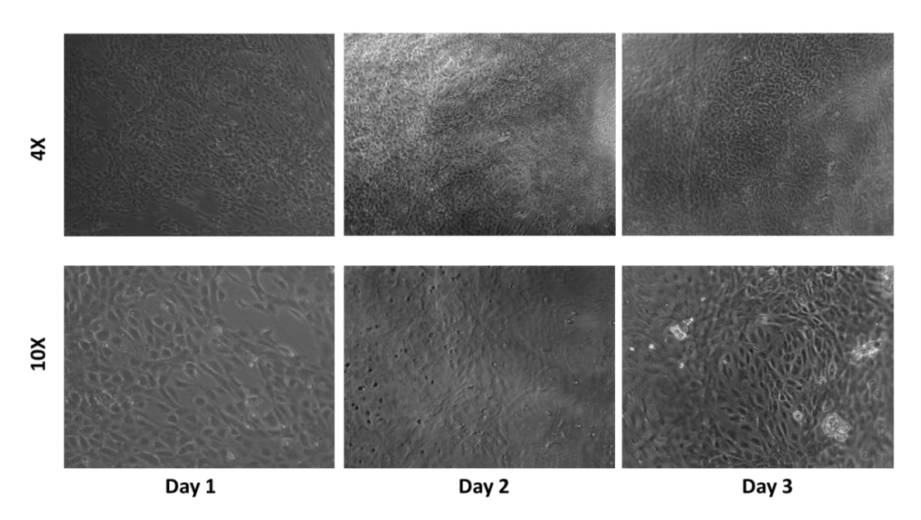


Figure 6.13 Representative images of HUVECs seeded onto RGD conjugated alginate within a 316SS externally controlled bioreactor prior to perfusion.

316SS Bioreactor w/Flow at 0.1 mL/min

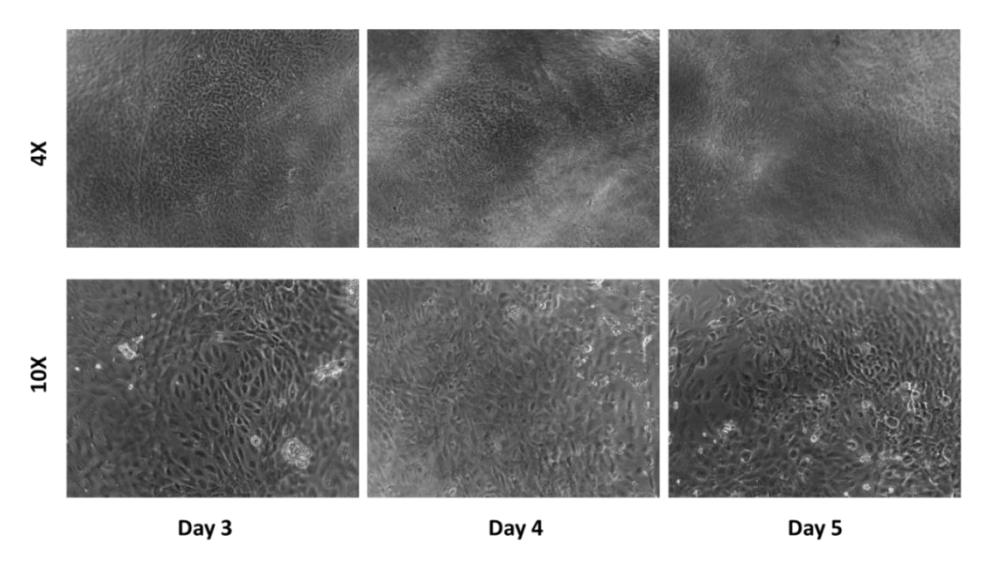


Figure 6.14 Representative images of HUVECs seeded onto RGD conjugated alginate within a 316SS externally controlled bioreactor during perfusion.

HUVECs thrived in all situations mentioned previously, with and without flow. Therefore, the RGD conjugated alginate appeared to be a functional biomaterial for endothelial cell culture.

6.2 Conclusions

The efforts described in Chapters 5 and 6 have exhaustively demonstrated the feasibility of using injection molded, water-soluble PVOH components for the fabrication of hydrogels with defined internal hydrogel architecture, e.g. channels or lumens, to shape tissue morphology at the micro-to-millimeter scale. It has been shown that all of the materials and system components of the perfusion bioreactor system have yielded functional cell growth promoting environments. Therefore, the groundwork for this flexible tool has been laid for future cell culture experiments and research.

6.3 Future Work

Future work on this research should be carried out in two areas:

- Display microvasculature networks permeating throughout alginate hydrogel networks
- Explore minimum achievable injection molded feature size with PVOH/Ca composites

The next step for this research would be to produce microvasculature networks with confluent layers of endothelial cells adhering to the entirety of a channeled hydrogel's lumens. This work will require cell culture and materials expertise which will optimize cell-hydrogel interactions and allow for sustainable microvasculature creation. Further,

collaborations with other tissue engineering experts could develop complimentary cocultures with dissimilar cells. Much of this work has already been started and characterized by another member in this lab but was not the scope of this thesis.

In order to accelerate the advancement of tissue engineering, additional research needs to be performed on the minimum feature size producible in this fashion. Rapid thermal cycling of the injection mold temperatures should be one method for increasing the L:D aspect ratio of the micro-injection molded components and thereby the capabilities of this new technology. Not only will this have implications for tissue engineering research, but for industrial applications such as micro-replication of small features on large scale components.

7 A Method for Creating Internal Geometries in Injection Molded Parts Using Water-soluble Polyvinyl Alcohol (PVOH) Inserts

In the modern global market companies differentiate on the basis of innovation and speed of development. In this study, we experimented with using water-soluble polyvinyl alcohol (PVOH) patterns to create internal geometries within injection molded parts. This process can help develop and mass-manufacture complex parts with internal geometries and undercut features faster and more economically than other industrial alternatives. By overmolding sacrificial PVOH patterns with a non-water-soluble polymer shell, and subsequently dissolving the inserts, diverse internal features were fabricated with traditional injection molding equipment. Metrological analysis performed on the components has shown that precise control of the internal dimensions is possible over a wide range of processing temperatures and conditions. White light interferometry analysis conducted on the surfaces of the PVOH patterns and shell materials show that the process is capable of replicating microscale features and decorations onto the internal surface of the molded components.

7.1 Introduction

As technology advances, manufacturing engineers are constantly forced to innovate with new materials and processes to keep up with the demands of the ever changing global market. Nowhere has this phenomenon been captured more than the field of polymer and composite processing [72]. Recently, there has been much research performed regarding the injection molding process and its variants to improve component surface aesthetics, reduce material density, and increase process economic efficiency [81, 103, 183-188].

Traditionally, injection molding has been a widely used process for mass producing dimensionally stable polymer and composite components with critical geometries in three dimensions. While the process is used in countless industrial applications globally and has been discussed in great detail elsewhere [189, 190], there is always room for improvement and innovation, especially in the area of multi-component assemblies. Historically, the design of products which house electronics, fluid flow, or internal features have required an assembly where interior geometries must be formed by the mechanical fastening of two or more subcomponents.

Upon initial inspection of the assembly methods such as ultrasonic welding and mechanical fastening, the manufacturing concerns become apparent. Each method requires numerous injection molds to manufacture the subcomponents, labor or automation to perform the assembly, and expensive post-processing equipment which can raise the costs of goods sold and ultimately decrease the profit margins [191, 192]. Additionally, for polymer components assembled with fasteners and ultrasonic welding, one of the requirements is that the material be thicker at the fastening joint, thus increasing material usage [193-195]. Besides the undesirable material waste, post operations of welding, bonding, or fastening can be identified as the weakest sections in the part, thus increasing the tendency of the part to fail at that site. Moreover, release agents and oils may contaminate the resin from the molding process and cause poor adhesion during welding and bonding. Despite the challenges listed above, these processes are still popular among plastic part designers due to the lack of a cost effective alternative.

The need for further research in this area is further exemplified by the recent introduction of collapsible and lost (fusible) core technologies, which have been developed to

avoid the drawbacks of the mechanical fastening methods presented above. Collapsible cores are used to create internal geometries in many components, typically female threads and light undercuts, but there are significant limitations regarding the severity of their depth [196, 197]. Lost core injection molding or the fusible core process, as the name suggests, involves the use of a low melting point alloy as a sacrificial pattern to be overmolded with a polymer or composite external shell [198, 199]. This process is typically used for manufacturing components with complex internal features without the need for subcomponents or assemblies. While the resulting products can be impressively complex, the systems required to produce such components are staggeringly expensive and intricate. A simplified explanation of the lost core process is where a sacrificial alloy pattern is manufactured using a die casting technique prior to insertion into an injection molding press for overmolding [200]. After the molding cycle is complete, the polymer–alloy composite is subjected to a heating procedure above the melting temperature of the alloy causing it to liquefy and flow out of the polymer shell.

Since the lost core process requires the alloy to melt at a lower temperature than the polymer shell during the heating phase, this limits the polymer materials that can be used to only those that can withstand high temperatures for long durations. This, plus the significant cost required to produce the alloy pattern using a die casting procedure, along with the long cycle times and energy required during the heating phase, limits the use of this process to high volume products for high performance applications with large profit margins. As a reference point, data suggests that the capital investment required to perform the lost core process is upwards of \$8M [72].

In order to reduce the costs associated with the lost core process, research has been performed on variants that utilize sacrificial cores made from glass beads or bound sand which may be disintegrated or dissolved, respectively, without the heating phase [201, 202].

In this study, a sequential molding process analogous to the lost core method has been investigated. The objective was to develop a process which could perform as well as the lost core method without the expense or equipment requirements. The resultant process exploited the use of polyvinyl alcohol (PVOH), a water-soluble polymer that could be injection molded into a sacrificial pattern and subsequently inserted into a secondary injection mold for overmolding with another polymer shell [203]. Afterwards, the composite was subjected to a room temperature water bath that dissolved the PVOH, leaving behind the polymer shell with internal features matching the PVOH pattern.

Besides the fact that PVOH is water-soluble, its mechanical properties make it an ideal option for an overmolding insert. Being that the thermal conductivity and diffusivity of PVOH is similar to that of most other polymer materials; the overmolding procedure does not significantly modify the surface roughness and feature dimensions of the insert. Furthermore, manufacturing the sacrificial pattern from a PVOH pattern allows the use of the same overmolding equipment and processes as traditional polymer processing. Lastly, the absence of elaborate and energy-intensive core removal procedures makes this an optimal technique for manufacturing limitless components with internal and external complexities.

Low density polyethylene (LDPE), polypropylene (PP), and polycarbonate (PC) are among the three most commonly used thermoplastics in commercial and industrial applications. In particular, the polyolefin family, which includes LDPE and PP, has been used heavily in consumer products industries due to its wide processing window, resistance

to fatigue, and low cost. PC has been selected as a material of choice where criteria such as transparency, scratch resistance, strength, stiffness, and dimensional control are of importance. For these reasons and more, LDPE, PP, PC, and their composites form a substantial share of injection molded polymer resins. Here, they have been used as the overmolding materials to demonstrate the PVOH sacrificial injection molding techniques potential for making microscale internal geometries with a variety of surface features. Interestingly, although PVOH has a melting temperature of 185°C and typically would degrade at the higher melting temperatures of PP and PC, PVOH's high thermal inertia ensures that the surface temperature of the PVOH pattern will remain below its melting temperature during the process of overmolding, thus retaining its initial geometry.

7.2 Experimental Methods and Materials

LDPE (Marlex, Chevron Phillips Chemical Company), PP (Pro-fax SR256M, LyondellBasell Montell), PC (Lexan 143R, SABIC), and PVOH (MonoPol C100, Monosol) were acquired from commercial vendors and used as received. Custom injection molds (Figure 7.1) were designed with 3D modeling software (Solidworks 2014, Dassault Systemes) and fabricated from 6061 aluminum with a computer numerical control (CNC) vertical machining center (MiniMill 2, Haas) programmed with computer aided design/manufacturing (CAD/CAM) software (MasterCAM X7, CNC Software, Inc.). All injection molding was performed on a 38 ton Arburg Allrounder 270A machine with an 18 mm injection unit with processing parameters found in Table 7-1 below. The morphology of the PVOH and shell material interfaces were evaluated using white light interferometry (NewView 7300, Zygo) after sputtering gold onto the surfaces (90 s at 45 mA).

Table 7-1 Injection molding process parameters

Injection Molding Process Parameters									
Parameter	Units	PVOH	PP	PC	LDPE				
Injection pressure	bar	1500	1500	1500	1500				
Injection speed	cm ³ /s	8	15	15	15				
Holding pressure	bar	1000	850	1000	500				
Holding time	s	2.25	2.25	2.5	1.25				
Mold temperature	°C	43	43	43	43				
Material temperature	°C	190- 200	210- 220	240- 265	170- 180				
Cooling time	s	20	20	20	20				

7.2.1 Injection Mold Design

To determine the flexibility of the sacrificial injection molding procedure, injection molds were manufactured with a variety of features including ribs, bosses, and holes (**Figure Figure 7.1**). After molding the PVOH patterns, they were subsequently overmolded with LDPE, PP, and PC.

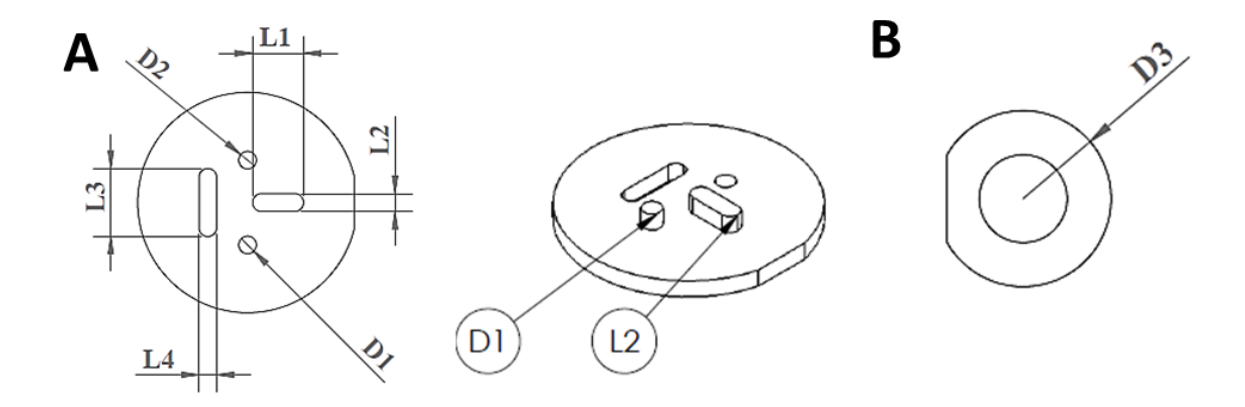


Figure 7.1 Custom designed components for injection mold tooling. Sacrificial PVOH components for assessing (A) geometric dimensional stability and (B) surface roughness.

The overmold tooling was built 6 mm deep with a diameter matching the outside diameter of PVOH insert A. Thus, upon completion of overmolding, there were 2 assemblies with internal PVOH subcomponents (cf. **Figure 7.2**).

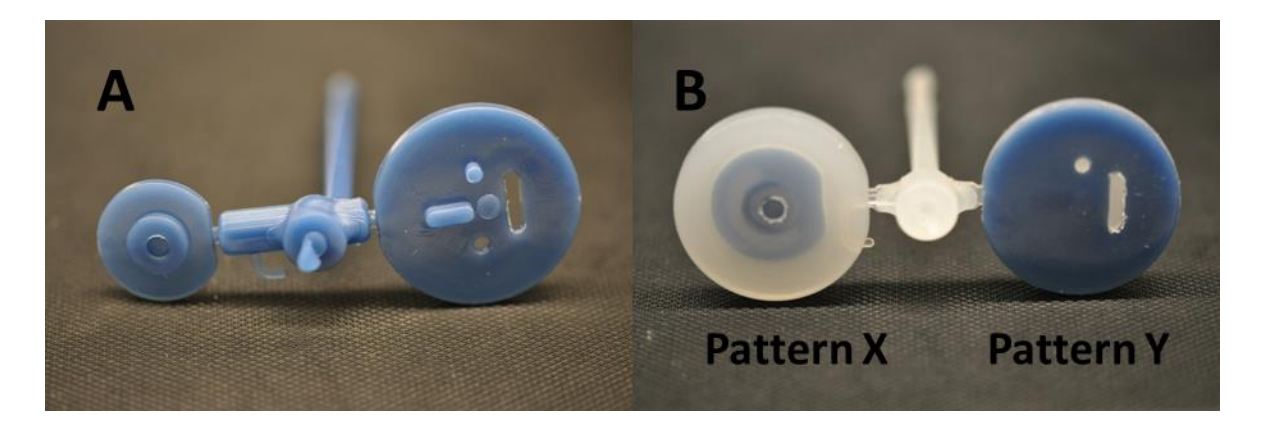


Figure 7.2 (A) Image of PVOH molded patterns in blue pigment and (B) image of PVOH molded patterns overmolded with LDPE.

As can be seen in **Figure 7.2**, the two types of PVOH patterns were molded to serve different purposes. Pattern Y was designed to be overmolded solely on one side, whereas pattern X was designed to be completely encapsulated during the overmolding procedure. Post overmolding, the assemblies were submerged in a water bath at 60°C until the PVOH

insert completely dissolved. Subsequently, the dimensions of the remaining shell materials were measured and compared to the corresponding dimensions on the PVOH patterns, as noted in **Figure 7.1**. In addition, the surfaces of the shell materials formed by the PVOH patterns were assessed using white light interferometry to assess whether or not the PVOH surface texture was modified during the overmolding process.

7.3 Results and Analysis

7.3.1 Metrology and Dimensional Analysis

The dimensional accuracy of the features formed in the shell materials using the PVOH pattern overmolding procedure were evaluated by comparison to the initial PVOH pattern dimensions. Prior to overmolding, a sample group of ten X and Y patterns were measured and the critical features noted in **Figure 7.1** were recorded. After overmolding the patterns with the shell materials and dissolving the PVOH, the relief features were measured again. For samples entirely encapsulated, the shell was machined to expose the internal cavity for measurement. All dimensions were consequently recorded and compared (**Figure 7.3**).

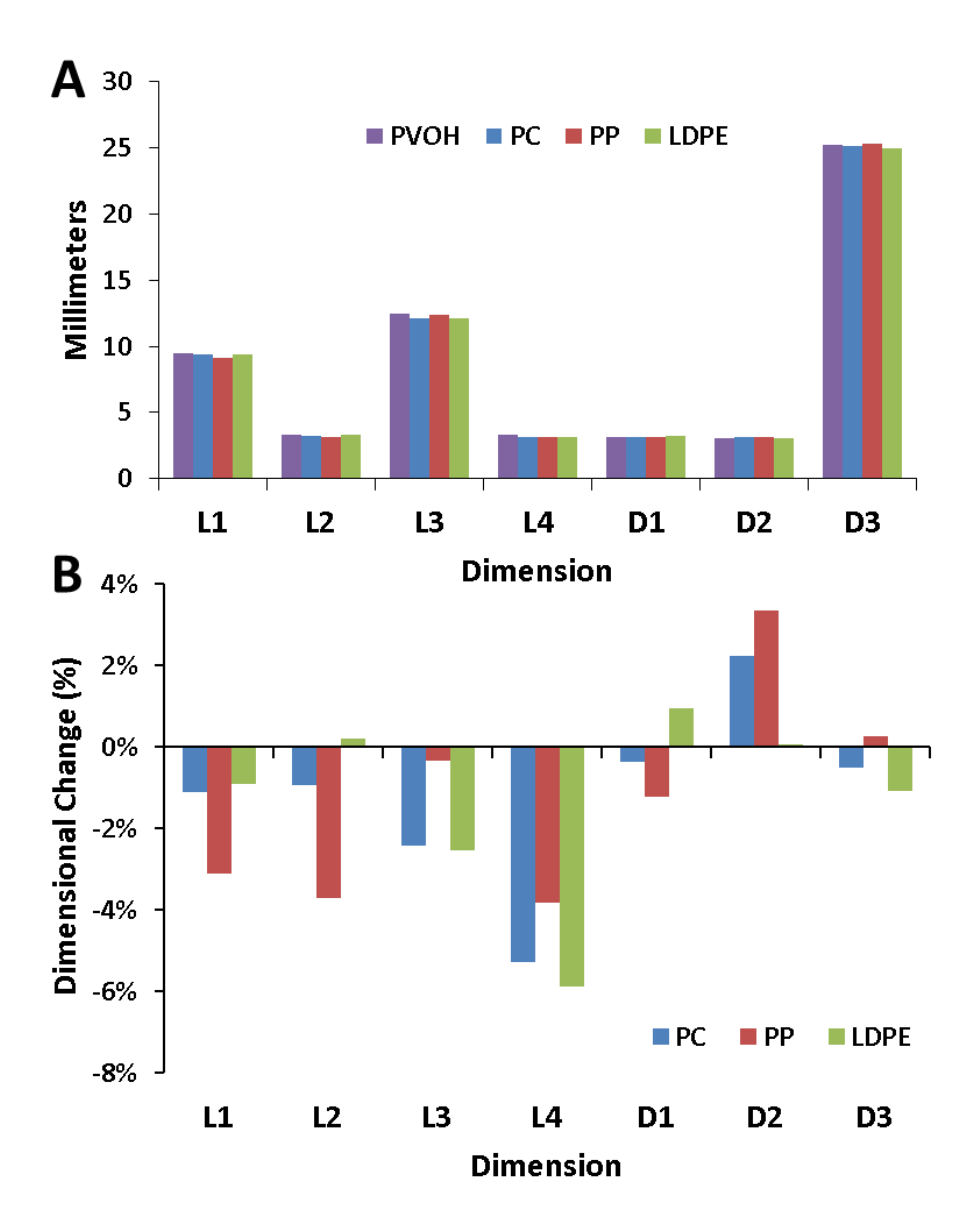


Figure 7.3 (A) Average measurement of all critical dimensions for all each material. (B) Average percent deviation of critical dimensions as compared to the initial PVOH pattern dimensions. The sample size was 10.

As the data suggests, there is an overall less than 6% (less than $320~\mu m$ absolute) change in the dimensions as compared to the PVOH pattern for the relief features in the shell material. Although this trend suggests that the relief material dimensions shrunk as compared

to the patterns, this propensity is not definite as can be seen regarding dimension D2, which is a cylindrical hole.

7.3.2 Surface Morphology Analysis

White light interferometry was used to assess any change in surface morphology due to the interfacial temperature, shear, or pressure imparted by the overmolding process. The PVOH patterns were molded with both milled and surface ground regions on the tool cavity. Four experimental groups were analyzed to see how the various overmolding materials responded to the tooling finish (**Figure 7.4**).

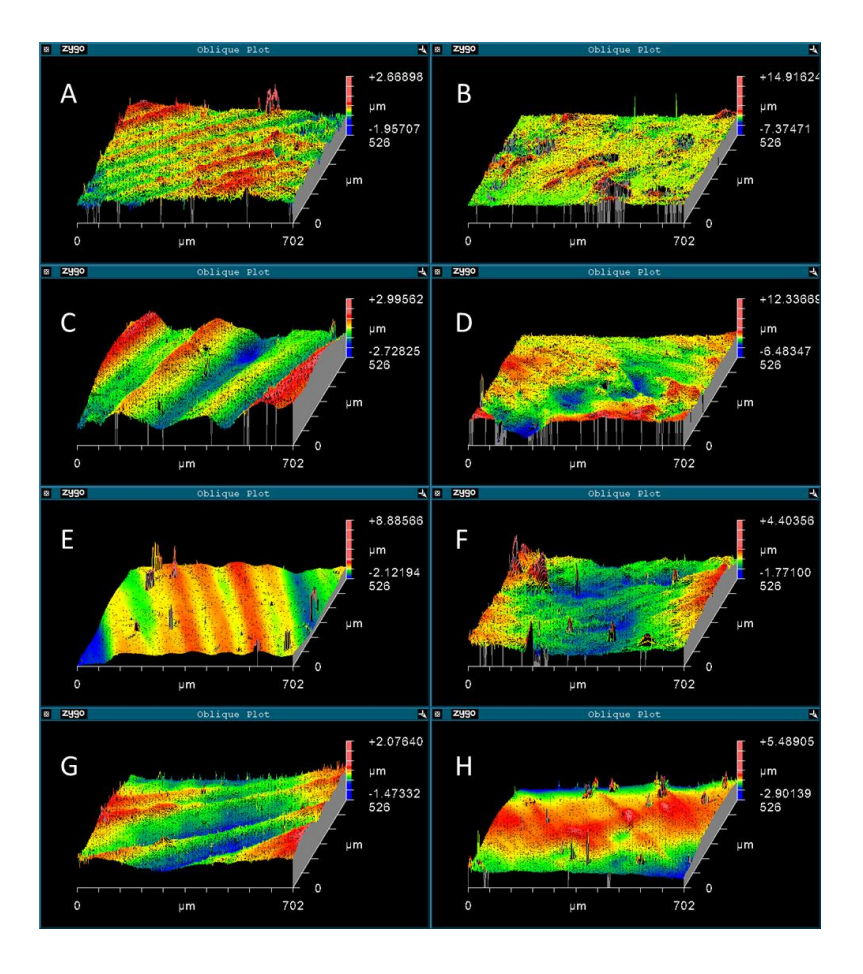


Figure 7.4 Surface morphology of (A) milled PVOH pattern, (B) surface ground PVOH pattern, (C) milled LDPE relief, (D) surface ground LDPE relief, (E) milled PP relief, (F)

surface ground PP relief, (G) milled PC relief, and (H) surface ground PC relief. All units in µm.

Observing the oblique plots reveals that the surface roughness of the PVOH insert was transferred onto the shell material with little deformation. The similarities in surface roughness between the insert and the overmolded substrate indicate a transferal of surface texture due to the strong dimensional stability of PVOH. This ability to transfer microfeatures from the PVOH pattern to the overmolded material would allow for greater control of the final product compared to similar methods such as the lost core process. Further implications of this result infer that, using the sacrificial PVOH overmolding process, internal microreplication of injection molded parts could be realized. Additionally, one could expect that if the technique were to include the use of in-mold labels or decoration, these features could also be directly transferred onto the shell material in a similar manner. One potential application of this technique could be the fabrication of scaffolds for tissue engineering with complex, controllable internal dimensions.

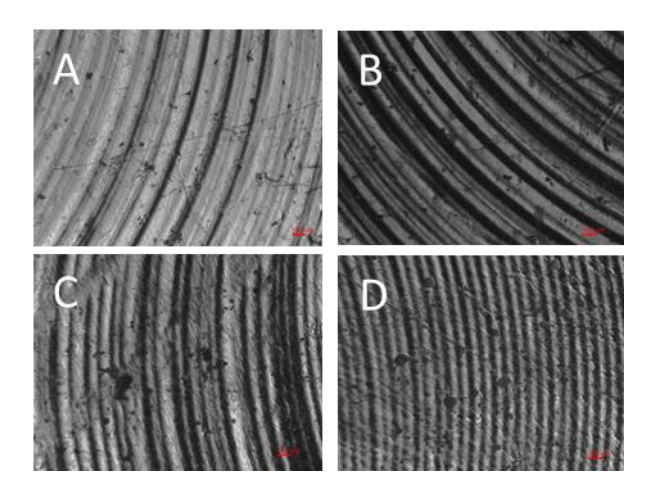


Figure 7.5 Optical microscope images displaying surface morphology of (A) PVOH patterns and the relief surfaces on (B) LDPE (C) PP and (D) PC substrates.

7.4 Conclusion

In this study, an approach for creating internal features and geometries on injection molded plastic components has been experimentally tested. By overmolding sacrificial PVOH patterns with a shell layer, and subsequently dissolving the patterns, various internal features can be manufactured within the component. Compared to current alternatives, this process has abundant benefits including low capital investment, singular post processing operation, and avoidance of complex injection molds and equipment. Furthermore, the dimensional analysis performed on PVOH overmolded samples with LDPE, PP, and PC has shown that precise control of the internal dimensions is possible over a wide range of processing temperatures and conditions. Future work on this process could yield a promising predetermined compensation value to accommodate deformations of the PVOH features during overmolding. This would allow tool manufacturers to fabricate molds with more speed, precision, and confidence on their first attempt.

White light interferometry analysis was conducted on the surfaces of the PVOH patterns and shell materials highlight the process's ability to replicate microfeatures and patterns onto component internals. The fact that the thermal conductivities and thermal diffusivities of the polymers were similar induces an interfacial temperature directly between the molten overmolding material and the room temperature PVOH pattern. This allows for the PVOH patterns to be overmolded with materials that exhibit a melting temperature well above that of the PVOH without any harm. Taking advantage of this phenomenon allows for much greater versatility with regard to injection molded component design, including the

possibility of transferring microfeatures and forming internal complexities within the polymer parts.

In today's fast paced innovative markets, where uncertainty of product life cycles is increasing, this sacrificial PVOH overmolding technology can offer a consistent method of manufacturing nearly limitless forms of undercut features and internal geometries in plastic molded parts, while reducing capital investment in complex molds, machinery, and manufacturing processes.

8 Conclusions and Future Work

The cross-disciplinary research outlined throughout this thesis discussed in great detail multiple enabling technologies aiming to provide spatial and temporal control of human tissue morphology and microenvironments. First, a robotic microcontact printing system was developed to produce highly uniform spatially organized 2D substrates with unparalleled accuracy, precision and sequential patterning abilities. Next, a process was established using microinjection molding to fabricate highly-complex 3D hydrogel scaffolds with internal and external microscale architectures. Lastly, a similar overmolding process was then evaluated for potential industrial applications in cost reduction and tooling simplification. Moving forward, the future work on this research will be carried out on three fronts:

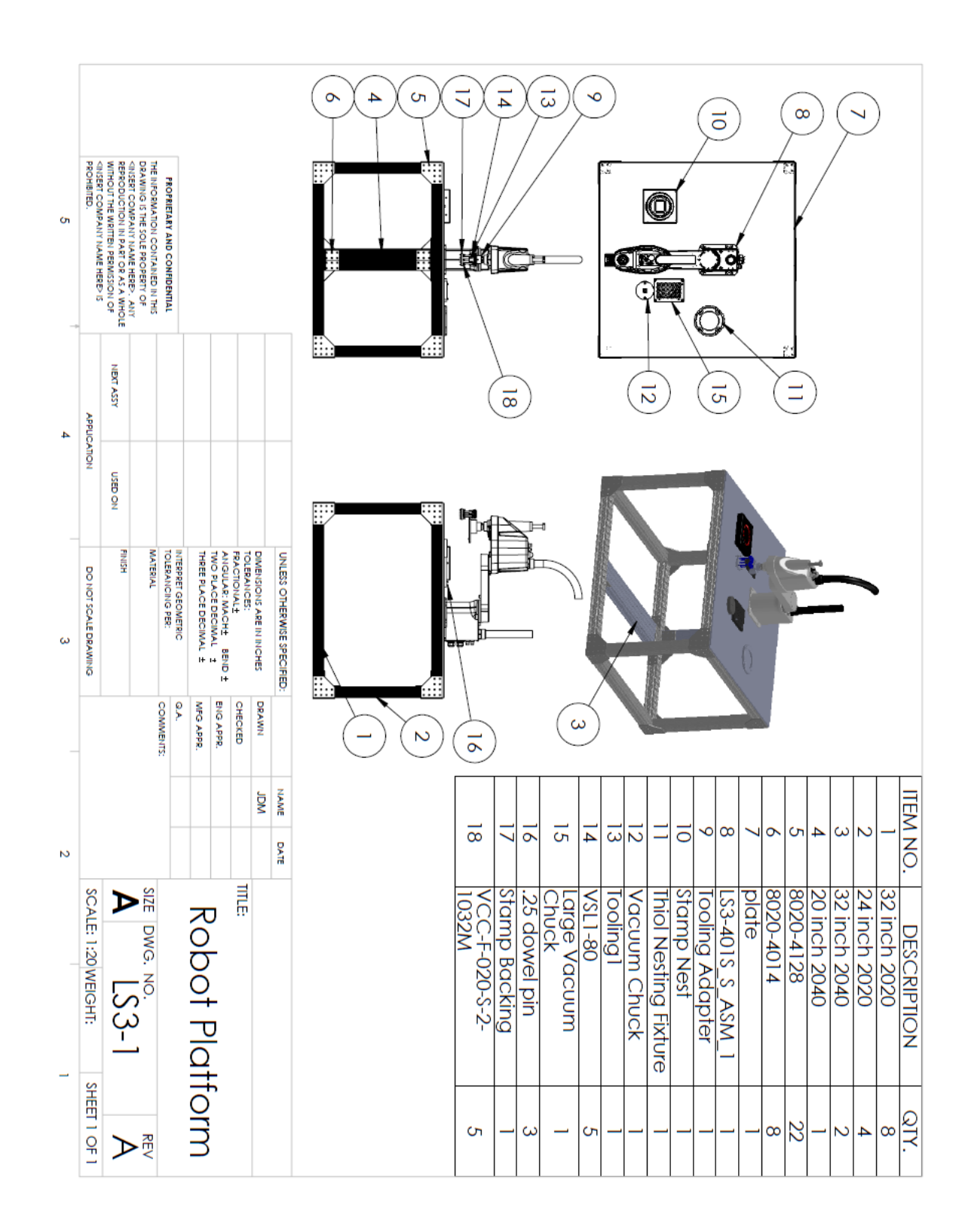
- Explore the capabilities of injection molding sacrificial PVOH/Ca composites
 in the microscale dimensions with high L:D aspect ratios using rapid mold
 heating and cooling (RMHC) techniques;
- Further develop template designs to propel the use of the sacrificial injection molding technology into useful 3D environments for biomedical applications;
- Incorporate the use of R-µCP with the micropatterned multiwall plate technology developed within our group at the Wisconsin Institute for Discovery [161].

It is the expectation that the research provided within this thesis will be used and modified to aid in the accelerated development of clinically viable regenerative therapeutics.

Appendix I – Sacrificial Molding SOP

- 1. Collect Mowiflex 232 PVOH pellets from Kuraray
- 2. Acquire Ca(C₂H₃O₂)₂ from http://www.sciencecompany.com/
- 3. Dry all materials in vacuum oven
- 4. Use the Leistritz twin screw extruder in WID fab lab to produce composite
 - a. Use all feed forward elements
 - b. Use Schenck Accurate feeder @ starving feed rate
 - c. Use processing parameters found in Table 5-1
 - d. Use the blue conveyor belt to maintain consistent draw ratio
 - e. Feed composite into pelletizer to chop strand into <3/16" pellets
- 5. Use the Arburg injection molding machine in the WID fab lab to produce sacrificial templates
 - a. Use 3x5" MUD mold system w/ aluminum molds
 - b. Use processing parameters found in Table 7-1
 - c. Existing files are located in the StartUp folder on the Arburg compact flash

Appendix II - RµCP Platform 2D Drawing



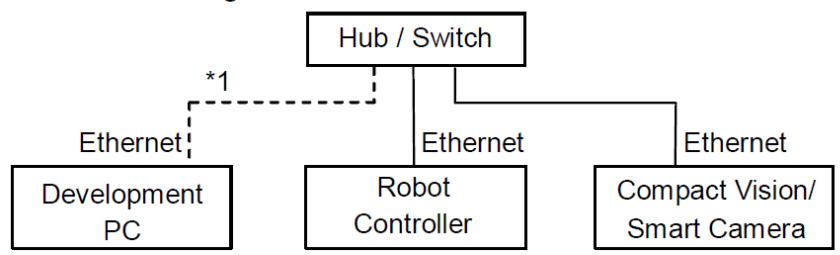
Appendix III – Epson RC+

The Epson LS3 SCARA robot uses the RC90 controller and RC+5.0 software. It has been determined that RC+5.4.5 along with RC90 firmware version 3.4.2 should be used along with a non-Dell brand PC. Not following these instructions may result in corrupt program files, non-functional GUI option and frequent connectivity issues.

Ensure the software is installed on the PC prior to connecting with the RC90 controller. In order to use more than 1 CV camera, use the Ethernet option from the RC90 controller manual below:

<Typical Cable Connection 2>

Compact Vision, Smart camera, PC, and Robot Controller need to be connected in the same subnet using a switch or hub.



- (1) Connect an ethernet cable between the camera and the hub.
- (2) Connect an ethernet cable between Robot Controller and the hub.
- (3) Connect an ethernet cable between the PC and the hub.
- *1 When Vision Guide 5.0 is enabled, you must connect the controller, camera, and development PC as shown above.

When the image of the camera in not monitored at operating the robot system, you do not have to connect the PC to use the Vision Guide 5.0.

Once connected, turn on main power switch on both – front of the RC90 controller and the power strip in rear of enclosure. Open Epson RC+ 5.0 software on PC and wait until the RC90 is completely initialized. In the RC+5.0 software, select Ethernet 1 in the

connections dropdown and connection will be established. Once connected, ensure Rucp

program is loaded by File>Open>Rucp. File locations will be saved in

C:\EpsonRC50\projects. When communicating with Epson applications support, always Zip

the desired project folder and send via Box or similar.

SCARA robots such as the LS3 move throughout their global coordinate

system from trained point-to-point via specific commands. Each point is 'taught' or

programed from other taught points. The robot saves the position of each joint and will return

to the exact configuration when prompted. Commands available in the SPEL language are

explained in the SPEL language reference PDF (through the help menu). It is important to

verify that when moving between points that the tooling does not come into contact with any

fixtures.

The RC+ software is used to write executable programs within larger project

files. An example of a program can be seen below with all of the required components.

Function main

Motor On

Power High

Jump P01

Go P02

Arc P03, P04

Jump P05

Jump P01

Power Low

Motor Off

Fend

When combined with a CV1 vision camera, the Epson RC90 can make use of complicated vision sequences which identify, locate and can screen objects of importance. To learn more about the vision sequences, read the Vision Guide 5.0 User Guide and Reference PDFs in the help menu.

For the R- μ CP project, the RC+ software was used to perform the following actions:

- Pick up the PDMS stamp
- Locate the center and orientation of the PDMS stamp using vision tools
- Locate the center and orientation of the gold coated glass substrate using vision tools
- Submerge the PDMS stamp's micro-features in an alkane thiol bath
- Dry the ethanol in a nitrogen stream
- Align the PDMS stamp with the gold coated substrate
- Perform micro contact printing

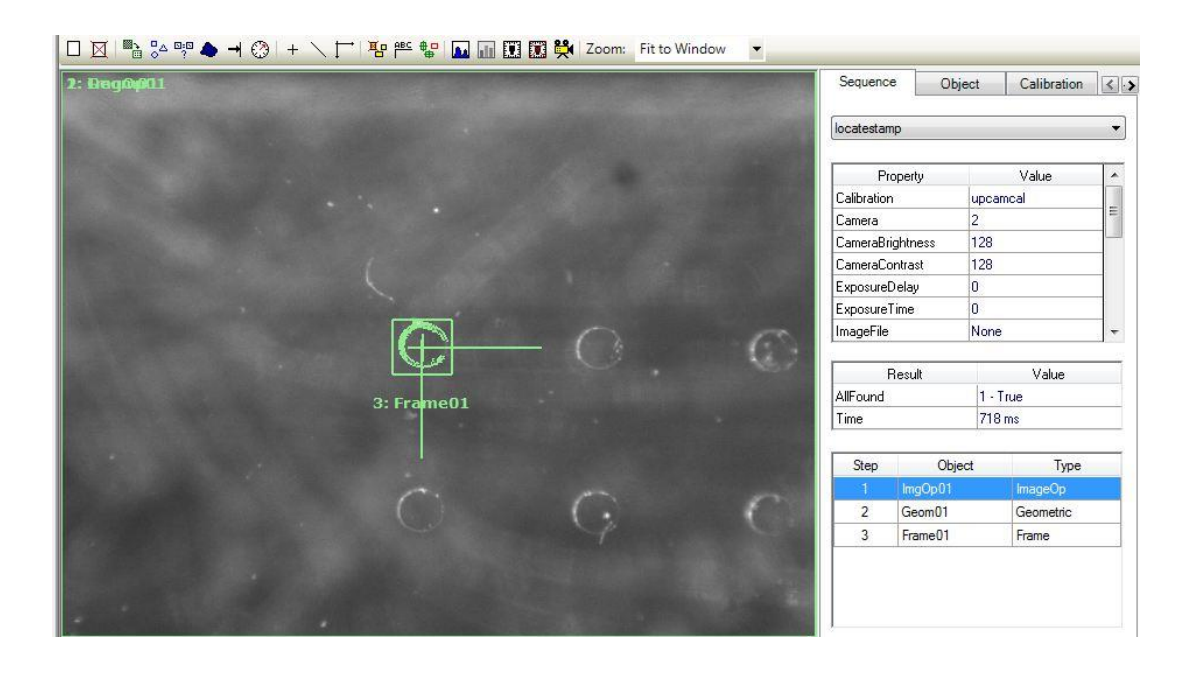
The vision sequencing of the components was the more complication portion of this project. Specifically, what tools to use, thresholding, and enabling angle and relocation recognition. Before proceeding with any sort of vision testing, it is recommended that the user first attempt to learn the process on a simple object, like a washer or paperclip. Next, ensure that whatever object, is in the focal plane.

The tools explained in the next portion of this appendix are the ones found to be most helpful in the R- μCP substrate location. Following this brief tutorial should assist in further implementation of new programs.

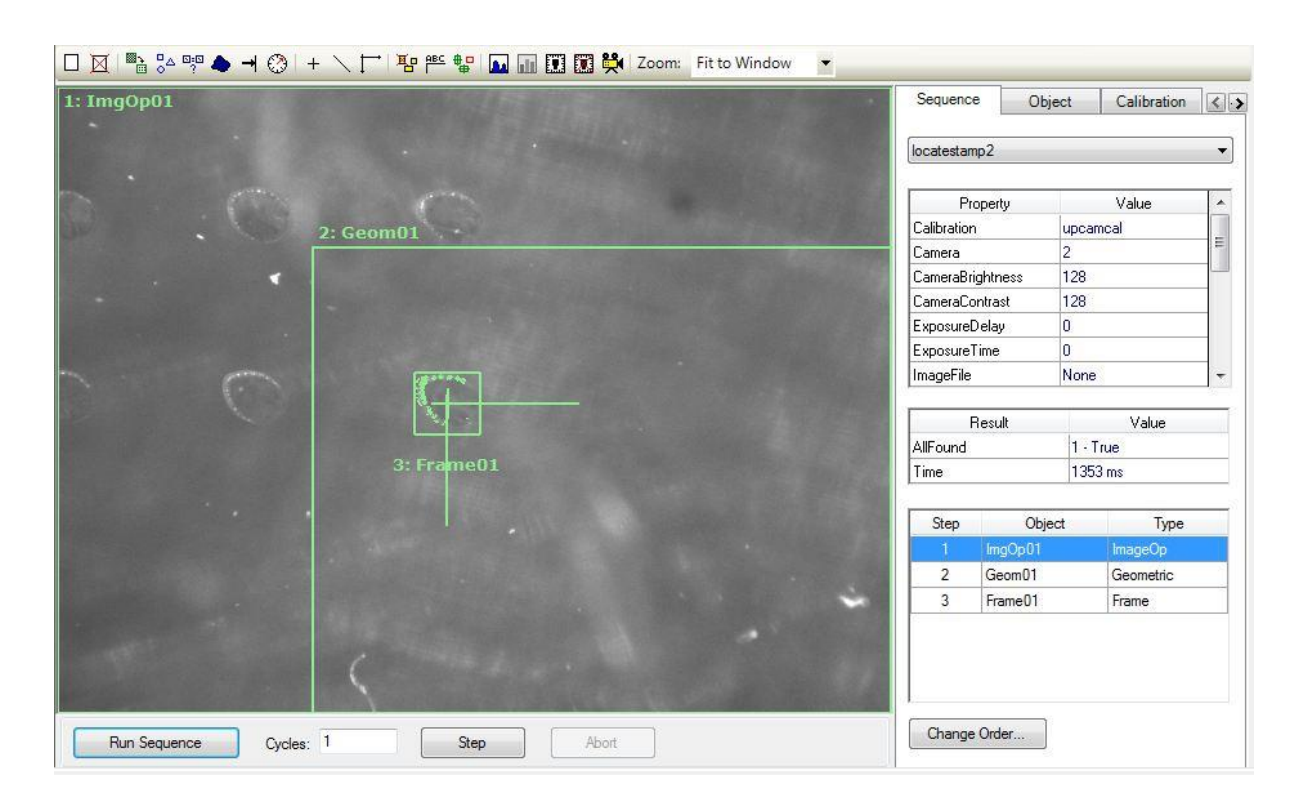
- Blob
- Frame
- Edge detection
- Line

- Point
- Image operations

A PDMS stamp with an array of 300um diameter wells was raised into the focal plane above the upward facing camera, within the LED ring light. After calibrating the cameras, a sequence was created to locate 2 opposite corner most features. To create a vision sequence, select Tools>Vision. Select New Sequence, the feature pane to the right allows the selection of the calibration method and the camera number. Next, select New Image Operation to make the features more defined. The Image Operation type was selected as Edge Detect 1, and the window was set to the entire FOV. Additional options can be changed such as the intensity, thresholding and brightness. Next, New Geometry Object was created and set over the corner feature. The image operation was run and then the geometry object was trained. Polarity and thresholding can be set again for this tool. Lastly, a Frame was created and the Origin Point was defined as Geom01 with Angle Enable On.

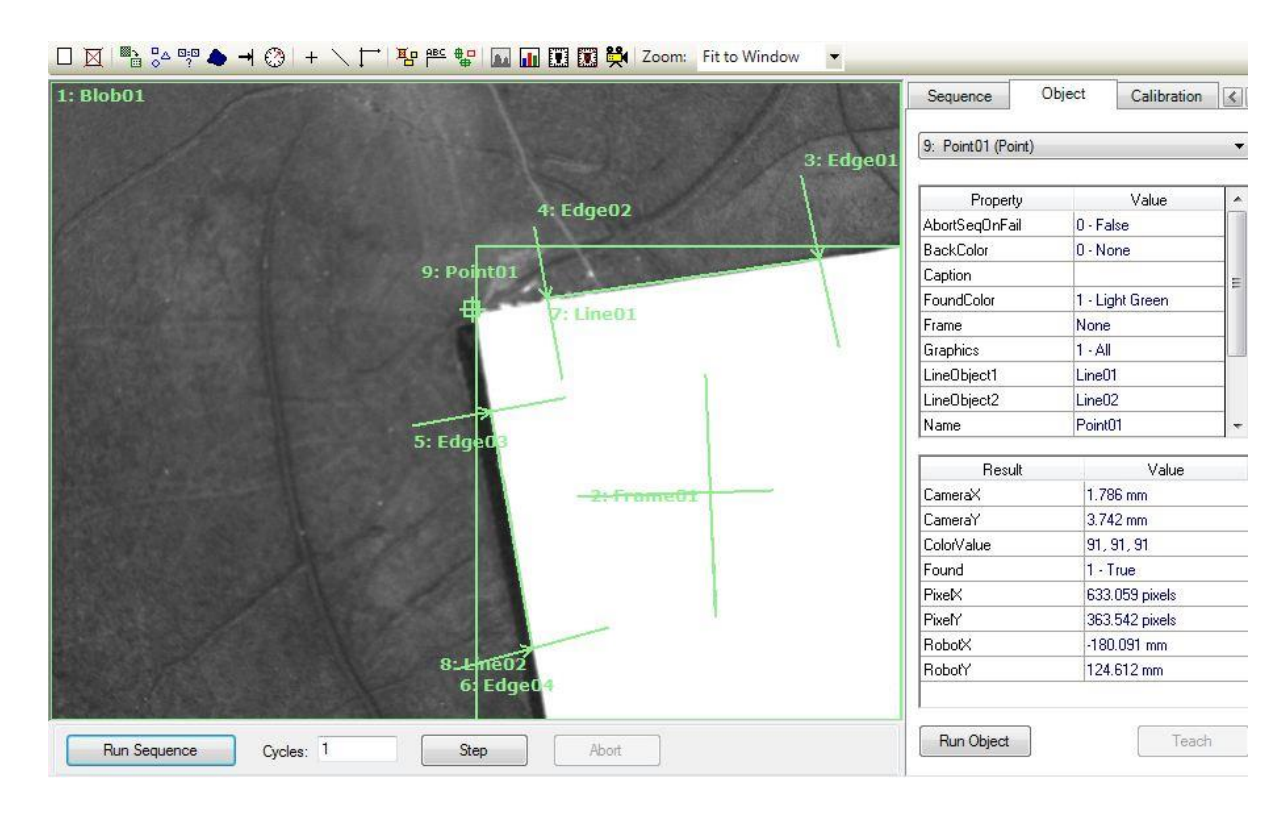


The other corner feature was then identified in the same manner, but it can be seen that the Geom01 window was shrunk in order to prevent additional feature distraction.



Next, the downward facing camera was calibrated and positioned above the corner of the glass substrate. Aperture and focus were adjusted in order to view the slide the best. In this case, a Blob was set to binarize the entire FOV and locate the center of the largest 'white-on-black' object. The threshold and size settings were manipulated until the slide was entirely white, and the background was black. The Frame was positioned in the sequence and Origin set to the Blob01 with Angle Enable set True. 4 edge detection tools were placed in a layout shown in the following image with 2 line tools spanning the gap between the Edge tools. The edge tools were set to locate from Black-to-White with reference frame set to Frame01. The line tools were each set to start and end at their respective edge tools. Finally,

a Point was placed in the sequence at the corner of the slide. In the Point01 settings, the origin was selected as 'Intersection" between line objects Line01 and Line02. Running the sequence locates all objects, and the Point01 exports RobotX, RobotY.



Discussion with Epson on this topic yielded the discovery of another useful Epson feature – Coordinate Systems. The following section describes the development of local coordinate systems and how they can be useful in coding.

Knowledgebase Article

Date: 2/17/12 Product: SPEL+

HowTo: Create a Local Coordinate System

The SPEL+ "Local" command is used for handling coordinate transformations. Rather than teaching points in the Robot's World Coordinate system (which we refer to as Local "0") you can create your own coordinate systems.

"Local" coordinate systems can be defined using either one point, two points or three points. A 3D Local (defined using 3 points) is primarily used with 6 axis articulated robots. A six axis robot can manipulate so that the tooling is perpendicular to the tilted/skewed Local. In geometry three distinct points define the equation of a plane. Conceptually you might want to think of a Local coordinate system as a plane. Technically it is a coordinate frame. I would like to explain the concept of Locals by using a piece of paper. Draw a point on the bottom left corner of the paper and label the point "P0". "P0" will be the origin of our Local coordinate system. Draw a point at the bottom right corner of the paper and label it "P1". The vector from "P0" to "P1" will be the "X" axis of the Local coordinate system. Draw a third point in the upper left hand corner of the paper and label it "P2". "P2" does not need to lie perfectly on the "Y" axis of the new Local coordinate system. "P2" actually determines the yaw and pitch of the Local. Here are the actual steps that you will need to take to implement a Local using points P0, P1 and P2 ->

- Define a Tool Offset for your end of arm tooling. Go to the EPSONRC+ 5.0|Robot Manager|Tools Tab|Tool Wizard to create a tool offset for the gripper.
- From the EPSONRC+|Tools|Robot Manager|Jog and Teach tab, teach points "P0", "P1" and "P2" (as explained above) in the appropriate Tool. Please note that "P0", "P1" and "P2" will be taught in the Robot's World Coordinate system (Local "0").
- Go to the EPSONRC+ 5.0|Tools|Command Window and type the following command -> > Local 1, P0, P1, P2

This will create Local "1".

 This step is not necessary but may help you understand what is going on. In the EPSONRC+ Command Window, type ->

> Local

You will now see that the 3 points that were used to create the Local have now been changed into a single point whose UVW coordinates define the yaw, pitch and roll of the Local. The XYZ coordinates are the origin of the Local.

- 4. To teach a point in the newly defined Local coordinate system, you can either ->
- a) Open the Jog and Teach page, select "Local 1" from the "Local" list box at the top of the dialog, jog the robot to the desired location and click "Teach". Or...
- b) In your program you can define the points in the new Local. For example ->

P10= XY(0, 0, 0, 0, 0, 0) /1

This will put P10 at the origin of Local "1". When you want to specify that a point is in a local, you must use the forward slash "/" followed by the Local number.

Please note that a "Z" coordinate of "0" means that the point lies on the plane of the Local (even if the plane is skewed and tilted)

c) You can also define a point in a Local by opening the EPSONRC+ Point Editor and typing in the coordinates and selecting the appropriate Local number.

Lastly....

Use the "@" sign to translate coordinates from one coordinate system to another.

For example, here is how to teach the current position of the robot relative to Local 1's origin rather then relative to the origin of the Robot's World Coordinate system.

P100 = Here @1

Additional Example:

Here is a simple example of how to use a pallet in a local coordinate system (that was defined with a single Point Local). If you change the coordinates of "P0" then the Local will be repositioned. When the local coordinate system is moved, the pallet will also move accordingly.

Now that I have explained how to create a Local from "scratch", EPSONRC+ also includes a "Local Wizard" (EPSONRC+ 5.0|Robot Manager|Locals Tab|Local Wizard) that will assist you in the creation of Local Coordinate Systems.

Author of the Article: John Yett

Appendix IV – R-µCP Code (Fall 2015)

Function arbitraryloc

'This program is used to pattern small glass (cut or not) on the small vac chuck

'It will pattern without any vision sequences

'It can be used to pattern in place of hand stamping OR calibrating hard stops

Real area, x, y, z, u, n 'define variables

Real x1, x2, x3, x4, y1, y2, y3, y4, theta, theta2, stamp

Power Low 'set motor power to Low

Tool 2

Jump Calstamploc

P103 = CurPos 'set a temporary point that will change with torque measurements

Do 'enter loop

ATCLR

Wait (2) 'wait 2 seconds before torque measurement

Real rawTorque, percentTorque

rawTorque = ATRQ(3)

percentTorque = rawTorque * 100

If percentTorque < 3.0 Then 'if the torque on joint 3 (z-axis) is less than 1% then

Print percentTorque, "% of total Torque"

P103 = P103 - Z(0.5) 'move joint 3 down 100 microns

Go P103

```
Else

Print "Torque before pickup: ", percentTorque, "% of total Torque"

Exit Do 'else exit loop

EndIf

Loop

Wait (3)

P104 = CurPos

Speed 1

For n = 1 To 30

P104 = P104 + Z(.1)

Go P104

Next

Speed 90

Fend
```

#define ZHeight2 -67.317 'Z position of Tool 4 with stamp on to be right above glass

Function Alkanethiolbath

'This program jumps to the alkanethiol or deposition material dish

Real area, x, y, z, u, n 'define variables

Real x1, x2, x3, x4, y1, y2, y3, y4, theta, theta2

Power Low 'set motor power to Low

Tool 2

Jump ethanolbath

TMove XY(0, 0, -0.5, 0)

P101 = CurPos

'Move the stamp in the ethanol bath small increments to ensure proper coating

For n = 0 To 8P101 = P101 + Y(1)

Go P101

P101 = P101 - Y(2)

Go P101

P101 = P101 + Y(1)

Next

Wait (3)

P101 = P101 + Z(10)

Go P101

Speed 100

For n = 0 To 5

P101 = P101 - Y(1)

Go P101

P101 = P101 + Y(2)

Go P101

P101 = P101 - Y(1)

Go P101

P101 = P101 +Z(2)

Go P101

P101 = P101 -Z(4)

Go P101

P101 = P101 +Z(2)

Go P101

Next

Speed 40

Fend

#define ZHeight2 -52 'Z position of Tool 4 with stamp on to be right above glass

Function calcsmallloc

'This program is used to find the center and orientation of the small glass on small chuck

'It images the corner of the slide and locates the corner point

Boolean found, CalcGlass

Real glassX, glassY, glassU, r

Real robX, robY, robU

Real x1, x2, x3, x4, y1, y2, y3, y4, u

Real x, y, theta, theta2, offX, offY

Integer i

Tool 3

Jump smallglasscam

```
CalcGlass = False
```

On 10

Wait 1

VRun locatesmall

VGet locatesmall.Point01.Found, found

VGet locatesmall.Point01.RobotX, x1

VGet locatesmall.Point01.RobotY, y1

VGet locatesmall.Line01.RobotU, u

If found = True Then

$$trGlassPos = XY(x1, y1, 0, u)$$

P200 = XY(x1, y1, ZHeight2, u) / 0

Local 1, P200

'P201, P202 and P203 are the corners of the pallet

'P201, P202 and P203 are defined in the Local 1 coordinate system

'pallet is 3x3, which means position 5 will be the center

$$P201 = XY(0, 0, 0, 0) / 1$$

P202 = XY(18, 0, 0, 0) / 1

P203 = XY(0, -18, 0, 0) / 1

Pallet 1, P201, P202, P203, 3, 3

Print "Center Glass Position: ", Pallet(1, 5)

Else

```
Print "Glass was not found!"
```

Exit Function

```
EndIf
```

```
Off (10)
```

SavePoints "Points.pts"

Tool 4

```
Jump Pallet(1, 5)
```

```
Pallet 2, trGlassPos, tlGlassPos, blGlassPos, brGlassPos, 59, 59
```

,

```
theta = RadToDeg(Atan2(x2 - x1, y2 - y1))
```

' Print "theta = ", theta

Pallet2center = Pallet(2, 1741)

' If (theta - 180) < -300 Then

theta
$$2 = theta + 180$$

Else

theta 2 = theta - 180

' EndIf

CU(pallet2center) = theta2

' CZ(pallet2center) = ZHeight2

' If stamp = 2 Then

pallet2center = pallet2center + XY(-0.6, -0.6, 0, 0)

' EndIf

,

```
Print "Glass Center Coord: ", pallet2center
' CalcGlass = True
Fend
Function CalcStampLoc
'This program locates the center of the stamp and its orientation
'finds 2 opposite corner features and calculates center point and theta
 Boolean found, CalcStamp, found1, found2
 Real r
 Real robX, robY, robU
 Real x, y, theta
 Real toolX1, toolY1, toolU
 Real toolX2, toolY2
 Real x1, y1, x2, y2, u
 Tool 2
 CalcStamp = False
       Jump stampFLcam
       Tool 0
       robX = CX(Here)
       robY = CY(Here)
       robU = CU(Here)
```

On 11

Wait 1

VRun locatestamp

VGet locatestamp.Geom01.Found, found

VGet locatestamp.Geom01.RobotX, x1

VGet locatestamp.Geom01.RobotY, y1

If found = True Then

x = x1 - robX

y = y1 - robY

theta = Atan2(x, y) - DegToRad(robU)

r = Sqr(x ** 2 + y ** 2)

toolX1 = Cos(theta) * r

toolY1 = Sin(theta) * r

Else 'target not found

Exit Function

EndIf

Tool 2

Jump stampBRcam

Tool 0

robX = CX(Here)

robY = CY(Here)

robU = CU(Here)

VRun locatestamp2

```
VGet locatestamp2.Geom01.Found, found
       VGet locatestamp2.Geom01.RobotX, x2
       VGet locatestamp2.Geom01.RobotY, y2
       If found = True Then
  x = x2 - robX
  y = y2 - robY
  theta = Atan2(x, y) - DegToRad(robU)
  r = Sqr(x ** 2 + y ** 2)
  toolX2 = Cos(theta) * r
  toolY2 = Sin(theta) * r
 Else 'target not found
  Exit Function
EndIf
x = (toolX1 + toolX2)/2
y = (toolY1 + toolY2)/2
 theta = Atan2(toolX1 - toolX2, toolY1 - toolY2)
toolU = RadToDeg(theta) - 45
TLSet 4, XY(x, y, 0, toolU)
 CalcStamp = True
Print "Stamp Center", x, y, toolU
Off (11)
Fend
```

```
Function calcwillowloc
```

'This program is similar to calcsmallloc but for large willow glass

Boolean found, CalcGlass

Real glassX, glassY, glassU, r

Real robX, robY, robU

Real x1, x2, x3, x4, y1, y2, y3, y4, u

Real x, y, theta, theta2, offX, offY

Integer i

Tool 3

Jump calcwillowFR

CalcGlass = False

On 10

Wait 1

VRun locatewillow

VGet locatewillow.Point01.Found, found

VGet locatewillow.Point01.RobotX, x1

VGet locatewillow.Point01.RobotY, y1

VGet locatewillow.Line02.RobotU, u

If found = True Then

$$P350 = XY(x1, y1, 0, u)$$

P300 = XY(x1, y1, ZHeight2, u) / 0

Local 2, P300

```
'P301, P302 and P303 are defined in the Local 2 coordinate system
                'pallet is 3x3, which means position 5 will be the center
                P301 = XY(0, 0, 0, 0) / 2
                P302 = XY(116, 0, 0, 0) / 2
                P303 = XY(0, 77, 0, 0) / 2
                Pallet 2, P301, P302, P303, 3, 3
                Print "Center Glass Position: ", Pallet(2, 5)
                Else
                        Print "Glass was not found!"
                        Exit Function
        EndIf
Off (10)
SavePoints "Points.pts"
Tool 4
        Jump Pallet(1, 5)
        Pallet 2, trGlassPos, tlGlassPos, blGlassPos, brGlassPos, 59, 59
        theta = RadToDeg(Atan2(x2 - x1, y2 - y1))
        Print "theta = ", theta
```

'P301, P302 and P303 are the corners of the pallet

```
Pallet2center = Pallet(2, 1741)
        If (\text{theta} - 180) < -300 \text{ Then}
                theta2 = theta + 180
                Else
                         theta2 = theta - 180
        EndIf
        CU(pallet2center) = theta2
        CZ(pallet2center) = ZHeight2
        If stamp = 2 Then
                pallet2center = pallet2center + XY(-0.6, -0.6, 0, 0)
        EndIf
        Print "Glass Center Coord: ", pallet2center
' CalcGlass = True
Fend
```

#define ZHeight2 -67.317 'Z position of Tool 4 with stamp on to be right above glass

Function CalibrateHardStops

'This program is used to calibrate the hard stops on the stamp backing plate

'First run pick up stamp, then ensure the ink pad is in proper location

'Run this program as many times as needed before drop stamp

Real area, x, y, z, u, n 'define variables

Real x1, x2, x3, x4, y1, y2, y3, y4, theta, theta2, stamp

Integer answer, count

Boolean found, found1, found2, found3, offset

Power Low 'set motor power to Low

Tool 2

offset = False 'True = 600 um offset from center in x and y, false = no offset

Real XoffsetS2, YoffsetS2, UoffsetS2, XoffsetS3, YoffsetS3, UoffsetS3

XoffsetS2 = 0.02498 '0.026956667 '0.021511 '0.032714167 '0.020727167 '0.029006 '0.01776

YoffsetS2 = 0.05379 '0.058226667 '0.049976 '0.0566977 '0.0454777 '0.031376 '0.02616

UoffsetS2 = -0.18 '-0.16 '-0.146 '-0.16798 '-0.12398 '-0.166 '-0.17

XoffsetS3 = 0 '-0.002263333 '0.014846 '0.011401667 '0.002775667 '0.005307 '0.01273

YoffsetS3 = 0 '0.077636667 '0.079189 '0.082369533 '0.078763533 '0.074173 '0.07092

UoffsetS3 = 0 '0.0033333333 '-0.028 '0.013486047 '0.017486047 '0.016 '0.02

Jump inkstamp

P104 = inkstamp

Tool 2

Jump calstamploc

P103 = CurPos 'set a temporary point that will change with torque measurements

```
Do 'enter loop
       ATCLR
       Wait (2) 'wait 2 seconds before torque measurement
       Real rawTorque, percentTorque
       rawTorque = ATRQ(3)
       percentTorque = rawTorque * 100
       If percentTorque < 3.0 Then 'if the torque on joint 3 (z-axis) is less than 1% then
               Print percentTorque, "% of total Torque"
               P103 = P103 - Z(0.5) 'move joint 3 down 100 microns
               Go P103
       Else
               Print "Torque before pickup: ", percentTorque, "% of total Torque"
               Exit Do 'else exit loop
       EndIf
Loop
Wait (3)
P104 = CurPos
Speed 1
For n = 1 To 30
       P104 = P104 + Z(.1)
```

Go P104

Next

Speed 90

Jump safept

Fend

Function centeredwillowstamp

'This program calls sub programs to pattern in the center of the willow glass

Call SpringStampPickup_A

Call CalcStampLoc

Call calcwillowloc

Call Alkanethiolbath

Call nitrostream

Tool 4

Jump Pallet(2, 5)

Call stampingtorque

Call DropStamp

Fend

#define ZHeight2 -67.317 'Z position of Tool 4 with stamp on to be right above glass

Function DropStamp

'This program drops the stamp in the stamp nesting fixture

Real area, x, y, z, u, n 'define variables

Real x1, x2, x3, x4, y1, y2, y3, y4, theta, theta2, stamp

Integer answer, count

Boolean found, found1, found2, found3, offset

Power Low 'set motor power to Low

Tool 2

Jump stamppickup

Off (8)

Jump safept

Fend

#define ZHeight2 -67.317 'Z position of Tool 4 with stamp on to be right above glass

Function nitrostream

'This program carries the stamp after the alkane thiol bath to dry under nitrogen stream

Real area, x, y, z, u, n 'define variables

Real x1, x2, x3, x4, y1, y2, y3, y4, theta, theta2

Integer answer, count

Power Low 'set motor power to Low

Tool 2

Jump n2stream

P102 = n2stream

On (9)

Power High

"The robot moves in a "zig-zag" pattern over the Nitrogen streams at a slow speed to evaporate the ethanol on it

```
Speed 1
```

CP On

For n = 1 To 7

P102 = P102 + X(30) + Y(30)

Go P102

P102 = P102 - X(60)

Go P102

P102 = P102 - Y(15)

Go P102

P102 = P102 + X(60)

Go P102

P102 = P102 - Y(15)

Go P102

P102 = P102 - X(60)

Go P102

P102 = P102 - Y(15)

Go P102

P102 = P102 + X(60)

Go P102

P102 = P102 - Y(15)

Go P102

P102 = P102 - X(60)

Go P102

P102 = P102 + Y(30) + X(30)

Go P102
Print n
Next
CP Off
Speed 40
Off (9)
Power Low
Fend
'This is the GUI details Will change as buttons are added or removed
Function RucpGUI_Pickup_Click(Sender\$ As String)
Xqt SpringStampPickup_A
Fend
Function RucpGUI_Calibrate_Click(Sender\$ As String)
Xqt CalibrateHardStops
Fend
Function RucpGUI_Drop_Click(Sender\$ As String)
Xqt DropStamp
Fend
Function RucpGUI_phigh_Click(Sender\$ As String)
Power High
Fend

Function RucpGUI_plow_Click(Sender\$ As String)
Power Low
Fend
Function RucpGUI_pon_Click(Sender\$ As String)
Motor On
Fend
Function RucpGUI_poff_Click(Sender\$ As String)
Motor Off
Fend
Function RucpGUI_stop_Click(Sender\$ As String)
Pause
Fend
Function RucpGUI_continue_Click(Sender\$ As String)
Cont
Fend
Function RucpGUI_smallarbitrary_Click(Sender\$ As String)
Xqt smallbasic
Fend

Function RucpGUI_smallcenteredpt_Click(Sender\$ As String)

Xqt smallcenteredstamp

Fend

Function RucpGUI_smallwillowstamp_Click(Sender\$ As String)

Xqt centeredwillowstamp

Fend

Function smallbasic

Call SpringStampPickup_A

Call Alkanethiolbath

Call nitrostream

Call arbitraryloc

Call DropStamp

Fend

#define ZHeight2 -67.317 'Z position of Tool 4 with stamp on to be right above glass

Function SecondCamStamp(stampNumber As Real)

'This is a legacy program, it is largely useless except for pulling old code

Print "Stamp number = ", stampNumber

Real area, x, y, z, u, n 'define variables

Real x1, x2, x3, x4, y1, y2, y3, y4, theta, theta2, stamp

Integer answer, count

Boolean found, found1, found2, found3, offset

```
Power Low 'set motor power to Low
Tool 4
offset = False 'True = 600 um offset from center in x and y, false = no offset
Real XoffsetS2, YoffsetS2, UoffsetS2, XoffsetS3, YoffsetS3, UoffsetS3
XoffsetS2 = 0.02498 '0.026956667 '0.021511 '0.032714167 '0.020727167 '0.029006 '0.01776
YoffsetS2 = 0.05379 '0.058226667 '0.049976 '0.0566977 '0.0454777 '0.031376 '0.02616
UoffsetS2 = -0.18 '-0.16 '-0.146 '-0.16798 '-0.12398 '-0.166 '-0.17
XoffsetS3 = 0 '-0.002263333 '0.014846 '0.011401667 '0.002775667 '0.005307 '0.01273
YoffsetS3 = 0 '0.077636667 '0.079189 '0.082369533 '0.078763533 '0.074173 '0.07092
UoffsetS3 = 0 '0.0033333333 '-0.028 '0.013486047 '0.017486047 '0.016 '0.02
'Jump Stamp1TR
On 11
VRun UC1TRStamp
VGet UC1TRStamp.Corr01.Found, found1
VGet UC1TRStamp.Corr02.Found, found2
VGet UC1TRStamp.Corr03.Found, found3
If found1 = True And found2 = False And found3 = False Then
       stamp = 1
```

```
ElseIf found1 = False And found2 = True And found3 = False Then
       stamp = 2
ElseIf found1 = False And found2 = False And found3 = True Then
       stamp = 3
Else
       Jump Stamp2TR
       VRun UC1TRStamp
       VGet UC1TRStamp.Corr01.Found, found1
       VGet UC1TRStamp.Corr02.Found, found2
       VGet UC1TRStamp.Corr03.Found, found3
       If found1 = True And found2 = False And found3 = False Then
              stamp = 1
       ElseIf found1 = False And found2 = True And found3 = False Then
              stamp = 2
       ElseIf found1 = False And found2 = False And found3 = True Then
              stamp = 3
       Else
              Jump Stamp3TR
              VRun UC1TRStamp
              VGet UC1TRStamp.Corr01.Found, found1
              VGet UC1TRStamp.Corr02.Found, found2
              VGet UC1TRStamp.Corr03.Found, found3
```

```
If found1 = True And found2 = False And found3 = False Then
                      stamp = 1
               ElseIf found1 = False And found2 = True And found3 = False Then
                      stamp = 2
               ElseIf found1 = False And found2 = False And found3 = True Then
                      stamp = 3
               Else
                      Print "cannot determine stamp!"
                      Exit Function
               EndIf
       EndIf
EndIf
Off 11
Print "Stamp = ", stamp
Tool 4
Jump glasscenter
x = 0
y = 0
u = 0
On 10
For n = 1 To 10
```

```
Print n
       Call CalcGlassPos(stamp, stampNumber, offset)
       x = x + CX(pallet2center)
       y = y + CY(pallet2center)
       u = u + CU(pallet2center)
Next
Off 10
x = x / 10
y = y / 10
u = u / 10
CX(pallet2center) = x
CY(pallet2center) = y
CU(pallet2center) = u
Print "Averaged Center Glass Location: ", pallet2center
Tool 4
Jump Stamp1TR
x = 0
y = 0
u = 0
```

```
On 11
For n = 1 To 10
        Print n
        Call CalcStampLoc(stamp)
        x = x + CX(Tool5Offset)
        y = y + CY(Tool5Offset)
        u = u + CU(Tool5Offset)
Next
Off 11
x = x / 10
y = y / 10
u = u / 10
Tool5Offset = XY(x, y, 0, u)
Print "Average Stamp Offset: ", Tool5Offset
TLSet 5, XY(x, y, 0, u)
Tool 5
'(comment below - Jasons)
If stamp = 2 Then
       pallet2center = pallet2center + XY(XoffsetS2, YoffsetS2, 0, UoffsetS2)
ElseIf stamp = 3 Then
        pallet2center = pallet2center + XY(XoffsetS3, YoffsetS3, 0, UoffsetS3)
EndIf
```

```
Jump pallet2center
Jump StampCentered
P103 = CurPos 'set a temporary point that will change with torque measurements
Do 'enter loop
       ATCLR
       Wait (2) 'wait 2 seconds before torque measurement
       Real rawTorque, percentTorque
       rawTorque = ATRQ(3)
       percentTorque = rawTorque * 100
       If percentTorque < 3.0 Then 'if the torque on joint 3 (z-axis) is less than 1% then
               Print percentTorque, "% of total Torque"
               P103 = P103 - Z(0.5) 'move joint 3 down 100 microns
               Go P103
       Else
               Print "Torque before pickup: ", percentTorque, "% of total Torque"
               Exit Do 'else exit loop
       EndIf
Loop
Wait (3)
P104 = CurPos
```

```
Speed 1
       For n = 1 To 30
               P104 = P104 + Z(.1)
               Go P104
       Next
       Speed 90
       Tool 4
       Jump stampPickUp
       Off (8)
       Jump safept
Fend
Function smallcenteredstamp
       Call SpringStampPickup_A
       Call CalcStampLoc
       Call calcsmallloc
       Call Alkanethiolbath
       Call nitrostream
       Tool 4
       Jump Pallet(1, 5)
       Call stampingtorque
```

Call DropStamp

#define ZHeight2 -67.317 'Z position of Tool 2 with stamp on to be right above glass

Function SpringStampPickup_A

'This program is used for picking up the stamps in a repeatable fashion

Real area, x, y, z, u, n 'define variables

Real x1, x2, x3, x4, y1, y2, y3, y4, theta, theta2, stamp

Integer answer, count

Boolean found, found1, found2, found3

Power Low 'set motor power to Low

Jump safept 'jump to defined safe point

Tool 2

Jump stamppickup

'The following commented section is used if Torque limited pickup is desired

- P100 = CurPos 'set a temporary point that will change with torque measurements
- Do 'enter loop
- ATCLR
- ' Wait (2) 'wait 3 seconds before torque measurement
- ' Real rawTorque, percentTorque
- ' rawTorque = ATRQ(3)

```
percentTorque = rawTorque * 100
               If percentTorque < 1 Then '-0.03 if the torque on joint 3 (z-axis) is greater than zero
then
                       Print percentTorque, "% of total Torque"
                       P100 = P100 - Z(0.1) 'move joint 3 down 100 microns
                       Go P100
               Else
                       Print "Torque before pickup: ", percentTorque, "% of total Torque"
                       Exit Do 'else exit loop
               EndIf
       Loop
       On (8) 'turn on suction cup
       Jump Safept
Fend
```

Function stampingtorque

'This program is used for beginning the torque limiting loop

'You can call this program after the stamp is 1mm or less above the desired substrate

'This will limit the torque based on the % below

P103 = CurPos 'set a temporary point that will change with torque measurements

Do 'enter loop

```
ATCLR
       Wait (2) 'wait 2 seconds before torque measurement
       Real rawTorque, percentTorque
       Integer n
       rawTorque = ATRQ(3)
       percentTorque = rawTorque * 100
       If percentTorque < 3.0 Then 'if the torque on joint 3 (z-axis) is less than 1% then
               Print percentTorque, "% of total Torque"
               P103 = P103 - Z(0.5) 'move joint 3 down 100 microns
               Go P103
       Else
               Print "Torque before pickup: ", percentTorque, "% of total Torque"
               Exit Do 'else exit loop
       EndIf
Wait (3)
P104 = CurPos
Speed 1
For n = 1 To 30
       P104 = P104 + Z(.1)
       Go P104
```

Loop

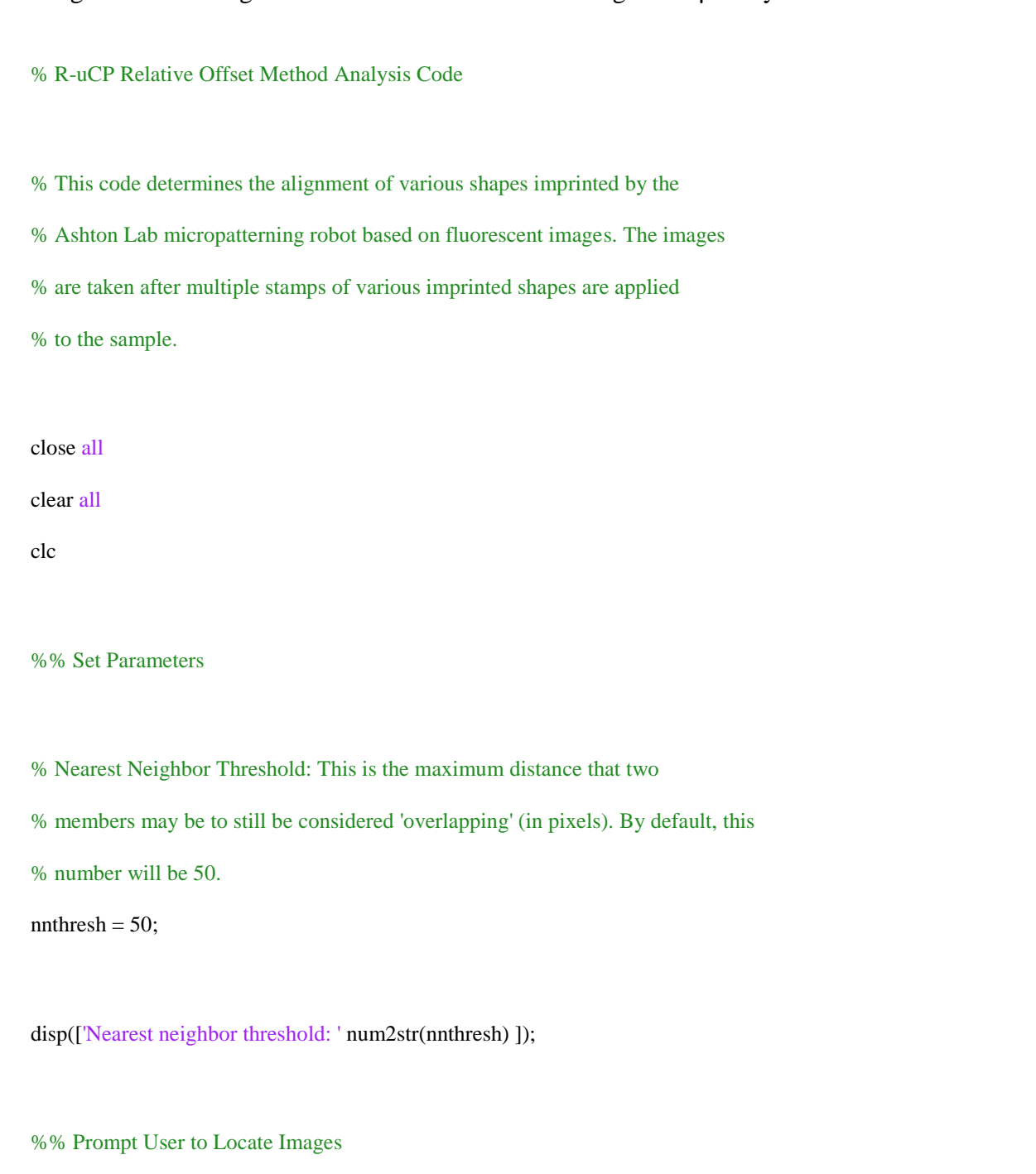
Next

Speed 90

Fend

Appendix V – MATLAB Code for Chapter 3

Below is the custom MATLAB code and user guide for analyzing the fluorescent images created using the relative offset method utilizing the $R-\mu CP$ system.



```
disp(['Locate images'])
[FileName,PathName] = uigetfile('*.tif','Select an Image Containing Sarcomere Structures','C:\Users\Jason
McNulty\Desktop','Multiselect','off');
res = get(0, 'ScreenSize');
horres = res(3);
vertres=res(4);
%% Get Image Data Ready, and Normalize
global imagedataorig
 imagedata = imread([PathName FileName]);
 imagedata = imagedata(:,:,1);
 imsize = size(imagedata);
imagemax = double(max(max(imagedata)));
imagecorrect= double(255/imagemax);
imagedata=imagedata*imagecorrect;
imagedataorig = imagedata;
imagedatamod = imagedata;
rois = zeros(size(imagedata));
%% Set Scale
```

sprintf(['Ashton Lab Robot Alignment Tool, Max Salick 6-11-2013', ...

```
'\n-----', ...
 '\n\nScale must be set...', ...
 '\n 1 - Use scalebar in image to calibrate', ...
 '\n 2 - Direct input of pixel/um ratio', ...
 '\n 3 - Set no scale (arbitrary scale will be set)'])
scalemode = input('Select Option: ');
if scalemode ==1
   colormap('gray')
 imagesc(imagedataorig);
 colormap('gray')
  [scalepointx,scalepointy] = ginput(2);
  close all
  scaleinput = input('Input the known distance between points: ');
  pixeldist = ((scalepointx(1)-scalepointx(2))^2 + (scalepointy(1)-scalepointy(2))^2)^5;
  umperpix = scaleinput/pixeldist;
  disp(['Selected scale is ' num2str(umperpix) ' microns per pixel'])
elseif scalemode==2
 umperpix = input('Input known microns-per-pixel: ');
elseif scalemode==3
 sprintf(['Setting arbitrary calibration of 1 micron per pixel'])
 umperpix = 1;
else
 sprintf(['Whoops?']);
 stop
end
```

```
%% ROI Selections
global popnames
global population_totalnum
global popims
global roimarked
disp(' ')
disp('.....')
disp(' ')
disp('Each shape type will be defined as a population.')
population_totalnum = input('Please indicate the total number of populations: ');
disp(' ')
for k=1:population_totalnum
popnames{k} = ['Population ' num2str(k)];
popims{k} = logical(0.*imagedataorig);
end
roimarked = zeros(size(imagedataorig));
disp('Starting pattern selection interface...')
[varargout] = patternfind2(imagedataorig,popnames,popims)
uiwait(patternfind2)
%% Prompt User for Predicted Population Offset
```

```
disp(' ');
disp('Population selection completed!');
disp(' ');
disp('Starting coordinate detection and matching module...')
disp(' ')
disp('Please input the designed offset for each population in comparison to Population 1.');
for k=2:population_totalnum
 offsetx{k} = input(['Population ' num2str(k) ' X offset (um): ']);
 offsetx{k} = offsetx{k}/umperpix;
 offsety{k} = input(['Population ' num2str(k) ' Y offset (um): ']);
offsety{k} = offsety{k}/umperpix;
end
offsetx\{1\} = 0;
offsety\{1\} = 0;
disp(' ');
disp(Patterns selected and defined; determining coordinates and performing nearest-neighbor computations...')
```

```
figure
hold on
%% Convert ROI Data to Population Coordinates
\quad \quad \text{for } k=1\text{:population\_totalnum}
disp(['Finding centroid coordinates of population ' num2str(k) '...'])
currentrois = popims{k}.*roimarked;
 roiprops = regionprops(currentrois);
regprops = regionprops(currentrois);
arealist = [regprops.Area];
idx = find(arealist > 1);
posareas = arealist(idx);
centlist = [regprops.Centroid];
 xlocs = centlist(2.*idx-1);
ylocs = centlist(2.*idx);
coords = [xlocs' ylocs'];
coords(:,2) = imsize(1) - coords(:,2);
 coordsave\{k\} = coords;
 scatter(coordsave\{k\}(:,1),coordsave\{k\}(:,2));
```

```
pause(.000001);
     coordsave\{k\} = [coords(:,1)-offsetx\{k\} \ coords(:,2)-offsety\{k\}];
     saveareas{k} = posareas;
end
%% Run Nearest-Neighbor Analysis to Produce Valid Coordinate Arrays
title('All-Population Scatterplot')
hold off
clear coordvalid
clear allmins
clear dists
clear xmiss
clear ymiss
clear xmissave
clear ymissave
for k=2:population_totalnum
     countup = 1;
     for vi = 1:max(size(coordsave{k}))
             dists \ \{k\}(vi,:) = ((coordsave\{k\}(vi,1)-coordsave\{1\}(:,1)).^2 + (coordsave\{k\}(vi,2)-coordsave\{k\}(vi,2)-coordsave\{k\}(vi,2)-coordsave\{k\}(vi,2)-coordsave\{k\}(vi,2)-coordsave\{k\}(vi,2)-coordsave\{k\}(vi,2)-coordsave\{k\}(vi,2)-coordsave\{k\}(vi,2)-coordsave\{k\}(vi,2)-coordsave\{k\}(vi,2)-coordsave\{k\}(vi,2)-coordsave\{k\}(vi,2)-coordsave\{k\}(vi,2)-coordsave\{k\}(vi,2)-coordsave\{k\}(vi,2)-coordsave\{k\}(vi,2)-coordsave\{k\}(vi,2)-coordsave\{k\}(vi,2)-coordsave\{k\}(vi,2)-coordsave\{k\}(vi,2)-coordsave\{k\}(vi,2)-coordsave\{k\}(vi,2)-coordsave\{k\}(vi,2)-coordsave\{k\}(vi,2)-coordsave\{k\}(vi,2)-coordsave\{k\}(vi,2)-coordsave\{k\}(vi,2)-coordsave\{k\}(vi,2)-coordsave\{k\}(vi,2)-coordsave\{k\}(vi,2)-coordsave\{k\}(vi,2)-coordsave\{k\}(vi,2)-coordsave\{k\}(vi,2)-coordsave\{k\}(vi,2)-coordsave\{k\}(vi,2)-coordsave\{k\}(vi,2)-coordsave\{k\}(vi,2)-coordsave\{k\}(vi,2)-coordsave\{k\}(vi,2)-coordsave\{k\}(vi,2)-coordsave\{k\}(vi,2)-coordsave\{k\}(vi,2)-coordsave\{k\}(vi,2)-coordsave\{k\}(vi,2)-coordsave\{k\}(vi,2)-coordsave\{k\}(vi,2)-coordsave\{k\}(vi,2)-coordsave\{k\}(vi,2)-coordsave\{k\}(vi,2)-coordsave\{k\}(vi,2)-coordsave\{k\}(vi,2)-coordsave\{k\}(vi,2)-coordsave\{k\}(vi,2)-coordsave\{k\}(vi,2)-coordsave\{k\}(vi,2)-coordsave\{k\}(vi,2)-coordsave\{k\}(vi,2)-coordsave\{k\}(vi,2)-coordsave\{k\}(vi,2)-coordsave\{k\}(vi,2)-coordsave\{k\}(vi,2)-coordsave\{k\}(vi,2)-coordsave\{k\}(vi,2)-coordsave\{k\}(vi,2)-coordsave\{k\}(vi,2)-coordsave\{k\}(vi,2)-coordsave\{k\}(vi,2)-coordsave\{k\}(vi,2)-coordsave\{k\}(vi,2)-coordsave\{k\}(vi,2)-coordsave\{k\}(vi,2)-coordsave\{k\}(vi,2)-coordsave\{k\}(vi,2)-coordsave\{k\}(vi,2)-coordsave\{k\}(vi,2)-coordsave\{k\}(vi,2)-coordsave\{k\}(vi,2)-coordsave\{k\}(vi,2)-coordsave\{k\}(vi,2)-coordsave\{k\}(vi,2)-coordsave\{k\}(vi,2)-coordsave\{k\}(vi,2)-coordsave\{k\}(vi,2)-coordsave\{k\}(vi,2)-coordsave\{k\}(vi,2)-coordsave\{k\}(vi,2)-coordsave\{k\}(vi,2)-coordsave\{k\}(vi,2)-coordsave\{k\}(vi,2)-coordsave\{k\}(vi,2)-coordsave\{k\}(vi,2)-coordsave\{k\}(vi,2)-coordsave\{k\}(vi,2)-coordsave\{k\}(vi,2)-coordsave\{k\}(vi,2)-coordsave\{k\}(vi,2)-coordsave\{k\}(vi,2)-coordsave\{k\}(vi,2)-coordsave\{k\}(vi,2)-coordsave\{k\}(vi,2)-coordsave\{k\}(vi,2)-coordsave\{k\}(vi,2)-coordsave\{k\}(vi,2)-co
coordsave{1}(:,2)).^2).^.5;
```

```
[mindist,bestpop1] = min(dists\{k\}(vi,:));
  if mindist <= nnthresh</pre>
%
      mindist
   xmiss\{k\}(vi) = coordsave\{k\}(vi,1)-coordsave\{1\}(bestpop1,1);
   ymiss\{k\}(vi) = coordsave\{k\}(vi,2)-coordsave\{1\}(bestpop1,2);
   coordvalid\{k\}(countup,1) = coordsave\{k\}(vi,1);
   coordvalid\{k\}(countup,2) = coordsave\{k\}(vi,2);
   coordvalid\{k\}(countup,3) = coordsave\{1\}(bestpop1,1);
   coordvalid{k}(countup,4) = coordsave{1}(bestpop1,2);
   countup = countup+1;
  end
  allmins\{k\}(vi) = mindist;
end
end
%% Find Hatchmark Center via GUI
disp(' ')
disp('Population coordinates determined.')
```

```
disp('Now the global center must be determined to indicate axis of rotation.');
disp(' ')
disp('Zoom is currently enabled. Please locate the hatchmarks and set the')
disp('zoom so that all hatchmarks are clearly framed withing the figure.')
disp(' ')
disp('When finished, press ENTER to begin point selection.')
disp(' ')
% figure
% imagesc(imagedataorig);
% colormap(gray)
% [hatch_x, hatch_y] = ginput(4);
%
imagesc(imagedataorig);
colormap(gray)
zoom on; % use mouse button to zoom in or out
% Press Enter to get out of the zoom mode.
% CurrentCharacter contains the most recent key which was pressed after opening
% the figure, wait for the most recent key to become the return/enter key
waitfor(gcf,'CurrentCharacter',13)
zoom reset
zoom off
```

```
disp('Please select the hatchmarks visible on the sample to determine this center.');
disp(' ')
disp('Select the hatchmarks in the FOLLOWING ORDER:')
disp(' ')
disp(' 1----2');
disp(' | |');
disp(' | |');
disp(' | |');
disp(' 3----4');
disp(' ')
[hatch_x, hatch_y] = ginput(4);
globalcent_x = mean(hatch_x);
globalcent_y = mean(hatch_y);
%
% xmissave{k} = mean(coordvalid{k}(:,1)-coordvalid{k}(:,3));
% ymissave\{k\} = (mean(coordvalid\{k\}(:,2)-coordvalid\{k\}(:,4)));
%
% figure
%
 \% \ quiver(coordvalid\{k\}(:,1),coordvalid\{k\}(:,2),coordvalid\{k\}(:,1)-coordvalid\{k\}(:,3),coordvalid\{k\}(:,2)-coordvalid\{k\}(:,3),coordvalid\{k\}(:,3),coordvalid\{k\}(:,3),coordvalid\{k\}(:,3),coordvalid\{k\}(:,3),coordvalid\{k\}(:,3),coordvalid\{k\}(:,3),coordvalid\{k\}(:,3),coordvalid\{k\}(:,3),coordvalid\{k\}(:,3),coordvalid\{k\}(:,3),coordvalid\{k\}(:,3),coordvalid\{k\}(:,3),coordvalid\{k\}(:,3),coordvalid\{k\}(:,3),coordvalid\{k\}(:,3),coordvalid\{k\}(:,3),coordvalid\{k\}(:,3),coordvalid\{k\}(:,3),coordvalid\{k\}(:,3),coordvalid\{k\}(:,3),coordvalid\{k\}(:,3),coordvalid\{k\}(:,3),coordvalid\{k\}(:,3),coordvalid\{k\}(:,3),coordvalid\{k\}(:,3),coordvalid\{k\}(:,3),coordvalid\{k\}(:,3),coordvalid\{k\}(:,3),coordvalid\{k\}(:,3),coordvalid\{k\}(:,3),coordvalid\{k\}(:,3),coordvalid\{k\}(:,3),coordvalid\{k\}(:,3),coordvalid\{k\}(:,3),coordvalid\{k\}(:,3),coordvalid\{k\}(:,3),coordvalid\{k\}(:,3),coordvalid\{k\}(:,3),coordvalid\{k\}(:,3),coordvalid\{k\}(:,3),coordvalid\{k\}(:,3),coordvalid\{k\}(:,3),coordvalid\{k\}(:,3),coordvalid\{k\}(:,3),coordvalid\{k\}(:,3),coordvalid\{k\}(:,3),coordvalid\{k\}(:,3),coordvalid\{k\}(:,3),coordvalid\{k\}(:,3),coordvalid\{k\}(:,3),coordvalid\{k\}(:,3),coordvalid\{k\}(:,3),coordvalid\{k\}(:,3),coordvalid\{k\}(:,3),coordvalid\{k\}(:,3),coordvalid\{k\}(:,3),coordvalid\{k\}(:,3),coordvalid\{k\}(:,3),coordvalid\{k\}(:,3),coordvalid\{k\}(:,3),coordvalid\{k\}(:,3),coordvalid\{k\}(:,3),coordvalid\{k\}(:,3),coordvalid\{k\}(:,3),coordvalid\{k\}(:,3),coordvalid\{k\}(:,3),coordvalid\{k\}(:,3),coordvalid\{k\}(:,3),coordvalid\{k\}(:,3),coordvalid\{k\}(:,3),coordvalid\{k\}(:,3),coordvalid\{k\}(:,3),coordvalid\{k\}(:,3),coordvalid\{k\}(:,3),coordvalid\{k\}(:,3),coordvalid\{k\}(:,3),coordvalid\{k\}(:,3),coordvalid\{k\}(:,3),coordvalid\{k\}(:,3),coordvalid\{k\}(:,3),coordvalid\{k\}(:,3),coordvalid\{k\}(:,3),coordvalid\{k\}(:,3),coordvalid\{k\}(:,3),coordvalid\{k\}(:,3),coordvalid\{k\}(:,3),coordvalid\{k\}(:,3),coordvalid\{k\}(:,3),coordvalid\{k\}(:,3),coordvalid\{k\}(:,3),coordvalid\{k\}(:,3),coordvalid\{k\}(:,3),coordvalid\{k\}(:,3),coordvalid\{k\}(:,3),coordvalid\{k\}(:,3),coordvalid\{k\}(:,3),coordvalid\{k\}(:,3),coordvalid\{k\}(:,3),coordvalid\{k\}(:,3),coordvalid\{k\}(:,3),coordvalid\{k\}(:,3)
coordvalid{k}(:,4));
% title(['Overall offset of Population 'num2str(k)]);
%
%
% disp(' ')
```

```
% disp(['Population 'num2str(k) 'displacement statistics:'])
% disp(['Average X offset: 'num2str(xmissave{k}*umperpix) 'um'])
% disp(['Average Y offset: 'num2str(ymissave{k}*umperpix) 'um'])
% disp(' ')
%
% relxoff\{k\} = coordvalid\{k\}(:,1)-coordvalid\{k\}(:,3)-xmissave\{k\};
% relyoff\{k\} = coordvalid\{k\}(:,2)-coordvalid\{k\}(:,4)-ymissave\{k\};
%
% overalloff{k} = (relxoff{k}.^2+relyoff{k}.^2).^5;
%
% figure
%
% quiver(coordvalid{k}(:,1),coordvalid{k}(:,2),relxoff{k},relyoff{k});
% title(['Relative offset of Population 'num2str(k)]);
%
for k = 2:population_totalnum
% Centering around global center....
ncoordvalid\{k\}(:,1) = coordvalid\{k\}(:,1) - globalcent\_x;
ncoordvalid\{k\}(:,3) = coordvalid\{k\}(:,3) - globalcent\_x;
ncoordvalid\{k\}(:,2) = coordvalid\{k\}(:,2) - globalcent_y;
ncoordvalid\{k\}(:,4) = coordvalid\{k\}(:,4) - globalcent_y;
[regParams,Bfit,ErrorStats]= ...
 absor([ncoordvalid{k}(:,1) ncoordvalid{k}(:,2)]', ...
 [ncoordvalid\{k\}(:,3) ncoordvalid\{k\}(:,4)]');
```

```
transposeinfo\{k\} = regParams;
absolve_xoff{k} = regParams.t(1)*-umperpix;
absolve_yoff{k} = regParams.t(2)*-umperpix;
absolve rot\{k\} = 360-regParams.theta;
fixedcoords\{k\} = (transposeinfo\{k\}.M*[ncoordvalid\{k\}(:,1) ncoordvalid\{k\}(:,2) ...
 ones(1,max(size(ncoordvalid{k}(:,1))))']')';
fixedcoords\{k\} = fixedcoords\{k\}(:,1:2);
origerror\{k\} = mean(abs(ncoordvalid\{k\}(:,4) - ncoordvalid\{k\}(:,2)) + ...
 (abs(ncoordvalid\{k\}(:,3) - ncoordvalid\{k\}(:,1))));
newerror(k) = mean(abs(ncoordvalid\{k\}(:,4) - fixedcoords\{k\}(:,2)) + ...
 (abs(ncoordvalid\{k\}(:,3) - fixedcoords\{k\}(:,1))));
end
disp(' ')
disp(' ')
disp(FileName)
disp('----')
disp('Suggested Corrections to Match Populations:')
for k=2:population_totalnum
 transangle\{k\} = transposeinfo\{k\}.theta;
 if transangle \{k\} > 180
   transangle\{k\} = transangle\{k\} - 360;
```

end

```
\label{lem:disp([Population 'num2str(k) 'should be rotated '... \\ num2str(transangle\{k\}) 'degrees (positive=CCW)']); \\ disp(['Population 'num2str(k) 'should be translated '... \\ num2str(transposeinfo\{k\}.t(1)*umperpix) 'um in the +X direction']); \\ disp(['Population 'num2str(k) 'should be translated '... \\ num2str(transposeinfo\{k\}.t(2)*umperpix) 'um in the +Y direction']); \\ disp('') \\ end \\ \end{tabular}
```

MATLAB Guide

Below is a guide for how to use the previously mentioned MATLAB code for analyzing the images created using the relative offset method with R-µCP. It should be mentioned that prior to loading the images into MATLAB, the first stamp population should be aligned such that the columns and rows are vertical and horizontal with the picture frame.

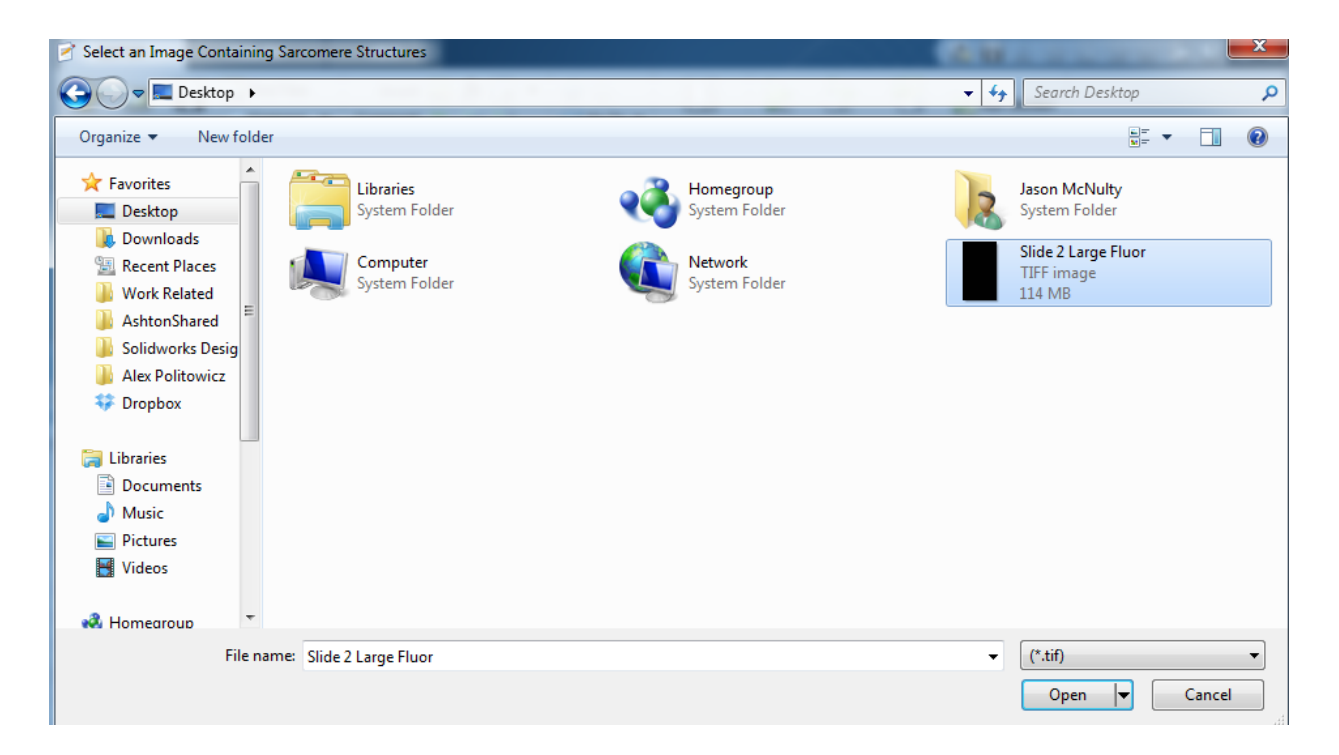
Once MATLAB is running, open AshtonRobotAlignV2

Select Run



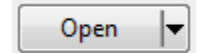
A.1 MATLAB run button image

Locate desired TIFF image



A. 2 Image selection window for locating TIFF

Select open



A. 3 Open button to load selected TIFF

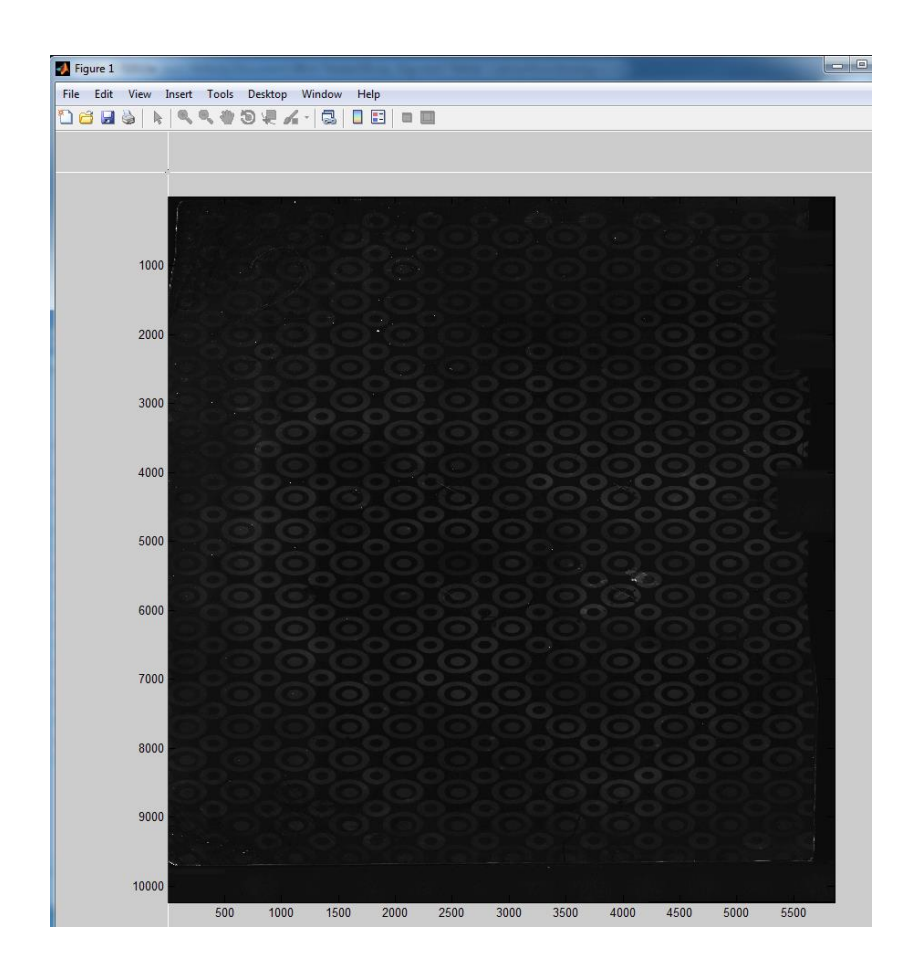
Select option for defining the scale bar:

```
Scale must be set...

1 - Use scalebar in image to calibrate
2 - Direct input of pixel/um ratio
3 - Set no scale (arbitrary scale will be set)

Select Option:
```

If the 1st option is selected, select 2 known points on GUI a set distance apart (to define scale)



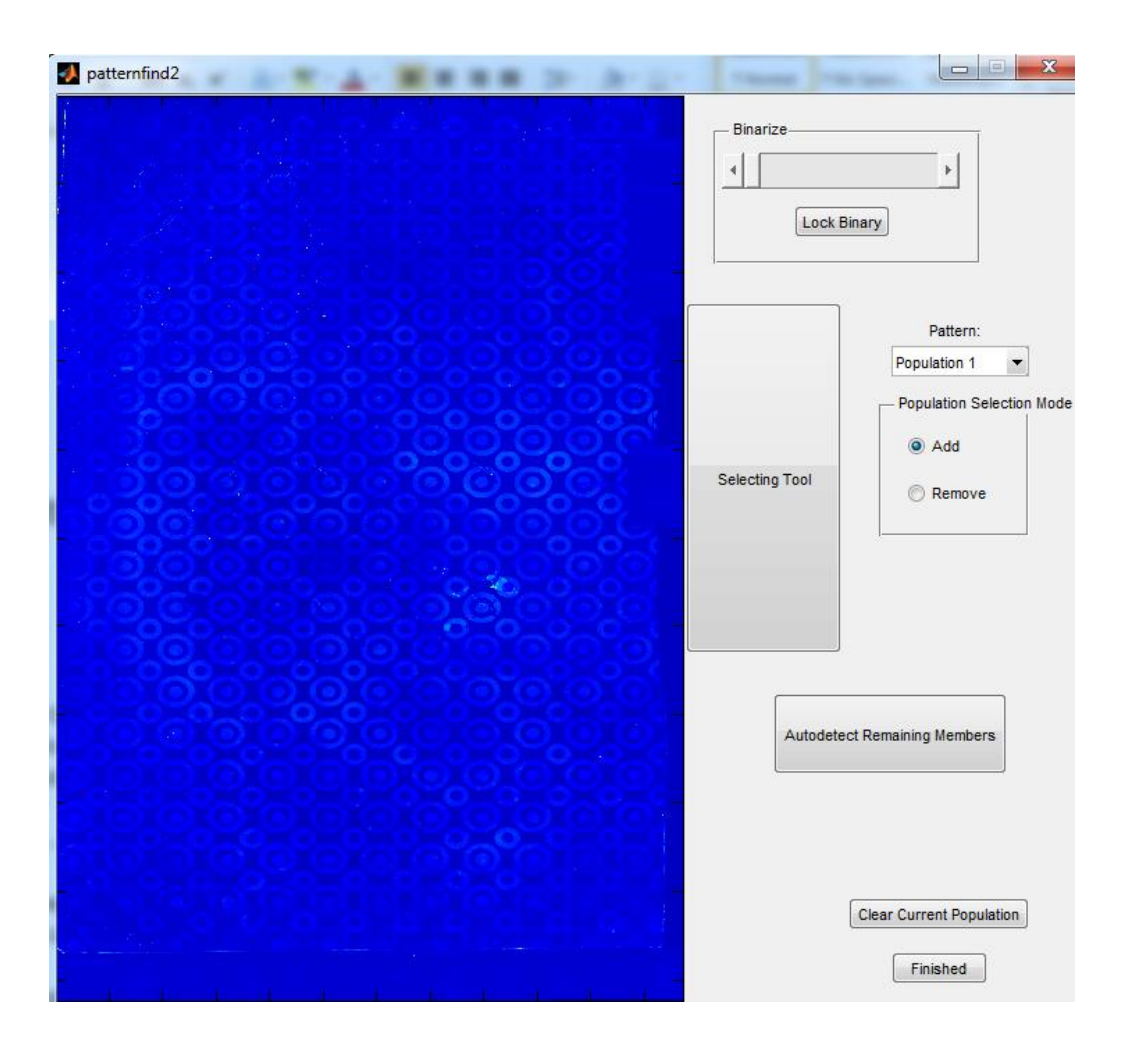
A. 4 Graphic user interface for determining image scale

Enter distance, ENTER, enter number of populations (stamps)

```
Select Option: 1
Input the known distance between points: 9600
Selected scale is 2.5243 microns per pixel
.....

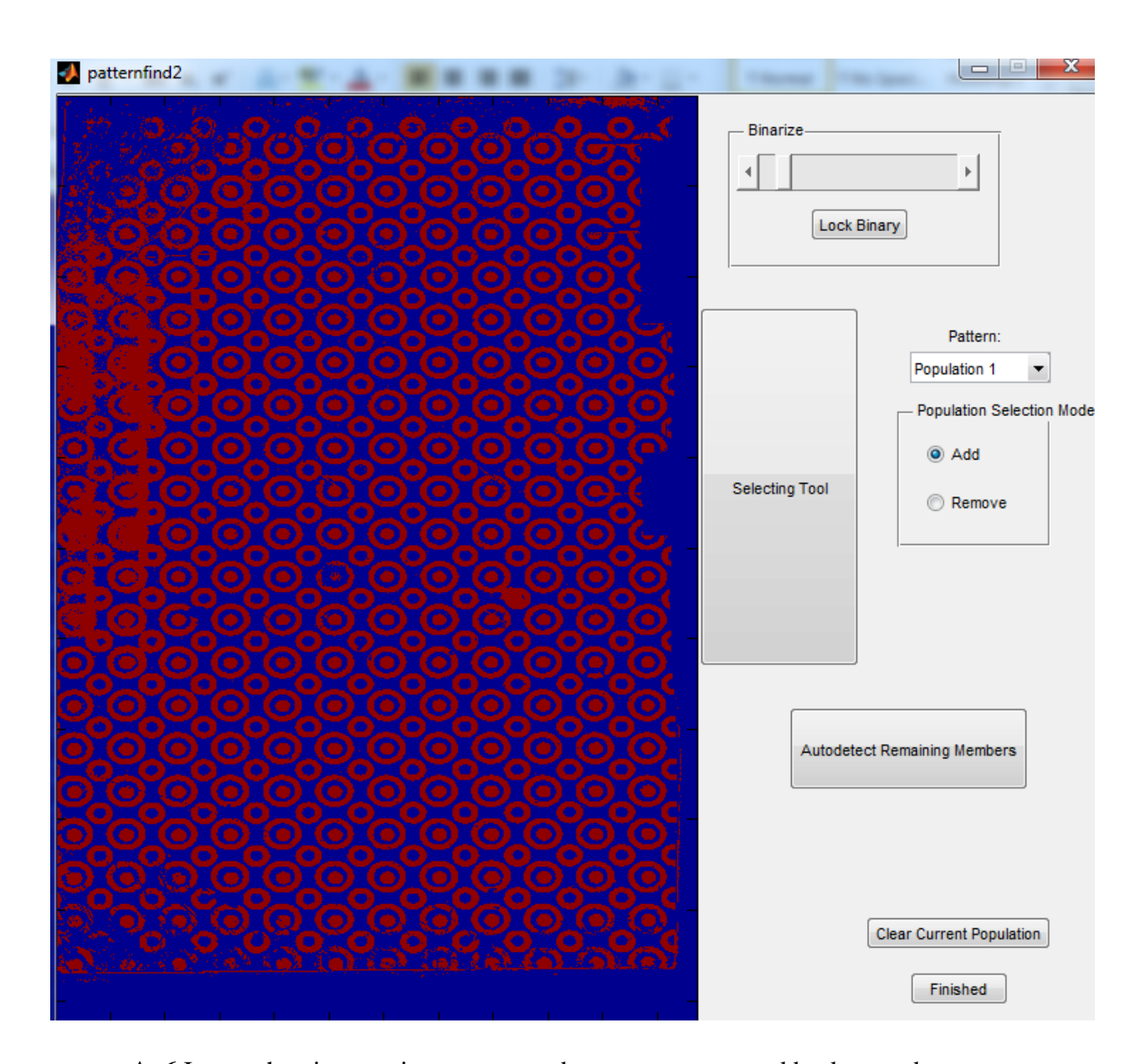
Each shape type will be defined as a population.
Please indicate the total number of populations: 3
Starting pattern selection interface...
varargout =
173.0020
```

A GUI will appear for selecting the patterns for each population.



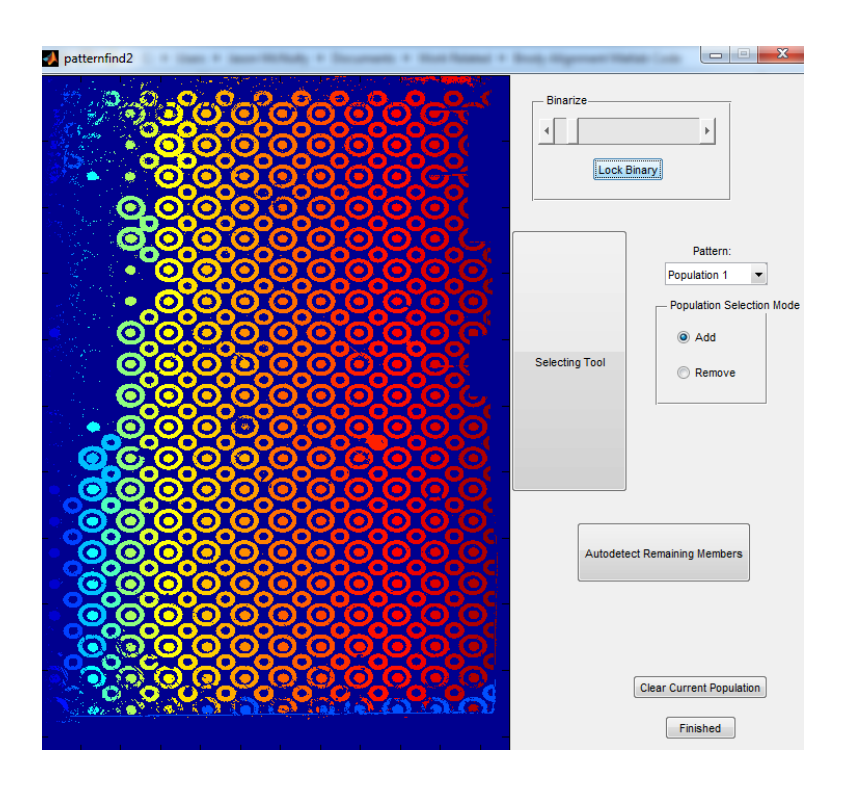
A. 5 GUI for determining binary scale, and selecting each population.

Set binary scale bar until clearest contrast between background and ROI's can be seen:



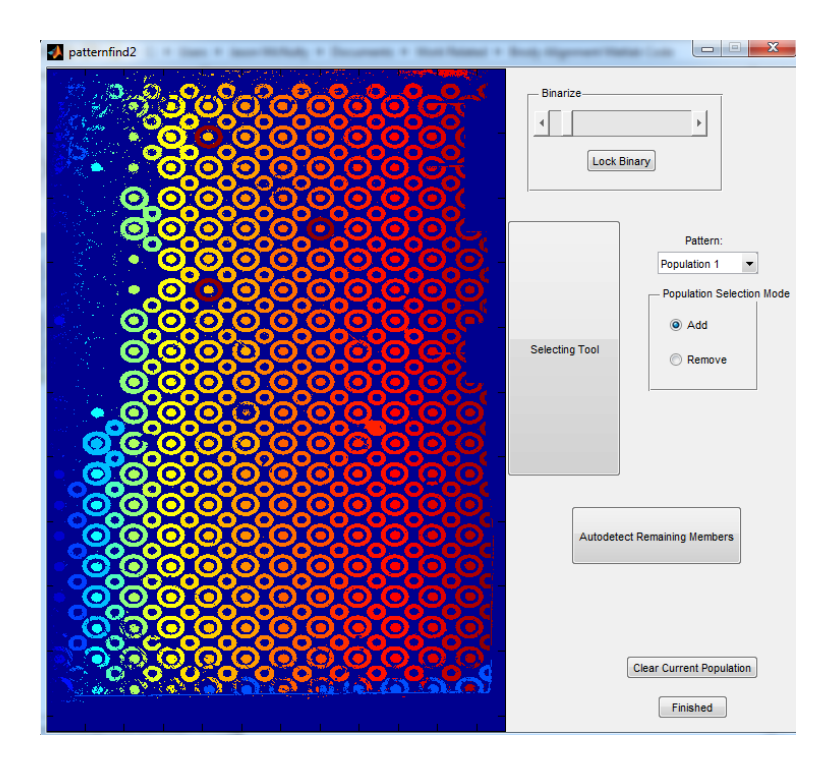
A. 6 Image showing maximum contrast between patterns and background

Select Lock Binary, and the image will be frozen for further analysis



A. 7 Image displaying binarized image once it has been locked.

Select Pattern: population 1, then click selecting tool and select a number of ROIs in population 1:



A. 8 Image showing 3 selected ROIs in population 1

Select autodetect remaining members, and wait for computation to complete.

Upon completion, the command window in Matlab will display:

```
Image binarized. You may begin selecting population members. Popup menu altered. Population 1 selected.

Please select population members to ADD or REMOVE...

Please select population members to ADD or REMOVE...

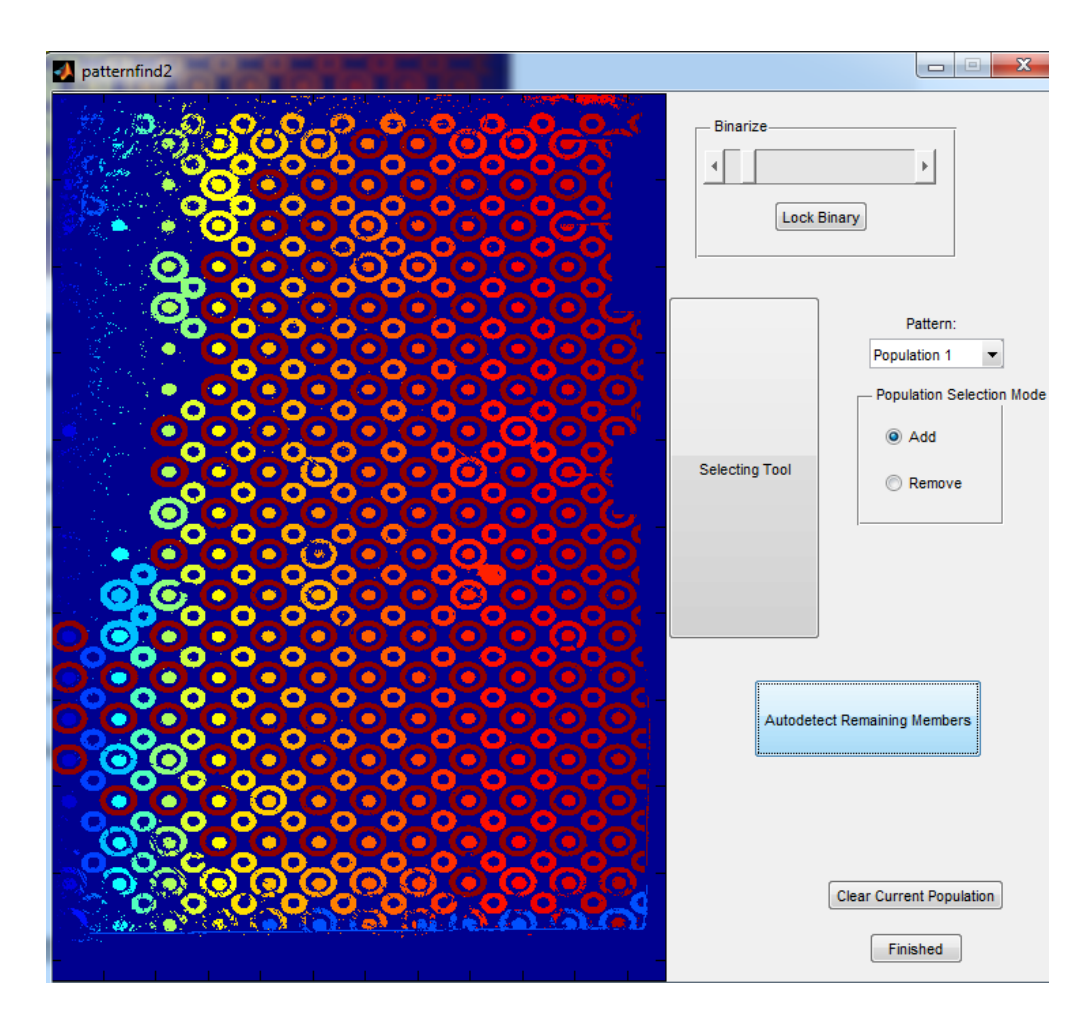
Please select population members to ADD or REMOVE...

Autodetect selected...

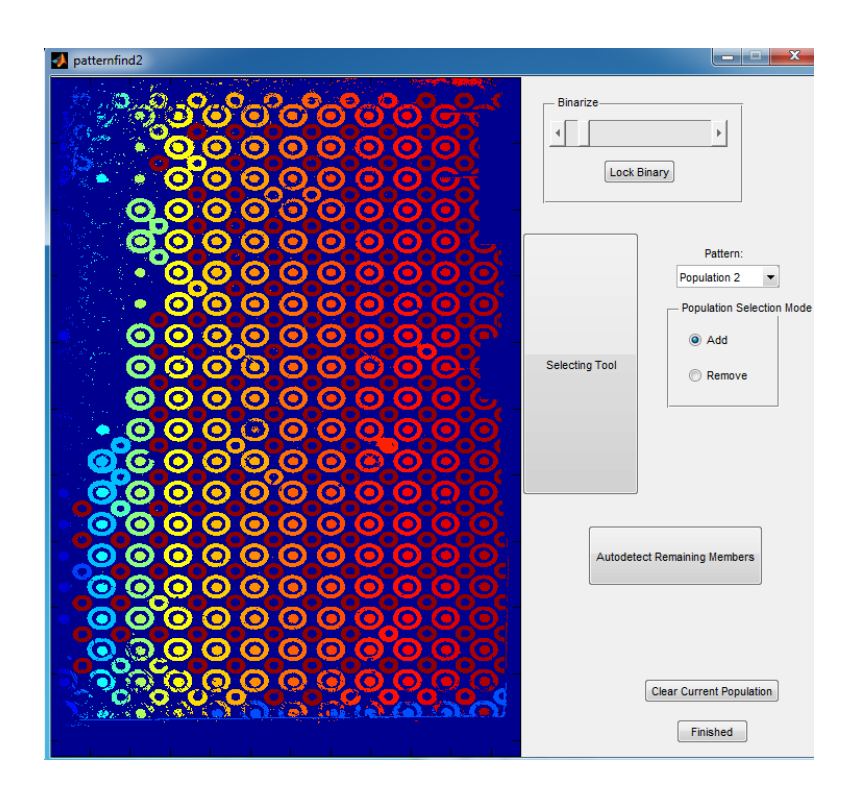
Used currently selected ROIs to determine ROI property threshol 147 members detected that are similar to the selected members.

Adding autodetected members to overall population 1
```

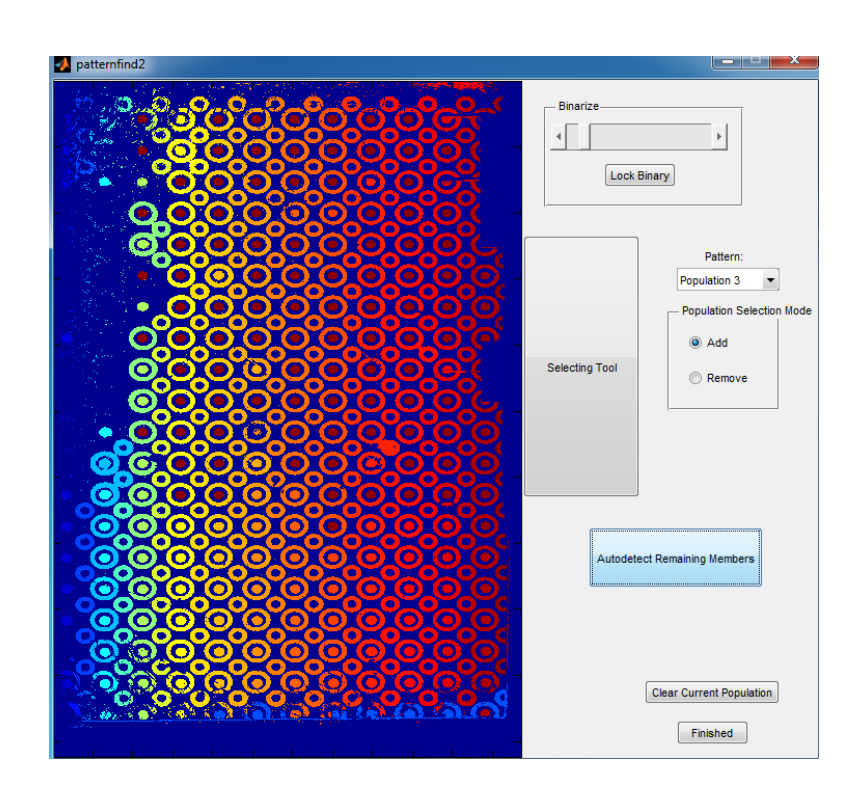
And the GUI will display:



A. 9 Image showing 147 ROIs in population 1 selected through auto-detection Select Pattern, Population 2, selecting tool, repeat the process. Same for population 3.



A. 10 Image showing ROIs in population 2 which were selected via autodetection



A. 11 Image showing ROIs in population 3 which were selected via autodetection

Select Finished



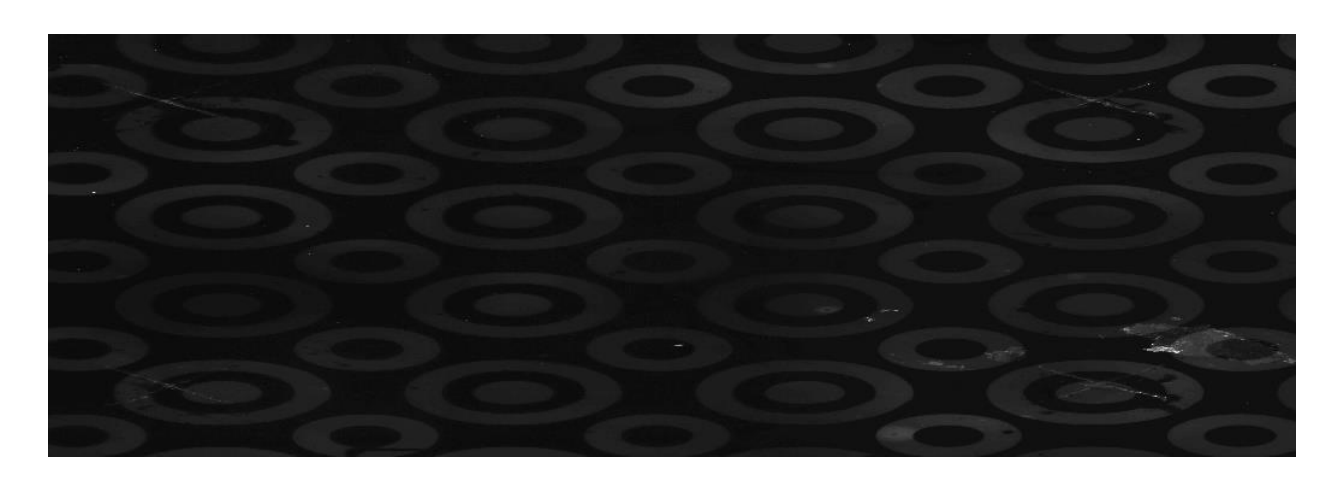
A. 12 Open button to load selected TIFF

Define the known Population 2 and population 3 XY offsets in relation to population 1 (expected offset)

```
Please input the designed offset for each population in
Population 2 X offset (um): 600
Population 2 Y offset (um): 600
Population 3 X offset (um): 0
Population 3 Y offset (um): 0
```

It will automatically define the centroids.

Next, zoom in on the next GUI screen until you can see all 4 etched marks in one window.



A. 13 Zoomed image showing all 4 etch marks in one field of view.

Select ENTER

Select the center of each etch mark with the pointer tool

Results for compensation values to ensure concentricity will be output at the bottom of the Command Window.

MATLAB Results

The table below indicates the values calculated from the MATLAB analysis pre and post compensation offsets.

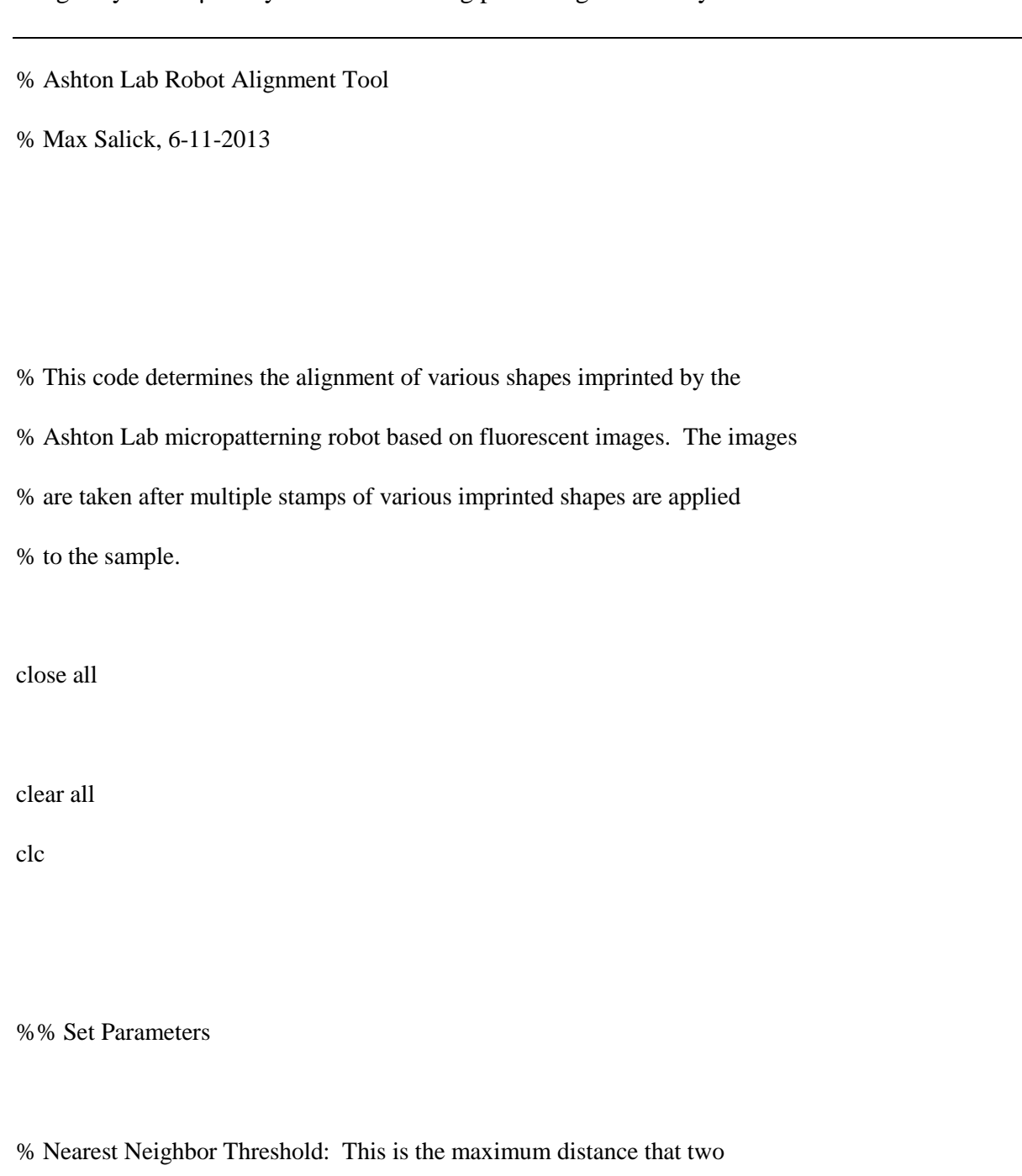
A. 14 MATLAB analysis value results – pre and post-compensation offsets.

	X	Y		E
R-µCP Accuracy	(µm)	(µm)	(°)	
	2	4		0
Pop 2, Pre-comp	6.9174	4.1080	.1796	
	1	8		0
Pop 3, Pre-comp	6.2371	5.4400	.0057	
	5	6		0
Pop 2, Post-comp	.9544	.6633	.0275	
	1	1		0
Pop 3, Post-comp	.2456	.3890	.0714	
	1	5		0
pop 2 stdev	0.4373	.1998	.0108	
pop 3 stdev	8	1		0

					.5446		.4467		.0041	
	pop	2	stdev	post		7		8		0
comp					.4729		.0023		.0530	
	pop	3	stdev	post		7		7		0
comp					.0557		.0491		.0176	

Appendix VI – MATLAB Code for Chapter 4

Below is the custom MATLAB code and user guide for analyzing the fluorescent images by the R- μCP system for assessing patterning uniformity.



```
% members may be to still be considered 'overlapping' (in pixels). By default, this
% number will be 50.
nnthresh = 50;
disp(['Nearest neighbor threshold: 'num2str(nnthresh) ]);
%% Prompt User to Locate Images
disp(['Locate images'])
[FileName,PathName] = uigetfile('*.tif','Select an Image Containing Sarcomere
Structures', 'Z:\msalick\Current Experiments', 'Multiselect', 'off');
res = get(0,'ScreenSize');
horres = res(3);
vertres=res(4);
%% Get Image Data Ready, and Normalize
global imagedataorig
        imagedata = imread([PathName FileName]);
  imagedata = imagedata(:,:,1);
```

```
imagedata = imresize(imagedata,0.25);
  imsize = size(imagedata);
imagemax = double(max(max(imagedata)));
imagecorrect= double(255/imagemax);
imagedata=imagedata*imagecorrect;
imagedataorig = imagedata;
imagedatamod = imagedata;
rois = zeros(size(imagedata));
%% Set Scale
sprintf(['Ashton Lab Robot Alignment Tool, Max Salick 6-11-2013', ...
  '\n----', ...
  '\n\nScale must be set...', ...
  '\n
        1 - Use scalebar in image to calibrate', ...
  '\n
        2 - Direct input of pixel/um ratio', ...
        3 - Set no scale (arbitrary scale will be set)', ...
  '\n
        4 - Use last-used pixel/um ratio'])
  '\n
scalemode = input('Select Option: ');
if scalemode ==1
```

```
colormap('gray')
  imagesc(imagedataorig);
  colormap('gray')
    [scalepointx,scalepointy] = ginput(2);
    close all
    scaleinput = input('Input the known distance between points: ');
    pixeldist = ((scalepointx(1)-scalepointx(2))^2 + (scalepointy(1)-scalepointy(2))^2)^5;
    umperpix = scaleinput/pixeldist;
     disp(['Selected scale is 'num2str(umperpix) ' microns per pixel'])
elseif scalemode==2
  umperpix = input('Input known microns-per-pixel: ');
elseif scalemode==3
  sprintf(['Setting arbitrary calibration of 1 micron per pixel'])
  umperpix = 1;
elseif scalemode==4
  load umperpix
  disp(['Selected scale is 'num2str(umperpix) 'microns per pixel'])
else
  sprintf(['Whoops?']);
  stop
end
save('umperpix','umperpix');
```

```
%% ROI Selections
global popnames
global population_totalnum
global popims
global roimarked
disp(' ')
disp('.....')
disp(' ')
disp('Each shape type will be defined as a population.')
population_totalnum = input('Please indicate the total number of populations: ');
disp(' ')
for k=1:population_totalnum
  popnames{k} = ['Population ' num2str(k)];
  popims{k} = logical(0.*imagedataorig);
end
roimarked = zeros(size(imagedataorig));
disp('Starting pattern selection interface...')
average intense = mean (mean (image data orig)) \\
```

```
[varargout] = patternfind2(imagedataorig,popnames,popims)
uiwait(patternfind2)
% % % % % % % % % % HAVE ROIS, WILL PLOT!
rois = imerode(popims{1},1);
roilabel = bwlabel(rois);
roicoords = regionprops(roilabel(1:end,end:-1:1),'Centroid');
roicoords = cat(1, roicoords.Centroid);
intenses = [];
for k1=1:max(max(roilabel))
  aveintense = mean(imagedataorig(find(bwlabel(roilabel)==k1)));
  intenses = [intenses; aveintense];
end
roix = roicoords(:,1);
roiy = roicoords(:,2);
roiz = intenses;
subplot(1,4,1)
imagesc(imagedataorig)
axis image
```

```
subplot(1,4,2)
tri = delaunay(roix,roiy);
trisurf(tri,roix,roiy,roiz)
axis([min(roix) max(roix) min(roiy) max(roiy) 0 max(roiz)]);
axis image
view([180 90]);
subplot(1,4,3:4)
% figure
roied = rois.*double(imagedataorig);
imshrink = imresize(roied(1:1:end,end:-1:1),.25);
imorigshrink = imresize(imagedataorig(1:1:end,end:-1:1),.25);
% imshrink = imresize(imagedataorig(1:1:end,end:-1:1),.25);
x=0*imshrink;
surface(x,imorigshrink,'FaceColor','texturemap','EdgeColor','none','CDataMapping','direct')
% imagesc(imagedataorig)
hold on
% trisurf(tri,roix,roiy,roiz)
surface(double(imshrink), 'EdgeColor', 'none', 'FaceAlpha', .75)
axis image
view([135 75]);
%
% [imsizex,imsizey]=size(imshrink);
% [X,Y]=meshgrid(1:imsizex,1:imsizey);
```

```
% surf(X,Y,imshrink')
mean(roiz)
std(roiz)
mean(mean(imagedataorig))
hold off
averageintense = mean(mean(imagedataorig))
% figure
% imshrink = imresize(imagedataorig(1:1:end,end:-1:1),.25);
% x=0*imshrink;
% surface(x,imshrink,'FaceColor','texturemap','EdgeColor','none','CDataMapping','direct')
% % imagesc(imagedataorig)
% hold on
% % trisurf(tri,roix,roiy,roiz)
% figure
% surface(double(imshrink), 'EdgeColor', 'none', 'FaceAlpha', .75)
% view([135 80]);
% figure
% tri = delaunay(roix/4,roiy/4);
% trisurf(tri,roix/4,roiy/4,roiz)
%
```

% %% Prompt User for Predicted Population Offset

```
% disp(' ');
% disp('Population selection completed!');
% disp(' ');
% disp('-----')
% disp('Starting coordinate detection and matching module...')
% disp(' ')
%
% disp('Please input the designed offset for each population in comparison to Population 1.');
%
% for k=2:population_totalnum
%
    offsetx{k} = input(['Population ' num2str(k) ' X offset (um): ']);
%
%
    offsetx{k} = offsetx{k}/umperpix;
%
%
%
    offsety{k} = input(['Population ' num2str(k) ' Y offset (um): ']);
%
%
    offsety\{k\} = offsety\{k\}/umperpix;
% end
%
% offsetx{1} = 0;
% offsety\{1\} = 0;
%
% disp(' ');
```

```
% disp('Patterns selected and defined; determining coordinates and performing nearest-neighbor
computations...')
%
% figure
% hold on
%
% %% Convert ROI Data to Population Coordinates
%
% for k = 1:population_totalnum
% disp(['Finding centroid coordinates of population 'num2str(k) '...'])
%
%
     currentrois = popims{k}.*roimarked;
%
     roiprops = regionprops(currentrois);
%
%
     regprops = regionprops(currentrois);
%
     arealist = [regprops.Area];
%
    idx = find(arealist > 1);
%
     posareas = arealist(idx);
%
%
%
     centlist = [regprops.Centroid];
     xlocs = centlist(2.*idx-1);
%
     ylocs = centlist(2.*idx);
%
%
```

```
coords = [xlocs' ylocs'];
%
%
     coords(:,2) = imsize(1) - coords(:,2);
     coordsave\{k\} = coords;
%
%
%
     scatter(coordsave\{k\}(:,1),coordsave\{k\}(:,2));
     pause(.000001);
%
%
    coordsave\{k\} = [coords(:,1)-offsetx\{k\} coords(:,2)-offsety\{k\}];
%
%
    saveareas{k} = posareas;
%
%
% end
%
% %% Run Nearest-Neighbor Analysis to Produce Valid Coordinate Arrays
%
% title('All-Population Scatterplot')
%
% hold off
% clear coordvalid
% clear allmins
% clear dists
% clear xmiss
% clear ymiss
% clear xmissave
```

```
% clear ymissave
 % for k=2:population_totalnum
%
                     countup = 1;
%
%
                     for vi = 1:max(size(coordsave{k}))
%
                               dists \{k\}(vi,:)=((coordsave\{k\}(vi,1)-coordsave\{1\}(:,1)).^2+(coordsave\{k\}(vi,2)-coordsave\{k\}(vi,2)-coordsave\{k\}(vi,2)-coordsave\{k\}(vi,2)-coordsave\{k\}(vi,2)-coordsave\{k\}(vi,2)-coordsave\{k\}(vi,2)-coordsave\{k\}(vi,2)-coordsave\{k\}(vi,2)-coordsave\{k\}(vi,2)-coordsave\{k\}(vi,2)-coordsave\{k\}(vi,2)-coordsave\{k\}(vi,2)-coordsave\{k\}(vi,2)-coordsave\{k\}(vi,2)-coordsave\{k\}(vi,2)-coordsave\{k\}(vi,2)-coordsave\{k\}(vi,2)-coordsave\{k\}(vi,2)-coordsave\{k\}(vi,2)-coordsave\{k\}(vi,2)-coordsave\{k\}(vi,2)-coordsave\{k\}(vi,2)-coordsave\{k\}(vi,2)-coordsave\{k\}(vi,2)-coordsave\{k\}(vi,2)-coordsave\{k\}(vi,2)-coordsave\{k\}(vi,2)-coordsave\{k\}(vi,2)-coordsave\{k\}(vi,2)-coordsave\{k\}(vi,2)-coordsave\{k\}(vi,2)-coordsave\{k\}(vi,2)-coordsave\{k\}(vi,2)-coordsave\{k\}(vi,2)-coordsave\{k\}(vi,2)-coordsave\{k\}(vi,2)-coordsave\{k\}(vi,2)-coordsave\{k\}(vi,2)-coordsave\{k\}(vi,2)-coordsave\{k\}(vi,2)-coordsave\{k\}(vi,2)-coordsave\{k\}(vi,2)-coordsave\{k\}(vi,2)-coordsave\{k\}(vi,2)-coordsave\{k\}(vi,2)-coordsave\{k\}(vi,2)-coordsave\{k\}(vi,2)-coordsave\{k\}(vi,2)-coordsave\{k\}(vi,2)-coordsave\{k\}(vi,2)-coordsave\{k\}(vi,2)-coordsave\{k\}(vi,2)-coordsave\{k\}(vi,2)-coordsave\{k\}(vi,2)-coordsave\{k\}(vi,2)-coordsave\{k\}(vi,2)-coordsave\{k\}(vi,2)-coordsave\{k\}(vi,2)-coordsave\{k\}(vi,2)-coordsave\{k\}(vi,2)-coordsave\{k\}(vi,2)-coordsave\{k\}(vi,2)-coordsave\{k\}(vi,2)-coordsave\{k\}(vi,2)-coordsave\{k\}(vi,2)-coordsave\{k\}(vi,2)-coordsave\{k\}(vi,2)-coordsave\{k\}(vi,2)-coordsave\{k\}(vi,2)-coordsave\{k\}(vi,2)-coordsave\{k\}(vi,2)-coordsave\{k\}(vi,2)-coordsave\{k\}(vi,2)-coordsave\{k\}(vi,2)-coordsave\{k\}(vi,2)-coordsave\{k\}(vi,2)-coordsave\{k\}(vi,2)-coordsave\{k\}(vi,2)-coordsave\{k\}(vi,2)-coordsave\{k\}(vi,2)-coordsave\{k\}(vi,2)-coordsave\{k\}(vi,2)-coordsave\{k\}(vi,2)-coordsave\{k\}(vi,2)-coordsave\{k\}(vi,2)-coordsave\{k\}(vi,2)-coordsave\{k\}(vi,2)-coordsave\{k\}(vi,2)-coordsave\{k\}(vi,2)-coordsave\{k\}(vi,2)-coordsave\{k\}(vi,2)-coordsave\{k\}(vi,2)-coordsave\{k\}(vi,2)-coordsave\{k\}(vi,2)-coordsave\{k\}(vi,2)-coordsave\{k\}(vi,2)-coordsave\{k\}(vi,2)-coordsave\{k\}(vi,2)-coordsave\{k\}(vi,2)-coordsave\{k\}(vi,2)-coordsave\{k\}(vi,2)-coordsave\{k\}(vi,2)-coordsave\{k\}(vi,2)-coordsav
%
coordsave{1}(:,2)).^2).^.5;
%
%
                               [mindist,bestpop1] = min(dists\{k\}(vi,:));
%
                               if mindist <= nnthresh
%
% %
                                                     mindist
                                          xmiss\{k\}(vi) = coordsave\{k\}(vi,1)-coordsave\{1\}(bestpop1,1);
%
%
                                          ymiss\{k\}(vi) = coordsave\{k\}(vi,2)-coordsave\{1\}(bestpop1,2);
%
%
                                          coordvalid\{k\}(countup,1) = coordsave\{k\}(vi,1);
                                          coordvalid\{k\}(countup,2) = coordsave\{k\}(vi,2);
%
%
                                          coordvalid\{k\}(countup,3) = coordsave\{1\}(bestpop1,1);
%
                                          coordvalid\{k\}(countup,4) = coordsave\{1\}(bestpop1,2);
%
                                          countup = countup+1;
%
%
                               end
 %
```

```
%
%
       allmins\{k\}(vi) = mindist;
%
%
%
     end
% end
% %% Find Hatchmark Center via GUI
%
% disp(' ')
% disp('Population coordinates determined.')
% disp('Now the global center must be determined to indicate axis of rotation.');
%
% disp(' ')
% disp('Zoom is currently enabled. Please locate the hatchmarks and set the')
% disp('zoom so that all hatchmarks are clearly framed withing the figure.')
% disp(' ')
% disp('When finished, press ENTER to begin point selection.')
% disp(' ')
%
% % figure
% % imagesc(imagedataorig);
% % colormap(gray)
% %
      [hatch_x, hatch_y] = ginput(4);
% %
```

```
%
% imagesc(imagedataorig);
% colormap(gray)
% zoom on; % use mouse button to zoom in or out
% % Press Enter to get out of the zoom mode.
%
% % CurrentCharacter contains the most recent key which was pressed after opening
% % the figure, wait for the most recent key to become the return/enter key
% waitfor(gcf,'CurrentCharacter',13)
%
% zoom reset
% zoom off
% disp('Please select the hatchmarks visible on the sample to determine this center.');
% disp(' ')
% disp('Select the hatchmarks in the FOLLOWING ORDER:')
% disp(' ')
% disp(' 1----2');
% disp(' | |');
% disp(' | |');
% disp(' | |');
% disp(' 3----4');
% disp(' ')
% [hatch_x, hatch_y] = ginput(4);
%
```

```
% globalcent_x = mean(hatch_x);
% globalcent_y = mean(hatch_y);
%
% %
% % xmissave\{k\} = mean(coordvalid\{k\}(:,1)-coordvalid\{k\}(:,3));
% % ymissave\{k\} = (mean(coordvalid\{k\}(:,2)-coordvalid\{k\}(:,4)));
% %
% % figure
% %
% % quiver(coordvalid{k}(:,1),coordvalid{k}(:,2),coordvalid{k}(:,1)-
coordvalid\{k\}(:,3),coordvalid\{k\}(:,2)-coordvalid\{k\}(:,4)\};
% % title(['Overall offset of Population 'num2str(k)]);
% %
% %
% % disp(' ')
% % disp(['Population ' num2str(k) ' displacement statistics:'])
% % disp(['Average X offset: 'num2str(xmissave{k}*umperpix) 'um'])
% % disp(['Average Y offset: 'num2str(ymissave{k}*umperpix) 'um'])
% % disp(' ')
% %
% % relxoff\{k\} = coordvalid\{k\}(:,1)-coordvalid\{k\}(:,3)-xmissave\{k\};
% % relyoff\{k\} = coordvalid\{k\}(:,2)-coordvalid\{k\}(:,4)-ymissave\{k\};
% %
% % overalloff\{k\} = (relxoff\{k\}.^2 + relyoff\{k\}.^2).^5;
```

```
% %
% % figure
% %
% % quiver(coordvalid{k}(:,1),coordvalid{k}(:,2),relxoff{k},relyoff{k});
% % title(['Relative offset of Population 'num2str(k)]);
% %
% for k = 2:population_totalnum
%
% % Centering around global center....
% ncoordvalid\{k\}(:,1) = coordvalid\{k\}(:,1) - globalcent_x;
% ncoordvalid\{k\}(:,3) = coordvalid\{k\}(:,3) - globalcent_x;
% ncoordvalid\{k\}(:,2) = coordvalid\{k\}(:,2) - globalcent_y;
% ncoordvalid\{k\}(:,4) = coordvalid\{k\}(:,4) - globalcent_y;
%
%
% % Use Horn's quaternion-based method to find optimal transposition matrix
% [regParams,Bfit,ErrorStats]= ...
%
     absor([ncoordvalid{k}(:,1) ncoordvalid{k}(:,2)]', ...
%
     [ncoordvalid\{k\}(:,3) ncoordvalid\{k\}(:,4)]');
%
% transposeinfo{k} = regParams;
% absolve_xoff{k} = regParams.t(1)*-umperpix;
% absolve_yoff{k} = regParams.t(2)*-umperpix;
% absolve_rot\{k\} = 360-regParams.theta;
```

```
%
% fixedcoords\{k\} = (transposeinfo\{k\}.M*[ncoordvalid\{k\}(:,1) ncoordvalid\{k\}(:,2) ...
%
    ones(1,max(size(ncoordvalid{k}(:,1))))']')';
%
% fixedcoords{k} = fixedcoords{k}(:,1:2);
%
% origerror\{k\}= mean(abs(ncoordvalid\{k\}(:,4) - ncoordvalid\{k\}(:,2))+ ...
%
    (abs(ncoordvalid\{k\}(:,3) - ncoordvalid\{k\}(:,1))));
% newerror(k) = mean(abs(ncoordvalid\{k\}(:,4) - fixedcoords\{k\}(:,2)) + ...
%
    (abs(ncoordvalid{k}(:,3) - fixedcoords{k}(:,1))));
%
%
%
% end
%
%
%
%
% disp(' ')
% disp(' ')
% disp(FileName)
% disp('-----')
% disp('Suggested Corrections to Match Populations:')
% for k=2:population_totalnum
```

```
transangle\{k\} = transposeinfo\{k\}.theta;
%
%
     if transangle\{k\} > 180
%
       transangle\{k\} = transangle\{k\} - 360;
%
     end
%
%
     disp(['Population ' num2str(k) ' should be rotated ' ...
%
        num2str(transangle{k}) ' degrees ( positive=CCW )']);
%
     disp(['Population ' num2str(k) ' should be translated ' ...
%
%
        num2str(transposeinfo{k}.t(1)*umperpix) 'um in the +X direction']);
%
     disp(['Population ' num2str(k) ' should be translated ' ...
        num2str(transposeinfo{k}.t(2)*umperpix) 'um in the +Y direction']);
%
% disp(' ')
% end
%
% function [poplocs] = patternfind2(imagedataorig,popnames,popims)
function varargout = patternfind2(varargin)
% PATTERNFIND2 M-file for patternfind2.fig
     PATTERNFIND2, by itself, creates a new PATTERNFIND2 or raises the existing
%
     singleton*.
%
%
%
     H = PATTERNFIND2 returns the handle to a new PATTERNFIND2 or the handle to
     the existing singleton*.
%
%
```

```
%
     PATTERNFIND2('CALLBACK',hObject,eventData,handles,...) calls the local
%
     function named CALLBACK in PATTERNFIND2.M with the given input arguments.
%
     PATTERNFIND2('Property', 'Value',...) creates a new PATTERNFIND2 or raises the
%
%
     existing singleton*. Starting from the left, property value pairs are
     applied to the GUI before patternfind2_OpeningFcn gets called. An
%
%
     unrecognized property name or invalid value makes property application
%
     stop. All inputs are passed to patternfind2 OpeningFcn via varargin.
%
     *See GUI Options on GUIDE's Tools menu. Choose "GUI allows only one
%
     instance to run (singleton)".
%
%
% See also: GUIDE, GUIDATA, GUIHANDLES
% Edit the above text to modify the response to help patternfind2
% Last Modified by GUIDE v2.5 14-Jun-2013 18:48:23
% Begin initialization code - DO NOT EDIT
gui_Singleton = 1;
gui_State = struct('gui_Name',
                                mfilename, ...
           'gui_Singleton', gui_Singleton, ...
           'gui_OpeningFcn', @patternfind2_OpeningFcn, ...
           'gui_OutputFcn', @patternfind2_OutputFcn, ...
```

```
'gui_LayoutFcn', [], ...
           'gui_Callback', []);
if nargin && ischar(varargin{1})
  gui_State.gui_Callback = str2func(varargin{1});
end
if nargout
  [varargout{1:nargout}] = gui_mainfcn(gui_State, varargin{:});
else
  gui_mainfcn(gui_State, varargin{:});
end
% End initialization code - DO NOT EDIT
% --- Executes just before patternfind2 is made visible.
function patternfind2_OpeningFcn(hObject, eventdata, handles, varargin)
% This function has no output args, see OutputFcn.
% hObject handle to figure
% eventdata reserved - to be defined in a future version of MATLAB
% handles structure with handles and user data (see GUIDATA)
% varargin command line arguments to patternfind2 (see VARARGIN)
global popnames;
global population_totalnum;
```

```
global popims
global imagedataorig
popnames;
population_totalnum;
handles.popnames = popnames;
handles.population_totalnum = population_totalnum;
imagesc(imagedataorig)
set(handles.patternindicate, 'String', handles.popnames)
% handles.patternindicate.String = popnames;
% handles.patternindicate.Value = 1:population_totalnum;
% handles.patternindicate;
% class(handles.patternindicate.String)
% Choose default command line output for patternfind2
handles.output = hObject;
% indicatorarray = 1:populationnumber;
% Update handles structure
guidata(hObject, handles);
% UIWAIT makes patternfind2 wait for user response (see UIRESUME)
% uiwait(handles.patternfinder);
```

```
% --- Outputs from this function are returned to the command line.
function varargout = patternfind2_OutputFcn(hObject, eventdata, handles)
% varargout cell array for returning output args (see VARARGOUT);
% hObject handle to figure
% eventdata reserved - to be defined in a future version of MATLAB
% handles structure with handles and user data (see GUIDATA)
% Get default command line output from handles structure
varargout{1} = handles.output;
% --- Executes on selection change in patternindicate.
function patternindicate_Callback(hObject, eventdata, handles)
global popims
val = get(hObject,'Value');
handles.pop_currentpop = val;
handles.pop_currentname = handles.popnames{val};
handles.pop_currentname;
```

```
imagesc(handles.roimarked-
handles.roimarked.*popims{handles.pop_currentpop}+max(max(handles.roimarked)).*popims{handl
es.pop_currentpop})
disp(['Popup menu altered. ' handles.pop_currentname ' selected.'])
handles.output = hObject;
guidata(hObject,handles)
% hObject handle to patternindicate (see GCBO)
% eventdata reserved - to be defined in a future version of MATLAB
% handles structure with handles and user data (see GUIDATA)
% Hints: contents = get(hObject, 'String') returns patternindicate contents as cell array
%
      contents{get(hObject,'Value')} returns selected item from patternindicate
% --- Executes during object creation, after setting all properties.
function patternindicate_CreateFcn(hObject, eventdata, handles)
% hObject handle to patternindicate (see GCBO)
% eventdata reserved - to be defined in a future version of MATLAB
% handles empty - handles not created until after all CreateFcns called
% Hint: popupmenu controls usually have a white background on Windows.
```

%

See ISPC and COMPUTER.

```
if ispc && isequal(get(hObject, 'BackgroundColor'), get(0,'defaultUicontrolBackgroundColor'))
  set(hObject,'BackgroundColor','white');
end
% --- Executes on button press in but_finished.
function but_finished_Callback(hObject, eventdata, handles)
global popims
global roimarked
roimarked = handles.roimarked;
varagout.popims = popims;
varargout.roimarked = roimarked;
close(handles.patternfinder)
handles.output = hObject;
% guidata(hObject,handles)
% hObject handle to but_finished (see GCBO)
% eventdata reserved - to be defined in a future version of MATLAB
% handles structure with handles and user data (see GUIDATA)
```

```
% --- Executes on button press in but_selectingtool.
function but_selectingtool_Callback(hObject, eventdata, handles)
global popims
disp('Please select population members to ADD or REMOVE...')
if handles.mode == 1
  handles.pop_currentpop;
  [roix, roiy] = ginput(1);
  roix = floor(roix);
  roiy = floor(roiy);
  handles.selectedroi = handles.roimarked(roiy,roix);
  handles.selectedroi;
  indexroi = handles.roimarked == handles.selectedroi;
  if popims{handles.pop_currentpop}(roiy,roix) ==0 && handles.selectedroi ~= 0
  popims{handles.pop_currentpop} = popims{handles.pop_currentpop} + indexroi;
    disp('Population
  end
  imagesc(handles.roimarked-
handles.roimarked.*popims{handles.pop_currentpop}+max(max(handles.roimarked)).*popims{handl
es.pop_currentpop});
```

```
elseif handles.mode == 0
  [roix, roiy] = ginput(1);
  roix = floor(roix);
  roiy = floor(roiy);
  handles.selectedroi = handles.roimarked(roiy,roix);
  handles.selectedroi;
  indexroi = handles.roimarked == handles.selectedroi;
  if popims{handles.pop_currentpop}(roiy,roix) ==1
       popims{handles.pop_currentpop} = popims{handles.pop_currentpop} -indexroi;
  end
  imagesc(handles.roimarked-
handles.roimarked.*popims{handles.pop_currentpop}+max(max(handles.roimarked)).*popims{handl
es.pop_currentpop});
end
handles.output = hObject;
guidata(hObject,handles)
% hObject handle to but_selectingtool (see GCBO)
% eventdata reserved - to be defined in a future version of MATLAB
```

```
% handles structure with handles and user data (see GUIDATA)
% --- Executes on button press in radbut_addmode.
function radbut_addmode_Callback(hObject, eventdata, handles)
handles.mode = 1;
disp('Mode switched to ADD population members.')
handles.output = hObject;
guidata(hObject,handles)
% hObject handle to radbut_addmode (see GCBO)
% eventdata reserved - to be defined in a future version of MATLAB
% handles structure with handles and user data (see GUIDATA)
% Hint: get(hObject,'Value') returns toggle state of radbut_addmode
% --- Executes on button press in radbut_removemode.
function radbut_removemode_Callback(hObject, eventdata, handles)
handles.mode = 0;
disp('Mode switched to REMOVE population members.')
```

```
handles.output = hObject;
guidata(hObject,handles)
% hObject handle to radbut_removemode (see GCBO)
% eventdata reserved - to be defined in a future version of MATLAB
% handles structure with handles and user data (see GUIDATA)
% Hint: get(hObject,'Value') returns toggle state of radbut_removemode
% --- Executes on slider movement.
function slid_binaryslider_Callback(hObject, eventdata, handles)
global imagedataorig
handles.binaryval = get(hObject,'Value');
sliderval = handles.binaryval;
handles.roibin = roicolor(imagedataorig,floor(255*sliderval),255);
imagesc(handles.roibin)
handles.output = hObject;
guidata(hObject,handles)
% hObject handle to slid_binaryslider (see GCBO)
% eventdata reserved - to be defined in a future version of MATLAB
% handles structure with handles and user data (see GUIDATA)
```

```
% Hints: get(hObject,'Value') returns position of slider
%
      get(hObject, 'Min') and get(hObject, 'Max') to determine range of slider
% --- Executes during object creation, after setting all properties.
function slid_binaryslider_CreateFcn(hObject, eventdata, handles)
% hObject handle to slid_binaryslider (see GCBO)
% eventdata reserved - to be defined in a future version of MATLAB
% handles empty - handles not created until after all CreateFcns called
% Hint: slider controls usually have a light gray background.
if isequal(get(hObject, 'BackgroundColor'), get(0,'defaultUicontrolBackgroundColor'))
  set(hObject, 'BackgroundColor', [.9.9.9]);
end
% --- Executes on button press in but_lockbinary.
function but_lockbinary_Callback(hObject, eventdata, handles)
handles.roibin = bwareaopen(handles.roibin, 30);
handles.roibin = imdilate(handles.roibin,strel('disk',3));
handles.roibin = imerode(handles.roibin,strel('disk',3));
handles.roimarked = bwlabel(handles.roibin);
imagesc(handles.roimarked);
```

```
disp('Image binarized. You may begin selecting population members.')
handles.mode = 1;
handles.output = hObject;
guidata(hObject,handles)
% hObject handle to but_lockbinary (see GCBO)
% eventdata reserved - to be defined in a future version of MATLAB
% handles structure with handles and user data (see GUIDATA)
% --- Executes on button press in but_clearpop.
function but_clearpop_Callback(hObject, eventdata, handles)
global imagedataorig
global popims
popims{handles.pop_currentpop} = zeros(size(imagedataorig));
imagesc(handles.roimarked-
handles.roimarked.*popims{handles.pop_currentpop}+max(max(handles.roimarked)).*popims{handl
es.pop_currentpop});
disp([ handles.pop_currentname ' cleared!'])
handles.output = hObject;
guidata(hObject,handles)
% hObject handle to but_clearpop (see GCBO)
```

```
% eventdata reserved - to be defined in a future version of MATLAB
% handles structure with handles and user data (see GUIDATA)
% --- Executes on button press in but_autodetect.
function but_autodetect_Callback(hObject, eventdata, handles)
global popims
global selectedrois
global allareas
global findgoodrois
disp('Autodetect selected...')
selectedrois = popims{handles.pop_currentpop}.*handles.roimarked;
selroi_area = regionprops(selectedrois,'Area');
selroi_extent = regionprops(selectedrois, 'Extent');
selroi_filledarea = regionprops(selectedrois,'FilledArea');
  arealist = [selroi_area.Area];
  extentlist = [selroi_extent.Extent];
  filledarealist = [selroi_filledarea.FilledArea];
  idx = find(arealist > 1);
  selroi_posarea = arealist(idx);
  selroi_extent = extentlist(idx);
  selroi_filledarea = filledarealist(idx);
```

```
% minarea = mean(selroi_posarea) * 0.7;
% maxarea = mean(selroi posarea) * 1.3;
% minextent = mean(selroi_extent) * 0.7;
% maxextent = mean(selroi_extent) * 1.3;
% minfilled = mean(selroi_filledarea) * 0.7;
% maxfilled = mean(selroi_filledarea) * 1.3;
minarea = mean(selroi posarea) * 0.4;
maxarea = mean(selroi_posarea) * 1.6;
minextent = mean(selroi_extent) * 0.01;
maxextent = mean(selroi_extent) * 10.3;
minfilled = mean(selroi_filledarea) * 0.01;
maxfilled = mean(selroi_filledarea) * 10.3;
disp('Used currently selected ROIs to determine ROI property thresholds...')
% Comparea all ROIs to gathered values
allareas = regionprops(handles.roimarked,'Area');
allextent = regionprops(handles.roimarked, 'Extent');
allfilled = regionprops(handles.roimarked, 'FilledArea');
allarealist = [allareas.Area];
idx1 = find(allarealist > minarea);
idx2 = find(allarealist < maxarea);
allextentlist = [allextent.Extent];
```

```
idx3 = find(allextentlist > minextent);
idx4 = find(allextentlist < maxextent);
allfilledlist = [allfilled.FilledArea];
idx5 = find(allfilledlist > minfilled);
idx6 = find(allfilledlist < maxfilled);
goodrois = intersect(intersect(intersect(intersect(idx1,idx2),idx3),idx4),idx5),idx6);
disp([num2str(max(size(goodrois))) ' members detected that are similar to the selected members.']);
disp(['Adding autodetected members to overall population 'num2str(handles.pop_currentpop)]);
findgoodrois = ismember(handles.roimarked,goodrois);
popims{handles.pop_currentpop} = findgoodrois;
imagesc(handles.roimarked-
handles.roimarked.*popims{handles.pop_currentpop}+max(max(handles.roimarked)).*popims{handl
es.pop_currentpop});
handles.output = hObject;
guidata(hObject,handles)
% hObject handle to but_autodetect (see GCBO)
% eventdata reserved - to be defined in a future version of MATLAB
% handles structure with handles and user data (see GUIDATA)
```

References

- 1. Vacanti, J.P. and R. Langer, *Tissue engineering: the design and fabrication of living replacement devices for surgical reconstruction and transplantation.* The Lancet, 1999. **354**: p. S32-S34.
- 2. Schaner, P.J., et al., *Decellularized vein as a potential scaffold for vascular tissue engineering*. Journal of vascular surgery, 2004. **40**(1): p. 146-153.
- 3. Schmidt, C.E. and J.M. Baier, *Acellular vascular tissues: natural biomaterials for tissue repair and tissue engineering.* Biomaterials, 2000. **21**(22): p. 2215-2231.
- 4. Teebken, O.E. and A. Haverich, *Tissue engineering of small diameter vascular grafts*. European Journal of Vascular and Endovascular Surgery, 2002. **23**(6): p. 475-485.
- 5. Horch, R.E., et al., *Tissue engineering of cultured skin substitutes*. Journal of cellular and molecular medicine, 2005. **9**(3): p. 592-608.
- 6. Wei, G. and P.X. Ma, Structure and properties of nano-hydroxyapatite/polymer composite scaffolds for bone tissue engineering. Biomaterials, 2004. **25**(19): p. 4749-4757.
- 7. Ikada, Y., *Challenges in tissue engineering*. Journal of The Royal Society Interface, 2006. **3**(10): p. 589-601.
- 8. Sun, J. and H. Tan, *Alginate-based biomaterials for regenerative medicine applications*. Materials, 2013. **6**(4): p. 1285-1309.
- 9. Winer, J.P., S. Oake, and P.A. Janmey, *Non-linear elasticity of extracellular matrices enables contractile cells to communicate local position and orientation.* PloS one, 2009. **4**(7): p. e6382.
- 10. Huebsch, N., et al., *Harnessing traction-mediated manipulation of the cell/matrix interface to control stem-cell fate.* Nature materials, 2010. **9**(6): p. 518-526.
- 11. Yang, S., et al., *The design of scaffolds for use in tissue engineering. Part I. Traditional factors.* Tissue engineering, 2001. **7**(6): p. 679-689.
- 12. Drury, J.L. and D.J. Mooney, *Hydrogels for tissue engineering: scaffold design variables and applications*. Biomaterials, 2003. **24**(24): p. 4337-4351.
- 13. Hollister, S.J., *Porous scaffold design for tissue engineering*. Nature materials, 2005. **4**(7): p. 518-524.

- 14. Lutolf, M. and J. Hubbell, *Synthetic biomaterials as instructive extracellular microenvironments for morphogenesis in tissue engineering*. Nature biotechnology, 2005. **23**(1): p. 47-55.
- 15. Braun, D., et al., *Polymer synthesis: theory and practice: fundamentals, methods, experiments.* 2012: Springer Science & Business Media.
- 16. Osswald, T.A., et al., *International plastics handbook.* 2006.
- 17. Hutmacher, D.W., *Scaffolds in tissue engineering bone and cartilage*. Biomaterials, 2000. **21**(24): p. 2529-2543.
- 18. Hutmacher, D.W., Scaffold design and fabrication technologies for engineering tissues—state of the art and future perspectives. Journal of Biomaterials Science, Polymer Edition, 2001. **12**(1): p. 107-124.
- 19. Ashton, R.S., et al., *High-Throughput Screening of Gene Function in Stem Cells Using Clonal Microarrays.* Stem Cells, 2007. **25**(11): p. 2928-2935.
- 20. McNulty, J., et al., *High-precision robotic microcontact printing (R-μCP) utilizing a vision guided selectively compliant articulated robotic arm.* Lab on a Chip, 2014.
- 21. Sha, J., et al., Sequential nucleophilic substitutions permit orthogonal click functionalization of multicomponent PEG brushes. Biomacromolecules, 2013.
- 22. Karimi, A., M. Navidbakhsh, and S. Faghihi, *Fabrication and mechanical characterization of a polyvinyl alcohol sponge for tissue engineering applications*. Perfusion, 2013: p. 0267659113513823.
- 23. Karande, T.S., J.L. Ong, and C.M. Agrawal, *Diffusion in musculoskeletal tissue engineering scaffolds: design issues related to porosity, permeability, architecture, and nutrient mixing.* Annals of biomedical engineering, 2004. **32**(12): p. 1728-1743.
- 24. Mikos, A.G. and J.S. Temenoff, *Formation of highly porous biodegradable scaffolds for tissue engineering*. Electronic Journal of Biotechnology, 2000. **3**(2): p. 23-24.
- 25. Nerem, R.M., *The challenge of imitating nature*. Principles of tissue engineering, 2000: p. 9-15.
- 26. Narayanan, R.P., et al., *Photodegradable iron (III) cross-linked alginate gels.* Biomacromolecules, 2012. **13**(8): p. 2465-2471.
- 27. Skjåk-Bræk, G., H. Grasdalen, and O. Smidsrød, *Inhomogeneous polysaccharide ionic gels*. Carbohydrate polymers, 1989. **10**(1): p. 31-54.
- 28. Hay, I.D., et al., *Bacterial biosynthesis of alginates*. Journal of chemical technology and biotechnology, 2010. **85**(6): p. 752-759.

- 29. Haug, A., *Fractionation of alginic acid*, 1959, MUNKSGAARD INT PUBL LTD 35 NORRE SOGADE, PO BOX 2148, DK-1016 COPENHAGEN, DENMARK. p. 601-603.
- 30. Grant, G.T., et al., *Biological interactions between polysaccharides and divalent cations: the egg-box model.* FEBS letters, 1973. **32**(1): p. 195-198.
- 31. Crow, B. and K. Nelson, *Release of bovine serum albumin from a hydrogel-cored biodegradable polymer fiber*. Biopolymers, 2006. **81**(6): p. 419-427.
- 32. Kuo, C.K. and P.X. Ma, *Ionically crosslinked alginate hydrogels as scaffolds for tissue engineering: part 1. Structure, gelation rate and mechanical properties.* Biomaterials, 2001. **22**(6): p. 511-521.
- 33. Augst, A.D., H.J. Kong, and D.J. Mooney, *Alginate hydrogels as biomaterials*. Macromolecular bioscience, 2006. **6**(8): p. 623-633.
- 34. Drury, J.L., R.G. Dennis, and D.J. Mooney, *The tensile properties of alginate hydrogels*. Biomaterials, 2004. **25**(16): p. 3187-3199.
- 35. Suzuki, Y., et al., Evaluation of a novel alginate gel dressing: Cytotoxicity to fibroblasts in vitro and foreign-body reaction in pig skin in vivo. Journal of biomedical materials research, 1998. **39**(2): p. 317-322.
- 36. Roy, D., J.N. Cambre, and B.S. Sumerlin, *Future perspectives and recent advances in stimuli-responsive materials.* Progress in Polymer Science, 2010. **35**(1): p. 278-301.
- 37. Rzaev, Z.M., S. Dincer, and E. Pişkin, *Functional copolymers of N-isopropylacrylamide for bioengineering applications*. Progress in Polymer Science, 2007. **32**(5): p. 534-595.
- 38. Lee, K.Y., et al., *Hydrogel formation via cell crosslinking*. Advanced Materials, 2003. **15**(21): p. 1828-1832.
- 39. Drury, J.L., T. Boontheekul, and D.J. Mooney, *Cellular cross-linking of peptide modified hydrogels*. Journal of biomechanical engineering, 2005. **127**(2): p. 220-228.
- 40. Smeds, K.A. and M.W. Grinstaff, *Photocrosslinkable polysaccharides for in situ hydrogel formation*. Journal of biomedical materials research, 2001. **54**(1): p. 115-121.
- 41. Zhao, X., et al., *Stress-relaxation behavior in gels with ionic and covalent crosslinks*. Journal of applied physics, 2010. **107**(6): p. 063509.
- 42. Eiselt, P., K.Y. Lee, and D.J. Mooney, *Rigidity of two-component hydrogels prepared from alginate and poly (ethylene glycol)-diamines.* Macromolecules, 1999. **32**(17): p. 5561-5566.

- 43. Lee, K.Y., et al., Controlling mechanical and swelling properties of alginate hydrogels independently by cross-linker type and cross-linking density. Macromolecules, 2000. **33**(11): p. 4291-4294.
- 44. Lee, K.Y., K.H. Bouhadir, and D.J. Mooney, *Controlled degradation of hydrogels using multi-functional cross-linking molecules*. Biomaterials, 2004. **25**(13): p. 2461-2466.
- 45. Tanaka, H. and Y. Sato, *Photosensitivity of polyvinylesters of substituted cinnamylideneacetic acids*. Journal of Polymer Science Part A-1: Polymer Chemistry, 1972. **10**(11): p. 3279-3287.
- 46. Lu, M., et al., *Cell encapsulation with alginate and α-phenoxycinnamylidene-acetylated poly (allylamine)*. Biotechnology and bioengineering, 2000. **70**(5): p. 479-483.
- 47. Tønnesen, H.H. and J. Karlsen, *Alginate in drug delivery systems*. Drug development and industrial pharmacy, 2002. **28**(6): p. 621-630.
- 48. George, M. and T.E. Abraham, *Polyionic hydrocolloids for the intestinal delivery of protein drugs: alginate and chitosan—a review.* Journal of controlled release, 2006. **114**(1): p. 1-14.
- 49. Corporation, K., 2008.
- 50. Cao, Y., et al., *pH-induced self-assembly and capsules of sodium alginate*. Biomacromolecules, 2005. **6**(4): p. 2189-2196.
- 51. Mi, F.-L., et al., *Chitin/PLGA blend microspheres as a biodegradable drug delivery system: a new delivery system for protein.* Biomaterials, 2003. **24**(27): p. 5023-5036.
- 52. Abbah, S.-A., et al., *In vivo bioactivity of rhBMP-2 delivered with novel polyelectrolyte complexation shells assembled on an alginate microbead core template.* Journal of Controlled Release, 2012. **162**(2): p. 364-372.
- 53. Zhao, Q., et al., Assembly of multilayer microcapsules on CaCO3 particles from biocompatible polysaccharides. Journal of Biomaterials Science, Polymer Edition, 2006. **17**(9): p. 997-1014.
- 54. Li, X., et al., *In situ injectable nano-composite hydrogel composed of curcumin, N, O-carboxymethyl chitosan and oxidized alginate for wound healing application.* International journal of pharmaceutics, 2012. **437**(1): p. 110-119.
- Hooper, S.J., et al., *The visualisation and speed of kill of wound isolates on a silver alginate dressing*. International wound journal, 2012. **9**(6): p. 633-642.

- 56. Fragonas, E., et al., *Articular cartilage repair in rabbits by using suspensions of allogenic chondrocytes in alginate.* Biomaterials, 2000. **21**(8): p. 795-801.
- Wang, C.-C., et al., *Cartilage regeneration in SCID mice using a highly organized three-dimensional alginate scaffold.* Biomaterials, 2012. **33**(1): p. 120-127.
- 58. Awad, H.A., et al., *Chondrogenic differentiation of adipose-derived adult stem cells in agarose, alginate, and gelatin scaffolds.* Biomaterials, 2004. **25**(16): p. 3211-3222.
- 59. Paige, K.T., et al., *De novo cartilage generation using calcium alginate-chondrocyte constructs*. Plastic and reconstructive surgery, 1996. **97**(1): p. 168-78; discussion 179-80.
- 60. Bian, L., et al., Enhanced MSC chondrogenesis following delivery of TGF-β3 from alginate microspheres within hyaluronic acid hydrogels in vitro and in vivo. Biomaterials, 2011. **32**(27): p. 6425-6434.
- 61. Rubert, M., et al., *Effect of alginate hydrogel containing polyproline-rich peptides on osteoblast differentiation.* Biomedical Materials, 2012. **7**(5): p. 055003.
- 62. Florczyk, S.J., et al., *Enhanced bone tissue formation by alginate gel-assisted cell seeding in porous ceramic scaffolds and sustained release of growth factor.* Journal of Biomedical Materials Research Part A, 2012. **100**(12): p. 3408-3415.
- 63. Tang, M., et al., *Human embryonic stem cell encapsulation in alginate microbeads in macroporous calcium phosphate cement for bone tissue engineering*. Acta biomaterialia, 2012. **8**(9): p. 3436-3445.
- 64. Chen, W., et al., *Umbilical cord stem cells released from alginate—fibrin microbeads inside macroporous and biofunctionalized calcium phosphate cement for bone regeneration*. Acta biomaterialia, 2012. **8**(6): p. 2297-2306.
- 65. Xia, Y., et al., *Bone tissue engineering using bone marrow stromal cells and an injectable sodium alginate/gelatin scaffold.* Journal of Biomedical Materials Research Part A, 2012. **100**(4): p. 1044-1050.
- 66. Brun, F., et al., Automated quantitative characterization of alginate/hydroxyapatite bone tissue engineering scaffolds by means of micro-CT image analysis. Journal of Materials Science: Materials in Medicine, 2011. **22**(12): p. 2617-2629.
- 67. Kolambkar, Y.M., et al., *An alginate-based hybrid system for growth factor delivery in the functional repair of large bone defects.* Biomaterials, 2011. **32**(1): p. 65-74.
- 68. Nguyen, T.-P. and B.-T. Lee, *Fabrication of oxidized alginate-gelatin-BCP hydrogels* and evaluation of the microstructure, material properties and biocompatibility for bone tissue regeneration. Journal of biomaterials applications, 2012. **27**(3): p. 311-321.

- 69. Lee, K.Y. and D.J. Mooney, *Alginate: properties and biomedical applications*. Progress in polymer science, 2012. **37**(1): p. 106-126.
- 70. Tubbs, R.K., Sequence distribution of partially hydrolyzed poly (vinyl acetate). Journal of Polymer Science Part A-1: Polymer Chemistry, 1966. **4**(3): p. 623-629.
- 71. Kobayashi, M., Y.-S. Chang, and M. Oka, *A two year in vivo study of polyvinyl alcohol-hydrogel (PVA-H) artificial meniscus*. Biomaterials, 2005. **26**(16): p. 3243-3248.
- 72. Osswald, T.A., L.-S. Turng, and P.J. Gramann, *Injection molding handbook*. 2008: Hanser Verlag.
- 73. Bonnebat, C., L. Macabrey, and G. Roullet, *Melt extrusion, stretching, heat treatment mixture of polyvinyl alcohol and water*, 1991, Google Patents.
- 74. Hanke, D.E., *Odor-free thermoformed heat-degraded polyvinyl alcohol*, 1975, Google Patents.
- 75. Baker, M.I., et al., *A review of polyvinyl alcohol and its uses in cartilage and orthopedic applications*. Journal of Biomedical Materials Research Part B: Applied Biomaterials, 2012. **100**(5): p. 1451-1457.
- 76. von Burkersroda, F., L. Schedl, and A. Göpferich, *Why degradable polymers undergo surface erosion or bulk erosion*. Biomaterials, 2002. **23**(21): p. 4221-4231.
- 77. Company, M., MonoPol C100 Technical Data Sheet. 2014.
- 78. Company, M., MonoPol C250 Technical Data Sheet. 2014.
- 79. Company, D., Elvanol Technical Data Sheet. 2014.
- 80. Corporation, C.C., Catonia Polyvinyl Alcohol Technical Data Sheet. 2015.
- 81. Kramschuster, A. and L.-S. Turng, *An injection molding process for manufacturing highly porous and interconnected biodegradable polymer matrices for use as tissue engineering scaffolds.* Journal of Biomedical Materials Research Part B: Applied Biomaterials, 2010. **92B**(2): p. 366-376.
- 82. Technology, N.I.o.S.a., *IUPAC-NIST Solubility Database, Version 1.1 NIST Standard Reference Database 106.* 2015.
- 83. Bonapasta, A.A., et al., *Cross-linking of poly (vinyl alcohol) chains by Ca ions in macro-defect-free cements.* Chemistry of materials, 2002. **14**(3): p. 1016-1022.
- 84. Bailey, F.J., *Poly (ethylene oxide)*. 2012: Elsevier.

- 85. LLC, S.A.C., 2015.
- 86. Nguyen, K.T. and J.L. West, *Photopolymerizable hydrogels for tissue engineering applications*. Biomaterials, 2002. **23**(22): p. 4307-4314.
- 87. Peppas, N.A., et al., *Poly (ethylene glycol)-containing hydrogels in drug delivery.* Journal of controlled release, 1999. **62**(1): p. 81-87.
- 88. Harris, J.M., *Introduction to biotechnical and biomedical applications of poly (ethylene glycol)*. 1992: Springer.
- 89. Antonsen, K.P. and A.S. Hoffman, Water structure of PEG solutions by differential scanning calorimetry measurements, in Poly (Ethylene Glycol) Chemistry. 1992, Springer. p. 15-28.
- 90. Merrill, E.W., *Poly (ethylene oxide) star molecules: synthesis, characterization, and applications in medicine and biology.* Journal of Biomaterials Science, Polymer Edition, 1994. **5**(1-2): p. 1-11.
- 91. Brun, P., et al., *Electrospun scaffolds of self-assembling peptides with poly (ethylene oxide) for bone tissue engineering.* Acta biomaterialia, 2011. **7**(6): p. 2526-2532.
- 92. Bryant, S.J. and K.S. Anseth, *The effects of scaffold thickness on tissue engineered cartilage in photocrosslinked poly (ethylene oxide) hydrogels.* Biomaterials, 2001. **22**(6): p. 619-626.
- 93. Peckner, D. and I.M. Bernstein, *Handbook of stainless steels*. 1977: McGraw-Hill New York, NY.
- 94. Rauwendaal, C., *Understanding extrusion*. 1998: Hanser.
- 95. Rauwendaal, C., *Polymer extrusion*. 2014: Carl Hanser Verlag GmbH Co KG.
- 96. Maier, C., *Understanding compounding*. 1998: Hanser Verlag.
- 97. Lee, J., et al., *Novel foam injection molding technology using carbon dioxide-laden pellets.* Polymer Engineering & Science, 2011. **51**(11): p. 2295-2303.
- 98. Aronin, C.P., et al., Osteogenic differentiation of dura mater stem cells cultured in vitro on three-dimensional porous scaffolds of poly (\varepsilon-caprolactone) fabricated via co-extrusion and gas foaming. Acta biomaterialia, 2008. 4(5): p. 1187-1197.
- 99. Washburn, N.R., et al. *Development of biodegradable polymer scaffolds using co-extrusion*. in *MRS Proceedings*. 2000. Cambridge Univ Press.

- 100. Washburn, N.R., et al., *Co-extrusion of biocompatible polymers for scaffolds with co-continuous morphology*. Journal of biomedical materials research, 2002. **60**(1): p. 20-29.
- 101. Gomes, M.E., et al., A new approach based on injection moulding to produce biodegradable starch-based polymeric scaffolds: morphology, mechanical and degradation behaviour. Biomaterials, 2001. **22**(9): p. 883-889.
- 102. Bledzki, A.K. and O. Faruk, Effects of the chemical foaming agents, injection parameters, and melt-flow index on the microstructure and mechanical properties of microcellular injection-molded wood-fiber/polypropylene composites. Journal of Applied Polymer Science, 2005. **97**(3): p. 1090-1096.
- 103. Gong, S., et al., *Microcellular Injection Molding*. International Polymer Processing, 2005. **20**(2): p. 202-214.
- 104. Sun, X., et al., Fabrication of super ductile polymeric blends using microcellular injection molding. Manufacturing Letters, 2014. **2**(2): p. 64-68.
- 105. Wang, X., W. Li, and V. Kumar, *A method for solvent-free fabrication of porous polymer using solid-state foaming and ultrasound for tissue engineering applications*. Biomaterials, 2006. **27**(9): p. 1924-1929.
- 106. Stratasys, W., FDM System Documentation. 1996.
- 107. Ahn, S.-H., et al., *Anisotropic material properties of fused deposition modeling ABS*. Rapid Prototyping Journal, 2002. **8**(4): p. 248-257.
- 108. Hutmacher, D.W., et al., *Mechanical properties and cell cultural response of polycaprolactone scaffolds designed and fabricated via fused deposition modeling*. Journal of biomedical materials research, 2001. **55**(2): p. 203-216.
- 109. Zein, I., et al., Fused deposition modeling of novel scaffold architectures for tissue engineering applications. Biomaterials, 2002. **23**(4): p. 1169-1185.
- 110. Miller, J.S., et al., *Rapid casting of patterned vascular networks for perfusable engineered three-dimensional tissues*. Nature Materials, 2012.
- 111. Mironov, V., et al., *Organ printing: tissue spheroids as building blocks*. Biomaterials, 2009. **30**(12): p. 2164-2174.
- 112. Norotte, C., et al., *Scaffold-free vascular tissue engineering using bioprinting*. Biomaterials, 2009. **30**(30): p. 5910-5917.
- 113. Skardal, A., J. Zhang, and G.D. Prestwich, *Bioprinting vessel-like constructs using hyaluronan hydrogels crosslinked with tetrahedral polyethylene glycol tetracrylates*. Biomaterials, 2010. **31**(24): p. 6173-6181.

- 114. Guillotin, B. and F. Guillemot, *Cell patterning technologies for organotypic tissue fabrication*. Trends in biotechnology, 2011. **29**(4): p. 183-190.
- 115. Derby, B., *Bioprinting: inkjet printing proteins and hybrid cell-containing materials and structures.* Journal of Materials Chemistry, 2008. **18**(47): p. 5717-5721.
- 116. Mironov, V., G. Prestwich, and G. Forgacs, *Bioprinting living structures*. J. Mater. Chem., 2007. **17**(20): p. 2054-2060.
- 117. Jakab, K., et al., *Three-dimensional tissue constructs built by bioprinting*. Biorheology, 2006. **43**(3): p. 509-513.
- 118. Deckard, C.R. and P. McClure, Selective laser sintering. 1988.
- 119. Agarwala, M., et al., *Direct selective laser sintering of metals*. Rapid Prototyping Journal, 1995. **1**(1): p. 26-36.
- 120. Kruth, J.-P., et al., *Lasers and materials in selective laser sintering*. Assembly Automation, 2003. **23**(4): p. 357-371.
- 121. Williams, J.M., et al., *Bone tissue engineering using polycaprolactone scaffolds fabricated via selective laser sintering.* Biomaterials, 2005. **26**(23): p. 4817-4827.
- 122. Chua, C., et al., Development of tissue scaffolds using selective laser sintering of polyvinyl alcohol/hydroxyapatite biocomposite for craniofacial and joint defects. Journal of Materials Science: Materials in Medicine, 2004. **15**(10): p. 1113-1121.
- 123. Jacobs, P.F., *Rapid prototyping & manufacturing: fundamentals of stereolithography*. 1992: Society of Manufacturing Engineers.
- 124. Peltola, S.M., et al., *A review of rapid prototyping techniques for tissue engineering purposes*. Annals of medicine, 2008. **40**(4): p. 268-280.
- 125. Griffith, M.L. and J.W. Halloran, *Freeform fabrication of ceramics via stereolithography*. Journal of the American Ceramic Society, 1996. **79**(10): p. 2601-2608.
- 126. Melchels, F.P., J. Feijen, and D.W. Grijpma, *A poly (D, L-lactide) resin for the preparation of tissue engineering scaffolds by stereolithography*. Biomaterials, 2009. **30**(23): p. 3801-3809.
- 127. Seck, T.M., et al., *Designed biodegradable hydrogel structures prepared by stereolithography using poly (ethylene glycol)/poly (d, l-lactide)-based resins.* Journal of Controlled Release, 2010. **148**(1): p. 34-41.

- 128. Dhariwala, B., E. Hunt, and T. Boland, *Rapid prototyping of tissue-engineering constructs*, using photopolymerizable hydrogels and stereolithography. Tissue engineering, 2004. **10**(9-10): p. 1316-1322.
- 129. Knox, K., et al., Stereolithographic vascular replicas from CT scans: choosing treatment strategies, teaching, and research from live patient scan data. American journal of neuroradiology, 2005. **26**(6): p. 1428-1431.
- 130. Cooke, M.N., et al., *Use of stereolithography to manufacture critical-sized 3D biodegradable scaffolds for bone ingrowth.* Journal of Biomedical Materials Research Part B: Applied Biomaterials, 2003. **64**(2): p. 65-69.
- 131. Lee, K.-W., et al., *Poly (propylene fumarate) bone tissue engineering scaffold fabrication using stereolithography: effects of resin formulations and laser parameters.* Biomacromolecules, 2007. **8**(4): p. 1077-1084.
- 132. Chopra, K., et al., *Gel-cast glass-ceramic tissue scaffolds of controlled architecture produced via stereolithography of moulds.* Biofabrication, 2012. **4**(4): p. 045002.
- 133. De Momi, E., et al. *Hip joint anatomy virtual and stereolithographic reconstruction for preoperative planning of total hip replacement*. in *International Congress Series*. 2005. Elsevier.
- 134. Whitesides, G.M., et al., *Soft lithography in biology and biochemistry*. Annu Rev Biomed Eng, 2001. **3**: p. 335-73.
- 135. Xia, Y. and G.M. Whitesides, *Soft lithography*. Annual review of materials science, 1998. **28**(1): p. 153-184.
- 136. Kane, R.S., et al., *Patterning proteins and cells using soft lithography*. Biomaterials, 1999. **20**(23–24): p. 2363-2376.
- 137. Mrksich, M., et al., *Using Microcontact Printing to Pattern the Attachment of Mammalian Cells to Self-Assembled Monolayers of Alkanethiolates on Transparent Films of Gold and Silver*. Experimental Cell Research, 1997. **235**(2): p. 305-313.
- 138. Wheeler, B.C., et al., *Microcontact Printing for Precise Control of Nerve Cell Growth in Culture*. Journal of Biomechanical Engineering, 1999. **121**(1): p. 73-78.
- 139. Craighead, H.G., C.D. James, and A.M.P. Turner, *Chemical and topographical patterning for directed cell attachment*. Current Opinion in Solid State and Materials Science, 2001. **5**(2–3): p. 177-184.
- 140. Lauer, L., et al., *Aligned microcontact printing of biomolecules on microelectronic device surfaces*. Biomedical Engineering, IEEE Transactions on, 2001. **48**(7): p. 838-842.

- 141. James, C.D., et al., Aligned microcontact printing of micrometer-scale poly-L-Lysine structures for controlled growth of cultured neurons on planar microelectrode arrays. Biomedical Engineering, IEEE Transactions on, 2000. **47**(1): p. 17-21.
- 142. Bernard, A., et al., *Printing Patterns of Proteins*. Langmuir, 1998. **14**(9): p. 2225-2229.
- 143. Bernard, A., et al., *Microcontact Printing of Proteins*. Advanced Materials, 2000. **12**(14): p. 1067-1070.
- 144. Schreiber, F., *Structure and growth of self-assembling monolayers*. Progress in Surface Science, 2000. **65**(5–8): p. 151-257.
- 145. Lange, S.A., et al., *Microcontact Printing of DNA Molecules*. Analytical Chemistry, 2004. **76**(6): p. 1641-1647.
- 146. Thibault, C., et al., *Direct microcontact printing of oligonucleotides for biochip applications*. Journal of Nanobiotechnology, 2005. **3**(7).
- 147. Valencia, P.M., et al., *Microfluidic technologies for accelerating the clinical translation of nanoparticles*. Nature nanotechnology, 2012. **7**(10): p. 623-629.
- 148. Khademhosseini, A., et al., *A soft lithographic approach to fabricate patterned microfluidic channels*. Analytical chemistry, 2004. **76**(13): p. 3675-3681.
- 149. Qin, D., Y. Xia, and G.M. Whitesides, *Soft lithography for micro-and nanoscale patterning*. Nature protocols, 2010. **5**(3): p. 491-502.
- 150. Kumar, A. and G.M. Whitesides, Features of gold having micrometer to centimeter dimensions can be formed through a combination of stamping with an elastomeric stamp and an alkanethiol 'ink''followed by chemical etching. Applied Physics Letters, 1993. **63**(14): p. 2002-2004.
- 151. Liao, W.-S., et al., *Subtractive patterning via chemical lift-off lithography*. science, 2012. **337**(6101): p. 1517-1521.
- 152. Odom, T.W., et al., *Improved pattern transfer in soft lithography using composite stamps*. Langmuir, 2002. **18**(13): p. 5314-5320.
- 153. Ng, E., et al., *Multicolor microcontact printing of proteins on nanoporous surface for patterned immunoassay*. Applied Nanoscience, 2011. **1**(2): p. 79-85.
- 154. Bou Chakra, E., et al., *A new instrument for automated microcontact printing with stamp load adjustment*. Review of Scientific Instruments, 2008. **79**(6): p. 064102-064102-9.

- 155. Tien, J., C.M. Nelson, and C.S. Chen, *Fabrication of aligned microstructures with a single elastomeric stamp*. Proceedings of the National Academy of Sciences, 2002. **99**(4): p. 1758-1762.
- 156. Trinkle, C.A. and L.P. Lee, *High-precision microcontact printing of interchangeable stamps using an integrated kinematic coupling.* Lab Chip, 2010. **11**(3): p. 455-459.
- 157. Epson, Epson LS3.
- 158. Lippmann, E.S., M.C. Estevez-Silva, and R.S. Ashton, *Defined human pluripotent stem cell culture enables highly efficient neuroepithelium derivation without small molecule inhibitors.* STEM CELLS, 2013: p. n/a-n/a.
- 159. Horn, B.K., *Closed-form solution of absolute orientation using unit quaternions*. JOSA A, 1987. **4**(4): p. 629-642.
- 160. Knight, G.T., et al., Fabricating Complex Culture Substrates Using Robotic Microcontact Printing (R-μCP) and Sequential Nucleophilic Substitution. JoVE (Journal of Visualized Experiments), 2014(92): p. e52186-e52186.
- 161. Harkness, T., et al., *High-content imaging with micropatterned multiwell plates reveals influence of cell geometry and cytoskeleton on chromatin dynamics*. Biotechnology journal, 2015.
- 162. Cao, Y., et al., *Transplantation of Chondrocytes Utilizing a Polymer-Cell Construct to Produce Tissue-Engineered Cartilage in the Shape of a Human Ear.* Plastic and Reconstructive Surgery, 1997. **100**(2): p. 297-302.
- 163. Murphy, S.V. and A. Atala, *3D bioprinting of tissues and organs*. Nat Biotech, 2014. **32**(8): p. 773-785.
- 164. Fernandez, J.G. and A. Khademhosseini, *Micro-Masonry: Construction of 3D Structures by Microscale Self-Assembly*. Advanced Materials, 2010. **22**(23): p. 2538-2541.
- 165. Kolesky, D.B., et al., 3D Bioprinting of Vascularized, Heterogeneous Cell-Laden Tissue Constructs. Advanced Materials, 2014.
- 166. Bellan, L.M., et al., Fabrication of an artificial 3-dimensional vascular network using sacrificial sugar structures. Soft Matter, 2009. **5**(7): p. 1354-1357.
- 167. Wu, W., et al., *Direct-write assembly of biomimetic microvascular networks for efficient fluid transport.* Soft Matter, 2010. **6**(4): p. 739-742.
- 168. Tocchio, A., et al., *Versatile fabrication of vascularizable scaffolds for large tissue engineering in bioreactor.* Biomaterials, 2015. **45**: p. 124-131.

- 169. Wang, X.-Y., et al., Engineering interconnected 3D vascular networks in hydrogels using molded sodium alginate lattice as the sacrificial template. Lab on a Chip, 2014. **14**(15): p. 2709-2716.
- 170. Golden, A.P. and J. Tien, *Fabrication of microfluidic hydrogels using molded gelatin as a sacrificial element.* Lab Chip, 2007. **7**(6): p. 720-725.
- 171. Cuchiara, M.P., et al., *Multilayer microfluidic PEGDA hydrogels*. Biomaterials, 2010. **31**(21): p. 5491-5497.
- 172. Ashton, R.S., et al., Scaffolds based on degradable alginate hydrogels and poly(lactide-co-glycolide) microspheres for stem cell culture. Biomaterials, 2007. **28**(36): p. 5518-5525.
- 173. Banerjee, A., et al., *The influence of hydrogel modulus on the proliferation and differentiation of encapsulated neural stem cells*. Biomaterials, 2009. **30**(27): p. 4695-4699.
- 174. Rowley, J.A., G. Madlambayan, and D.J. Mooney, *Alginate hydrogels as synthetic extracellular matrix materials*. Biomaterials, 1999. **20**(1): p. 45-53.
- 175. Paul, W. and C.P. Sharma, *Chitosan and alginate wound dressings: a short review*. Trends Biomater Artif Organs, 2004. **18**(1): p. 18-23.
- 176. Alsberg, E., et al., *Cell-interactive alginate hydrogels for bone tissue engineering*. Journal of dental research, 2001. **80**(11): p. 2025-2029.
- 177. Liu, S.j. and Y.s. Chen, *Water-assisted injection molding of thermoplastic materials: Effects of processing parameters.* Polymer Engineering & Science, 2003. **43**(11): p. 1806-1817.
- 178. Chen, Z. and L.S. Turng, *A review of current developments in process and quality control for injection molding*. Advances in Polymer Technology, 2005. **24**(3): p. 165-182.
- 179. Toepke, M.W., et al., *Characterization of Thiol-Ene Crosslinked PEG Hydrogels*. Macromolecular materials and engineering, 2013. **298**(6): p. 699-703.
- 180. Peyton, S.R., et al., *The use of poly (ethylene glycol) hydrogels to investigate the impact of ECM chemistry and mechanics on smooth muscle cells.* Biomaterials, 2006. **27**(28): p. 4881-4893.
- 181. Standard, A., *D638: Standard Test Method for Tensile Properties of Plastics.* West Conshohocken (PA): ASTM International, 2010.

- 182. Tsur-Gang, O., et al., The effects of peptide-based modification of alginate on left ventricular remodeling and function after myocardial infarction. Biomaterials, 2009. **30**(2): p. 189-195.
- 183. Yao, D. and B. Kim, *Development of rapid heating and cooling systems for injection molding applications*. Polymer Engineering & Science, 2002. **42**(12): p. 2471-2481.
- 184. Chen, S.-C., et al., *Variable mold temperature to improve surface quality of microcellular injection molded parts using induction heating technology*. Advances in Polymer Technology, 2008. **27**(4): p. 224-232.
- 185. Turng, L.S. and H. Kharbas, *Development of a Hybrid Solid-Microcellular Co-injection Molding Process*. International Polymer Processing, 2004. **19**(1): p. 77-86.
- 186. Lee, J., et al., A novel method for improving the surface quality of microcellular injection molded parts. Polymer, 2011. **52**(6): p. 1436-1446.
- 187. Lee, J. and L.-S. Turng, *Improving surface quality of microcellular injection molded parts through mold surface temperature manipulation with thin film insulation*. Polymer Engineering & Science, 2010. **50**(7): p. 1281-1289.
- 188. Chen, S.C., P.S. Hsu, and Y.W. Lin, *Establishment of Gas Counter Pressure Technology and Its Application to Improve the Surface Quality of Microcellular Injection Molded Parts*. International Polymer Processing, 2011. **26**(3): p. 275-282.
- 189. Passilla, J. and K. Zupancic. Warpage study on two-shot injection molding. in ANTEC-CONFERENCE PROCEEDINGS-. 2005.
- 190. Beaumont, J.P., R. Nagel, and R. Sherman, *Successful injection molding*. Hanser, Munich, 2002.
- 191. Jones, I., *Laser welding for plastic components*. Assembly Automation, 2002. **22**(2): p. 129-135.
- 192. Klein, R., Laser welding of plastics. 2013: John Wiley & Sons.
- 193. Tolunay, M.N., P.R. Dawson, and K.K. Wang, *Heating and bonding mechanisms in ultrasonic welding of thermoplastics*. Polymer Engineering & Science, 1983. **23**(13): p. 726-733.
- 194. Grewell, D. and A. Benatar, *Welding of Plastics: Fundamentals and New Developments*. International Polymer Processing, 2007. **22**(1): p. 43-60.
- 195. Bucknall, C.B., I.C. Drinkwater, and G.R. Smith, *Hot plate welding of plastics:* Factors affecting weld strength. Polymer Engineering & Science, 1980. **20**(6): p. 432-440.

- 196. Rosato, D.V., D.V. Rosato, and M.G. Rosato, *Injection molding handbook*. 2000: springer.
- 197. Catalanotti, P. and A. Lotfi, *Molding apparatus with collapsible core*, 1990, Google Patents.
- 198. Stevenson, J.F., Innovation in polymer processing: molding. 1996: Hanser.
- 199. Avery, J., *Injection molding alternatives: a guide for designers and product engineers.* 1998: Hanser.
- 200. Arzondo, L.M., et al., Sequential injection overmolding of an elastomeric ethyleneoctene copolymer on a polypropylene homopolymer core. Polymer Engineering & Science, 2004. **44**(11): p. 2110-2116.
- 201. Moore, T.M. and G.W. Van der Woude, *Dissolving in hot water*, 1992, Google Patents.
- 202. NARUTOMI, M.T.P.C.L., *Method of manufacturing plastic moldings and core used in same*, 1999, Google Patents.
- 203. Hattori, J., N. Shibahara, and S. Torigoe, Sacrificial molding, 1995, Google Patents.